UNDERSTANDING AND CONTROLLING THE TRIBOLOGICAL PROPERTIES OF GRAPHENE ON ROUGH SURFACES

A Dissertation

by

JESSICA CRYSTAL SPEAR

Submitted to the Office of Graduate and Professional Studies of
Texas A&M University
in partial fulfillment of the requirements for the degree of

DOCTOR OF PHILOSOPHY

Chair of Committee,	James D. Batteas
Committee Members,	Dong H. Son
	Jaime C. Grunlan
	Emile A. Schweikert
Head of Department,	Francois P. Gabbai

December 2015

Major Subject: Chemistry

ABSTRACT

Understanding and controlling friction, adhesion and wear is critical for the continued growth and utilization of emerging nanotechnologies such as micro- and nano-electromechanical systems devices (NEMS/MEMS). The challenge of operating NEMS/MEMS with contacting interfaces stems from the large surface-to-volume ratio of these devices where surface forces dominate the interfacial interactions. Capillary forces, even in low humidity, can increase adhesion causing high friction and sticking as well as catalyzing wear on the surface. In addition, the nanoscale roughness of surfaces leads to high pressures and shear forces at asperity-asperity contacts, ultimately leading to device failure.

To mitigate friction and wear of silicon surfaces, two-dimensional solid state lubricants such as graphene have drawn increased interest due to the rapid development of fabrication techniques. One of the newest carbon nanomaterials, graphene is a single atomic layer of highly ordered pyrolytic graphite. Studies over the past decade on graphene have elucidated a variety of unique properties such as large out-of-plane flexibility, strong in-plane modulus and chemical inertness which have made it an ideal candidate for use as a protective surface coating. Although graphene can easily adopt a similar morphology to its underlying substrate, the properties of graphene are largely influenced by its environmental and substrate interactions.

To better understand and address the challenges of graphene's substrate mediated properties for applications to NEMS/MEMS, this dissertation includes research on the

fundamental interactions between graphene and rough substrates. Using Atomic Force Microscopy, the morphology of graphene on rough surfaces was shown to partially conform to the substrate roughness as a result of the size and spacing of the nanoparticle asperities and a balance between the interfacial adhesion and strain in the graphene lattice. This type of morphology decreases the contact between graphene and the substrate resulting in a weakly bound state that is undesirable for use as a protective coating. However, exploring the mechanical properties showed that under increased loading the conformity could be controllably increased and the frictional properties showed a dependence on the asperity-asperity contact area unique to these types of rough substrate geometries. Based on these results, further research was explored to control the tribological properties of graphene by systematically changing the nanoscale roughness and surface chemistry to increase graphene adhesion to the substrate for better friction modification.

ACKNOWLEDGMENTS

I would first like to thank my advisor, James Batteas, for his mentoring and endless patience over the past five years of graduate school here at Texas A&M University. I would also like to thank the Batteas Group members I have worked with over the years, especially Chi-Yuan Chang, Arika Pravitasari, and Augustin Diaz for their mentoring and friendship.

I am also grateful to my Western Carolina University undergraduate mentors Shan Manickam, Carmen Huffman, and William Kwochka for their teaching, guidance, and encouragement to pursue a Ph.D. in chemistry. Additionally, I would like to thank my high school JROTC army instructors for their leadership training which helped me build the confidence to dream big in a very small town.

Most importantly, I would like to thank my parents, Rondy and Christine Spear, for their life-long support and encouragement. I am very grateful to have such loving and supportive parents who gave me the freedom to always make my own choices in life.

TABLE OF CONTENTS

Page

Page

Page

LIST OF FIGURES

Page

Page

Page

Page

Page

Page

Page

LIST OF TABLES

Page

CHAPTER I

INTRODUCTION AND LITERATURE REVIEW: 2D-NANOMATERIALS FOR CONTROLLING FRICTION AND WEAR AT INTERFACES*

1.1 Overview

Control of friction and wear are widely recognized problems that impact a broad range of materials applications from gears and engine components, to medical implants for joint replacement, to micro- and nano-scaled machine technologies, such as micro - and nano - electromechanical systems (MEMS, NEMS) devices. The nearly ubiquitous impact of friction and wear in numerous sectors of the economy (Figure 1.1) persistently motivates research into lubrication and surface coating schemes that more effectively address these challenges. At its core, this research is poised to proffer significantly improved efficiencies in the generation and usage of energy, one of society's most fundamental needs. Layered materials like graphite, MoS_2, and hexagonal boron nitride (h-BN) have long been recognized as effective surface lubricants.[1-3] Offering the advantages of being solids, these lubricious films can be applied to open systems and can also be applied in other circumstances in which liquid lubrication is not appropriate. In all cases they offer interlayer sliding interfaces with phenomenally low interfacial shear

* Reprinted from Spear, J. C.; Ewers, B. W.; Batteas, J. D. *Nano Today* **2015,** 10, (3), 301-314 with permission from Elsevier.

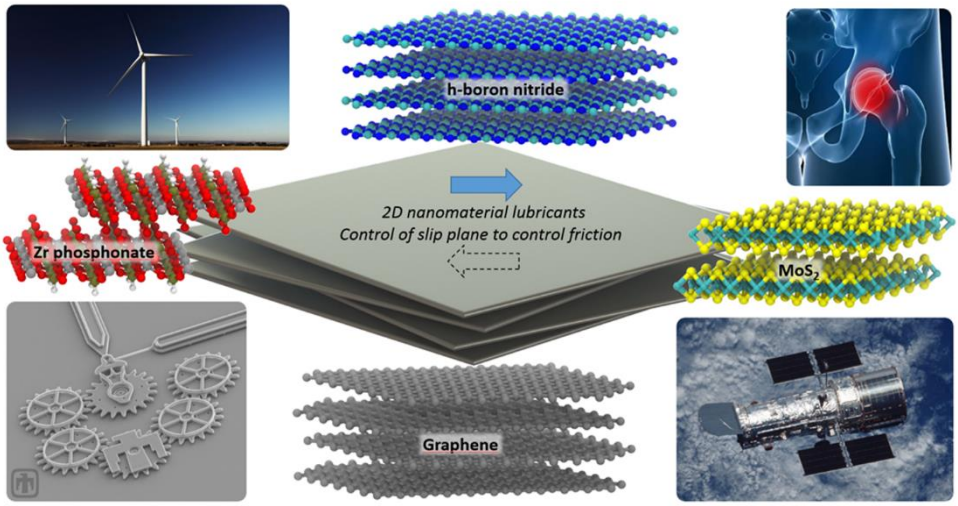

Figure 1.1. Layered materials like graphite, molybdenum disulfide, hexagonal boron nitride, and zirconium phosphates offer solutions to lubrication challenges in a variety of economically and technologically critical sectors of society. Pictures courtesy of NIH Senior Health, Sandia National Laboratories, SUMMiT™ Technologies, www.mems.sandia.gov, and NASA and the Space Telescope Science Institute.

strengths facilitated by characteristically weak interlayer interactions within the materials.[4, 5]

Recently, the ability to isolate single atomic layers of these materials has promoted an interesting new area of research into their frictional properties. Since its discovery in 2004,[6] graphene in particular has drawn considerable attention. Made up of a simple honeycomb carbon lattice, it has been found to exhibit many unique electronic and mechanical properties including ballistic electron transport,[7] high thermal conductivity,[8-11] large in-plane elastic modulus[12] and a low coefficient of friction.[13-15] These desirable properties make graphene of considerable interest for potential use in many applications including composite materials,[16] energy transfer[17] and storage,[18] electronic[19] and mechanical devices,[20] and solid-state lubrication.[13-15, 21] Although

mechanical exfoliation produces the most pristine, defect free graphene (edge sites not withstanding), it is not feasible for bulk production and large scale applications. Chemical vapor deposition (CVD) has been utilized as an alternative means to fabricate large area graphene by thermal decomposition of silicon carbide (SiC) and by its catalyzed growth on various metal surfaces.[22] Interestingly, there is also evidence that graphitic carbon can be generated *in situ* within sliding contacts which could provide a mechanism by which such surface coatings could be formed and repaired.[23] When considering utilizing graphene in real devices however, it must be recognized that its electronic and mechanical properties strongly depend on the interfacial interaction with the underlying substrate.[24, 25] Due to its high out-of-plane flexibility, the morphology of graphene is dictated by the substrate geometry, which influences the measured properties through changes in electronic structure, topological defects, and chemical doping effects,[26-31] and the frictional properties of graphene have been reported to have a unique dependence on the substrate surface roughness and interfacial adhesion.[32-34]

With the isolation of graphene, the study of friction of single atomic layers could be pursued, offering potentially the thinnest feasible surface coating one could use as a lubricant. Akin to graphene, a host of other layered inorganic materials (e.g. h-BN, MoS_2, Y_2O_3, Zr phosphates) are also being explored, all of which have been seen to provide modest to exceptional friction reduction in devices. By expanding the library of solid lubricants which may be employed at sliding interfaces, lubrication of a broader range of materials in a wider range of environments may be achieved, and single layer studies of these materials have begun to expand. Oddly enough, by considering

lubrication with a single layer, the weak interlayer interactions that have largely defined their lubricity are no longer present, and interactions between the layered material and the substrate dominate. Rather, interest in single layers is largely motivated by the interaction anisotropy that renders such layered materials relatively chemically inert, as well as the high mechanical strength of these materials, which together offer a means to chemically and mechanically modify a surface with only a single atomic layer of material.

That is not to say that these studies are not interesting or useful in their own right in terms of solid lubrication. The ability to study the frictional characteristics of single and few layered samples of these materials makes it possible to isolate the effects of the interface between the lubricant and the substrate, which is more challenging when the majority of sliding occurs between the layers. These interactions become increasingly important in demanding nanoscale applications where the most effective lubrication with the least amount of material is essential, and in these cases, the lubricant-substrate interface will have increasing influence on the mechanical, dissipative, and chemical properties of the layered lubricant, it is therefore essential that these interactions, and the factors that influence them, be understood.

There are effectively two interfaces that must be understood to characterize and optimize the frictional characteristics or layered materials. First, and probably foremost, is the interlayer interface, as the majority of interfaces lubricated with these materials will be protected by multiple layers and the majority of sliding will occur between the layers. Second, the interface between the substrate and the lubricant, which becomes

increasingly important as the number of layers at the interface is reduced. Factors like nanoscale morphology and chemistry are perhaps the most important, raising issues of film conformity that leads to behaviors like wrinkling and puckering that create increased real area of contact and additional dissipation pathways that influence the frictional characteristics of these materials.

This review focuses on three critical areas of 2D lubricant materials. First, the influence of interlayer interactions, as studied through a variety of computational methods, are discussed, as these interactions form the foundation of layered material lubricity in the majority of applications. Next, studies examining substrate-lubricant interactions, facilitated by the isolation of single and few layer graphene and other layered materials, are discussed, emphasizing this new area of research in layered materials and exploring factors like substrate morphology, interaction strength, and the sliding environment. Finally, studies seeking to apply 2D nanomaterials in sliding contacts are discussed, exploring their incorporation in lubricant fluids as nanoparticles and platelets in order to evaluate the relevant challenges in the incorporation of these materials as lubricants and lubricant additives.

1.2 Interlayer Interactions in Layered Materials

Computational approaches provide an excellent means to study the underlying mechanisms governing the friction of layered materials. Application of these techniques largely focus on two key aspects: contributions to friction from structural features that are either too small to resolve or inaccessible to experiment like atomic scale roughness,[34] defects, wrinkling,[35] and step edge effects,[36] and the role of interlayer

interactions in the response of sliding materials. Perhaps the most appealing feature of layered materials is the general weakness of their interlayer interactions, and their superlubricity is largely attributed to variations in these interactions. These contributions to the friction response are challenging to probe in single asperity measurements, and though they are present in macroscopic sliding contacts, they cannot be easily isolated. Computational approaches therefore provide the best means available

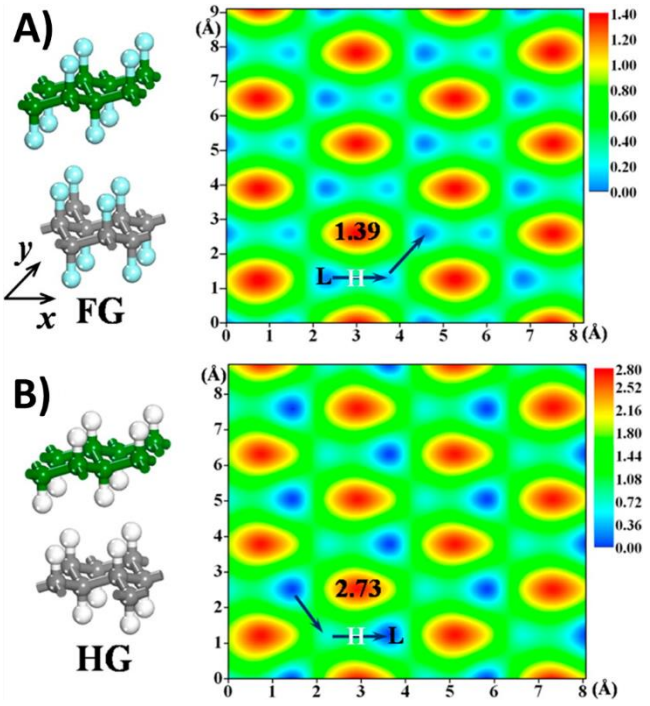

Figure 1.2. Models of fluorinated (A) and hydrogenated (B) graphene (FG and HG respectively), where grey atoms indicate carbon, blue fluorine, and white hydrogen. Corresponding potential energy surfaces are shown, with the favored path of sliding indicated. The highest and lowest energy points on these sliding pathways are denoted H and L respectively. Reproduced with permission from Ref.[37] Copyright 2013, American Chemical Society.

to study the role of interlayer interactions and the mechanisms that give rise to superlubricity of layered materials.

The potential energy corrugation is a fundamental parameter in determining the magnitude of the shear strains that originate during sliding, and consequently influences the magnitude of the friction force. Determination of the interlayer potential requires only a single unit cell geometry, a size that is easily accessible by density functional theory (DFT),[38, 39] and this approach has been used to investigate the interlayer interactions of molybdenum disulfide,[40, 41] graphite,[39] and hexagonal boron nitride[38] and derivatives.[42, 43] Modified DFT functionals with dispersion corrections must typically be employed due to the weak interactions between sheets, though the shape of the potential can be obtained by applying pressure to the system, such that Pauli repulsion dominates the interlayer interaction.[44] Sample potential energy surfaces of hydrogenated and fluorinated graphene are depicted in Figure 1.2, showing the maximal potential energy and the most favorable sliding pathway, and a summary of the potential variations in common layered materials is provided in Table 1.1.

Interestingly, hydrogenated and fluorinated graphene exhibit the lowest potential corrugation, suggesting that they would exhibit the lowest friction of these materials when sliding occurs between layers. To date, however, only Atomic Force Microscopy (AFM) measurements of friction across the modified graphene surface, rather than sliding between layers of the material, have been performed. In these cases, greater friction than that observed for pristine graphite was observed,[45] and atomic roughness of the modified graphene sheet[46] or contributions due to increased out-of-plane stiffness[45]

Material	U_{max}-U_{min} (meV/atom)	U_{max}-U_{min} (meV/atom) (Free sliding path)	Method[Ref.]
Graphene	10	2-3	DFT-PBE-D[39]
h-BN	30	3-4	DFT-B3LYP+TS-vdW[38]
Graphene/h-BN	20	15	DFT-PBE-vdW[42]
F-Graphene	1.4	0.3	DFT-PBE-D[37]
H-Graphene	2.7	1	DFT-PBE-D[37]
MoS_2	30	10	DFT-PBE-D[41]

Table 1.1 Compilation of available sliding energy surface corrugation maxima and variation along the free sliding path measured at the equilibrium separation of the layers, expressed in terms of the potential energy difference between points of highest (Umax) and lowest (Umin) potential energy along the sliding path.

have been proposed as a mechanism for the greater friction response under these conditions.

Breaking the periodicity of a layered system dramatically reduces the potential corrugation of interlayer sliding. The effect is difficult to determine by ab initio methods, but through application of the registry index developed by Hod *et al*., the effect is clearly illustrated.[47] The registry index is a normalized result, varying from 0 to 1, which describes the favorability of a given stacking configuration. A value of 0 corresponds to two layers at their equilibrium position, consistent with the crystal structure of the material, while 1 corresponds to the most unfavorable position. For example, graphene varies from 0 for the AB crystalline structure to 1 for the AA structure in which all atoms overlap, while isoelectronic h-BN varies from 0 for the AA'

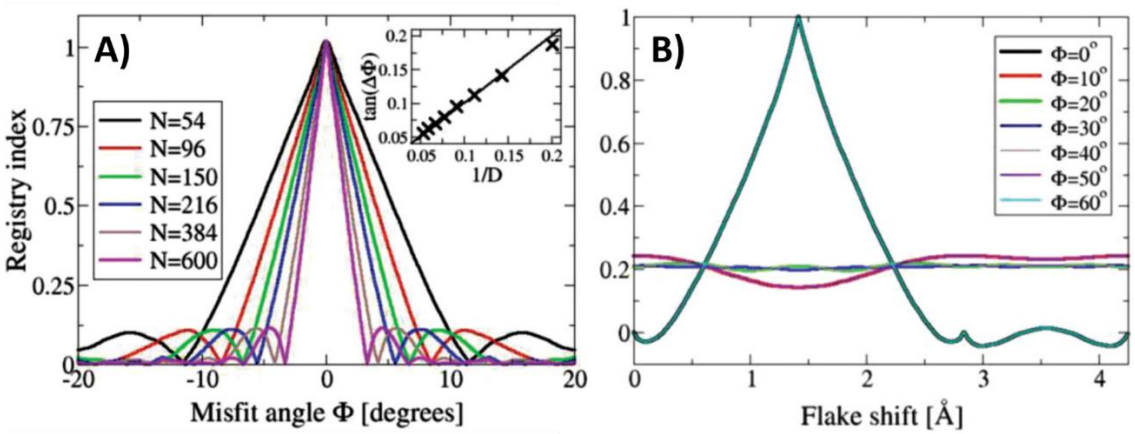

Figure 1.3. Variation of registry index as a function of flake size, expressed in terms of N carbon atoms, and misfit angle (A), and variation in registry index during sliding for different misfit angles (Φ) between sheets (B). The dramatic reduction in registry index variation results in dramatic reductions in friction. Adapted from Ref.[48] Copyright 2012 American Physical Society.

stacking structure to 1 for AA stacking. Through proper tuning of the parameters used to determine the registry index, it scales roughly with the potential energy, and can be more easily calculated for large, aperiodic systems. Figure 1.3A depicts the registry index as a function of mismatch angle in graphene for a range of flake sizes. Large flakes require a smaller rotation to become effectively incommensurate,[48] but more energy is required to achieve this state. Figure 1.3B depicts the variation in the registry index for different misfit angles, demonstrating dramatic reduction in the variation of the RI, and a corresponding reduction in the friction response has been observed for graphitic systems.[2, 48, 49] This is not a particularly surprising result, sliding of commensurate crystals is generally observed to produce a very high friction response due to the large area and numerous, constructive interactions involved. Layered materials offer the weakest interlayer interactions conceivable but nevertheless, when

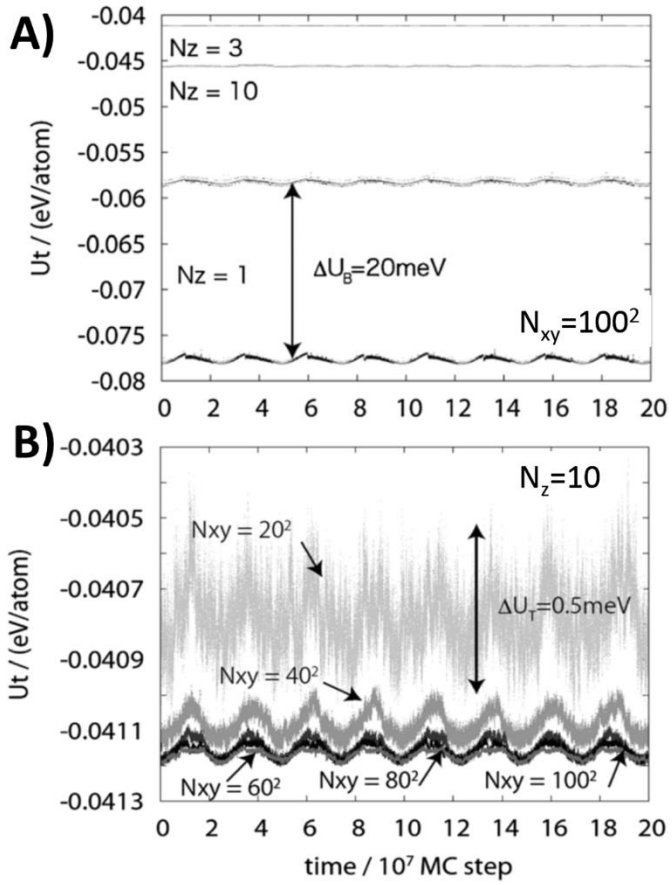

Figure 1.4. Thermal fluctuations in the potential energy (UT) for varying numbers (Nz) of stacked graphene flakes (A) and sheets of varying size, expressed in terms of the number of carbon atoms represented in the sheet (Nxy). Large fluctuations for the case Nz=1 were observed because the single sheet was force to oscillate between two stable points dictated by the upper and lower fixed sliders, the difference in these two states denoted by ΔUB. Adapted with permission from Ref.[50] Copyright 2012, RSC Publishing.

commensurate, these interactions will scale with the size of the sliding interface which is unfavorable in terms of minimizing friction.

To maximize the lubrication benefit of layered materials it is thus necessary to identify the ideal conditions in which layers are able to escape the commensurate state.

Using coarse-grained Metropolis Monte Carlo Brownian Dynamics,[51] Washizu *et al*. examined the dynamics of multilayer graphene sliding as a function of number of layers and sheet size to determine the likelihood of "thermal escape," i.e. the slipping of graphene flakes out of the commensurate state due to thermal energy.[50] In this work, they examined the dynamics of graphene sheets sliding on an infinite graphite plane, and the variations in potential energy of these sliding simulations are depicted in Figure 1.4A and 1.4B as a function of layer count and sheet size respectively. They found that single sheet motion on an infinite graphene plane is highly restricted, and these restrictions result in large oscillations of the system energy that can give rise to greater friction. Flake size also dictates the magnitude of the interactions. In the smallest flakes studied (r=2 nm), thermal fluctuations dominate the variation in potential energy. For larger flakes, thermal fluctuations are more muted because the total interaction energy scales with flake size, but give rise to more stable potential energy profiles that would yield low friction. For the largest flakes studied (r=90 nm), however, thermal energy was insufficient to dislodge the flakes from the commensurate state, and their highly restricted motion would similarly give rise to greater friction. These results indicate that the most lubricating materials would consist of both multi-layered, and small grained structures.

1.3 Graphene: 2D or not 2D? That is the Question

Graphene is one of the newest nanoscale carbon allotropes including carbon nanotubes and fullerenes. It is a 2D material with a wide array of interesting properties such as chemical stability, hydrophobicity, impermeability, excellent mechanical

properties with a high in-plane elastic modulus,[12] large out-of-plane flexibility, and low coefficient of friction.[13-15] These properties make it ideally suited for many applications, including the field of tribology, as a protective surface coating and friction modifier. There has been numerous experimental and theoretical studies devoted to understanding the structure-property relationship and modifications for improving the applicability of graphene to the field of tribology, but a broader fundamental understanding is still required.

Currently the frictional mechanisms for using 2D materials as friction modifiers has been found to depend on a variety of factors including the thickness of the graphene layers, the surface morphology and chemistry, and the fabrication method such as mechanical exfoliation, chemical vapor deposition, thermal decomposition, and reduction of graphene oxide. Some of the most recent work in this area is reviewed here and more thorough reviews, specifically on graphene, can be found elsewhere.[52-54]

1.3.1 Nanotribological Studies on Graphene

To use graphene as a protective coating or friction modifier it must be interfaced with different substrates depending on the desired applications. Nanotribological experiments are key for understanding these interfacial interactions and the resulting fundamental friction mechanisms. Nanoscale studies using AFM investigated the friction of graphene on smooth and atomically rough surfaces and have found that the strength of graphene adhesion to the substrate largely depends on the morphology of the substrate.[32, 33] Experiments of exfoliated graphene on flat surfaces such as mica, h-BN, and graphite showed no layer dependence in the frictional properties, implying that

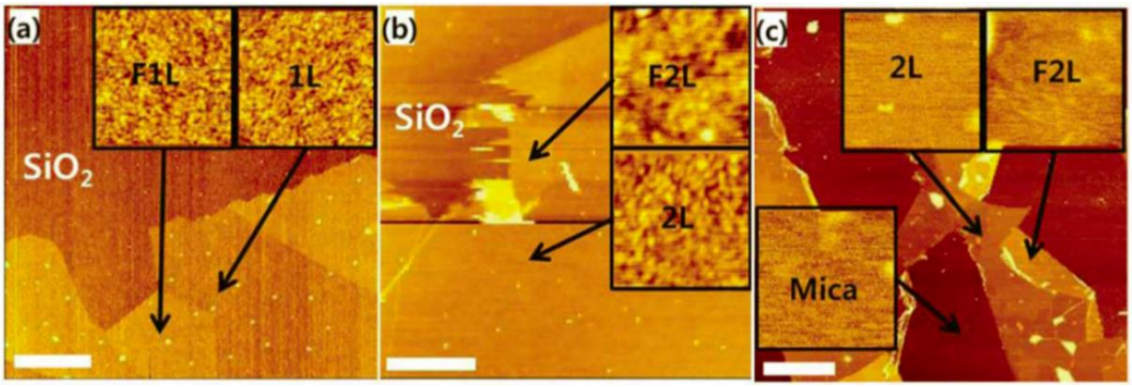

Figure 1.5. Topography images of (a) folded mono-layer graphene on SiO_2, (b) folded bi-layer graphene on SiO_2 and (c) folded bi-layer graphene on mica. Inset images acquired for the region indicated by black arrows have the same scan size of 500 x 500 nm^2 with identical z-scale (0 to 1.23 nm). 'F1L' and 'F2L' represent folded mono- and bi-layer graphene, respectively. Scale bars, 2 μm. Reproduced from Ref.[32] with permission of The Royal Society of Chemistry.

graphene can reduce the friction as effectively as its bulk lamellar counterpart graphite when it makes good contact with the interface and has strong adhesion. However, on atomically rough surfaces such as SiO_2, the intimate contact with the substrate is reduced which decreases the adhesive van der Waals forces between the substrate and graphene, inducing a "puckering" effect with friction as high as double that of bulk graphite. It known that the flexibility of graphene allows it to maximize its conformity to whatever substrate it is interfaced with, and by folding the flakes of graphene with an AFM tip, the morphology of the substrate was seen to be preserved as shown in Figure 1.5. Since the graphene maintained a rough configuration after folding from SiO_2, the friction was still higher despite added thickness due to the decreased contact with the flat substrate. Hence, the adhesion to the substrate also depends on the morphology before and after transfer which should be considered in cases where graphene is processed after

fabrication for transfer to other surfaces as a protective coating.[32] As the surface roughness transitions to the nanoscale, the balance of substrate morphology and graphene-substrate interactions plays a critical role in the friction observed, as it results in regions of conformed and unconformed states. For example, studies of graphene on silica nanoparticle films with controlled nanoscopic roughness (*ca.* 10 nm rms) show that the frictional properties strongly depended upon the relative adhesion between the AFM probe tip and the substrate, with suppression of the "puckering" effect, mentioned above, occurring when there is large surface roughness and low adhesion to the tip.[55]

As most nanoscale studies have been done under ambient conditions the environmental dependence of friction and adhesion properties of graphene are also relevant. Under humid conditions, the adhesion[56] and friction forces generally decreased with lower humidity due to reduction of the capillary force but similar trends, such as the puckering effect, are still observed even under dry nitrogen and vacuum.[33, 57] The effect of liquid environment on the adhesion and friction forces of few layer graphene has been found to be different from ambient studies in that the measured forces also depend on the polarity of the solvent. It was seen that the friction coefficient and adhesion were similarly reduced in liquid environment due to the loss of the water meniscus, which dominates the adhesion under ambient conditions. However, using ultrasonic force microscopy, the few layer graphene was observed to be more relaxed in liquid environment with increased contact to the interface. The lowest adhesion was measured in the nonpolar dodecane solvent, although higher friction was measured in dodecane over water. This was attributed to a ~2 nm thick solid-like cushion structure between the

tip and few layer graphene in dodecane and it was concluded to be responsible for the increased friction.[58]

Although mechanical exfoliation is suitable for fundamental nanoscale studies, it is not sufficient for bulk processing and over the years the quality of other fabrication methods such as CVD of graphene has improved which is more suitable for applications.[59, 60] However, since the tribological properties of graphene depend on the substrate it is fabricated on and transferred to, fundamental studies of the frictional properties of graphene on these substrates are also important. A recent study of CVD graphene grown on copper foil demonstrated a layer dependence of friction between bilayer and single layer graphene. The puckering effect was again observed and found to have a strong dependence on the normal force and sliding history with larger deformations observed at larger loads indicating a weak interaction with the underlying copper substrate.[61] In the case of CVD graphene grown on Ni(111), it was found that the graphene-Ni(111) interface has a strong interaction due to the covalent bonding character and is more rigid with respect to out-of-plane deformations with lower shear strength and work of adhesion compared to graphene on amorphous silica.[57]

Alternatively, graphene oxide films have also been considered as friction modifiers for MEMS devices. Since these films are known to have defects and contain an overall negative charge, the adhesion and friction are affected differently than pristine graphene coatings. This is especially important for devices containing electrical contacts, as it was found that when an AFM tip with a positive charge slides over the

graphene oxide films, the charges are polarized creating an attractive electrostatic forces resulting in increased adhesion and friction until a saturation point is reached.[62]

1.3.2 Micro/Macrotribological Studies of Graphene

Microscale tribological experiments, using a microtribometer, on graphene coated SiC-6H(0001) showed that graphene quickly delaminates from the substrate exposing the interfacial layer with twice the measured friction (Figure 1.6). This is due to the fact that the graphene is weakly adhered to the substrate and can easily be sheared off at points of high pressure such as step edges meaning that although graphene can reduce the friction, low loads and smooth surfaces are ideal to maintain the graphene coating.[14]

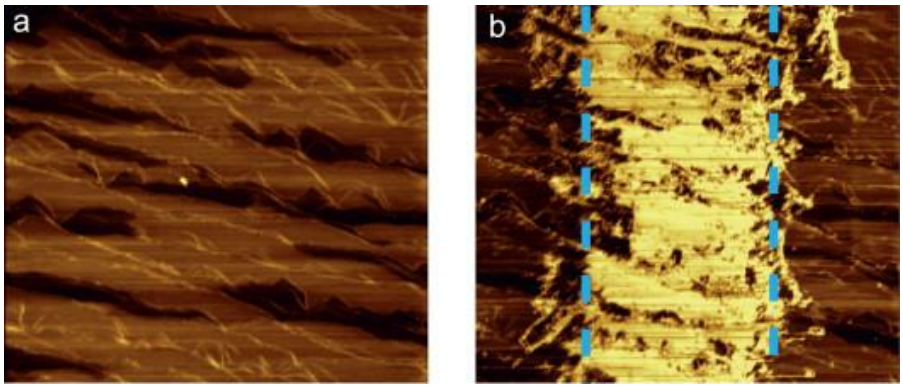

Figure 1.6. AFM friction maps of the graphene-covered SiC surface before (a) and after (b) a microtribological experiment. Dark areas indicate low and bright areas high friction. The images have a width of 20 μm, the color scale ranges from 1 nN to 12 nN. The dashed lines in (b) indicate the estimate of the contact diameter. Reprinted with permission from Ref.[14] Copyright 2013, Elsevier.

Similar results were found when macroscale tribological experiments, using a high vacuum tribometer with a ball on disk contact geometry, were tested on few layer graphene/steel surfaces. A non-continuous film of graphene flakes (25 % coverage) was deposited on the substrate from an ethanol solution. The coefficient of friction was stabilized around 0.18, approximately six times lower than the uncoated steel surface showing good friction reduction even under dry nitrogen environment unlike bulk graphite samples. Analysis of the wear tracks from long sliding cycles revealed a reduction in wear by two orders of magnitude on the graphene coated substrates compared to the bare steel. Load studies from 1 - 5 N, shown in Figure 1.7, indicated better durability under low loads lasting the full 2000 cycles, while at higher loads the

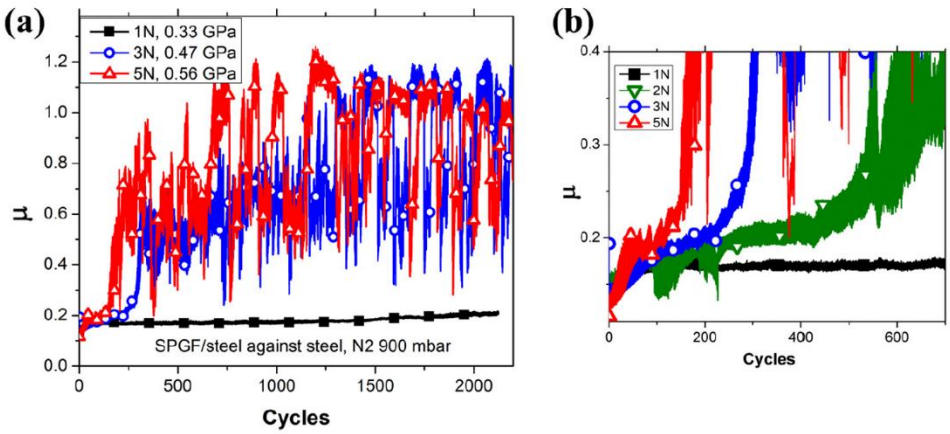

Figure 1.7. Coefficient of friction for steel with solution processed graphene flakes (SPGF) under different loads (a) for 2000 cycles; (b) represents magnified view for initial cycling period. The average Hertz contact pressure is presented for every applied load. Reprinted with permission from Ref.[63] Copyright 2013, Elsevier.

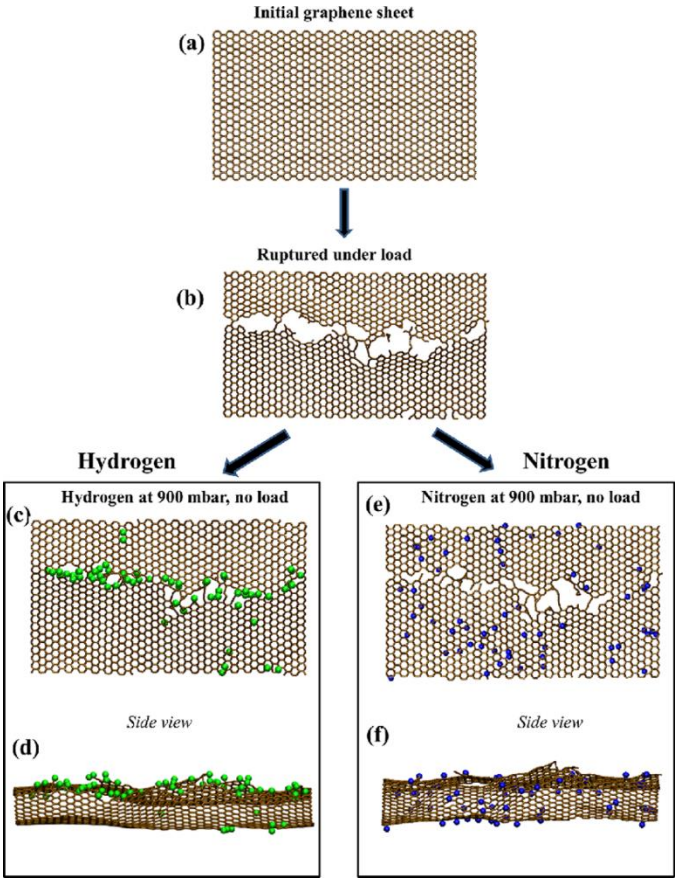

Figure 1.8. Graphene modification under different gas environments. Hydrogen environments afford capping of dangling bonds (hydrogens in green), while nitrogen atmospheres (nitrogen in blue) do not and show not preferential bonding to defect sites. Reprinted with permission from Ref.[64] Copyright 2014. Wiley-VCH

interface suffered immediate high friction and wear due to the removal of the graphene layers from the track.[63]

Most recently Berman *et al*. have shown that stabilization of graphene films can be observed when the gaseous environment in which the wear is occurring is controlled.[64] From a combination of experimental and computational studies they demonstrated that when wear experiments were conducted in hydrogen versus nitrogen

environments, wear could be dramatically impeded when in hydrogen. From the computational studies it has been proposed that under hydrogen environments, "healing" of defects in the graphene can be achieved as the hydrogen will passivate dangling bonds and defects in the film, whereas in nitrogen, no reaction with the graphene films occurs (Figure 1.8). The hydrogen is also purported to suppress oxide formation in the steel surfaces studied.

Along with other large scale fabrication techniques, graphene oxide presents an alternative solution based method for deposition of graphene films. Graphene oxide (GO) may be reduced to form graphene as well as offer alternative hybrid composite films for tribological applications due to its chemical reactivity and good solvent dispersion. Macroscale tribological studies between a sintered tungsten carbide ball and

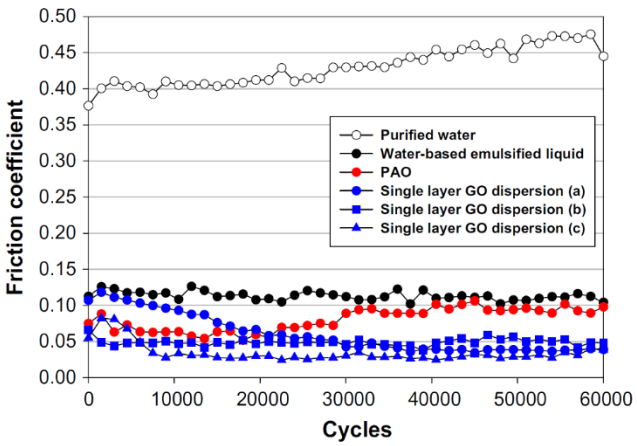

Figure 1.9. Variations of friction coefficients lubricated with purified water, the water-based emulsified liquid, polyalphaolefin (PAO), and the graphene oxide (GO) dispersion, as a function of friction cycles, between the WC ball and stainless steel flat plate under the load of 1.88 N. Reprinted with permission from Ref.[65] Copyright 2013, Elsevier.

stainless steel substrate have shown that 1 wt. % of graphene oxide in water can sustain low friction up to 60,000 cycles with a friction coefficient as low as 0.05 (Figure 1.9), likely due to the continuous replenishment and adsorption of flakes from the solution.[65]

The chemically reactive functional groups on graphene oxide (typically, -OH, -COOH and epoxide) have also been utilized to form thin films by which graphene is covalently bound to the substrate to overcome its intrinsic adhesion and debonding from substrates where graphene is only stabilized by van der Waals forces. These films can then be interfaced with other mobile lubricants as friction reducers and the immobilized graphene layers as the wear reducers. This idea has already been proven effective where graphene oxide was immobilized on substrates layered with multiply-alkylated cyclopentanes and C_{60} and microtribological tests using a ball-on-plate tribometer were performed.[66, 67] In both cases the synergistic effect of the hybrid films allowed for good

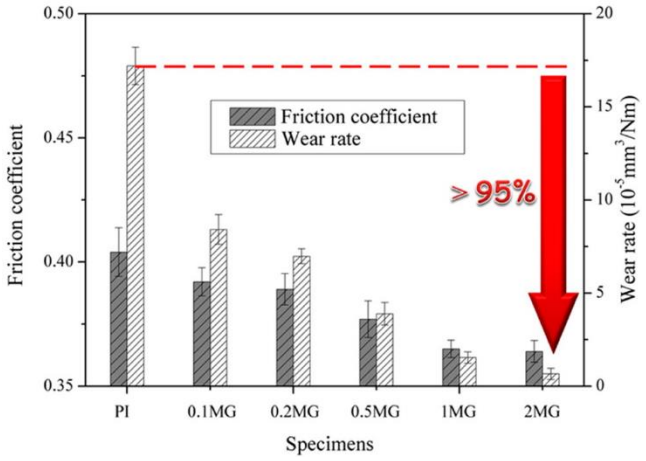

Figure 1.10. Friction coefficient and wear rate of neat polyimide (PI) and various weight percent values of modified graphene (MG) /polyimide specimens. Reprinted with permission from Ref.[68] Copyright 2013, American Chemical Society.

friction and wear resistance due to the replenishing of the mobile lubricants and rolling of the C_{60} combined with the mechanical resistance of the graphene oxide. Additionally, graphene flakes have been utilized as filler additives to form nanocomposites and enhance the matrix properties including the friction and wear resistance. In one recent example, modified graphene/polyimide nanocomposites prepared through surface modification of the graphene and *in situ* polymerization showed enhancements in thermal stability, electrical conductivity, mechanical and tribological properties. It can be seen in Figure 1.10, when 2 wt. % modified graphene was used in the nanocomposites the friction coefficient was reduced by 12% and the wear rate decreased by 95% (20x increase in wear resistance) compared to polyimide without the modified graphene.[68]

1.3.3 Layered Nanomaterials

It is clear that graphene is currently a hot topic in tribology research, but it has also opened up interest in similar 2D nanomaterials as well. Other well-known lamellar materials such as h-BN, MoS_2, and WS_2 are now starting to be investigated as single and few layer coatings. Recently it was shown, using mechanical exfoliation, that these materials exhibit a similar nanoscale friction mechanism despite having different electronic compositions and properties. As in the case of graphene, thin 2D single and few layer sheets of h-BN, $NbSe_2$, and MoS_2 also show the characteristic "puckering effect" which results from weak adhesion to the silica substrate and is a universal concern for materials of this type.[33] Although this research highlights the possibility of non-graphene 2D coatings, little work has been done to explore and take advantage of

the unique properties these materials have to offer. Single layer hexagonal boron nitride has received slightly more attention recently when the tribological properties of CVD grown single layers on copper were investigated. The performance of the monolayers showed excellent friction reduction (up to 40x lower) as compared to the bare copper surface.[69] It is notable that in addition to friction modification, both CVD graphene and hexagonal boron nitride also have the ability to protect metallic interfaces against oxidation[70, 71] however, hexagonal boron nitride can sustain much higher temperatures before oxidizing, making it more desirable for high-temperature applications than graphene.

Unlike graphene where numerous fabrication methods have been explored and optimized these alternative materials are typically sputter coated or produced in the form of nanoparticles. Nanoparticles have been studied for many years and are of interest due to their ability to be used as solid lubricants, additives in liquid lubricants such as oils, and incorporated into nanocomposites. When combined with other friction modifiers, the nanoparticles offer unique advantages in that they are more environmentally friendly while maintaining good friction and wear reduction. In particular, when materials such as transition metal dichalcogenides (MoS_2, WS_2), which are well known for their friction reducing properties in bulk form, are scaled down to the nanoscale the good frictional properties are maintained but the mechanisms are different when used as nanoparticles as compared to 2D lamellar sheets.

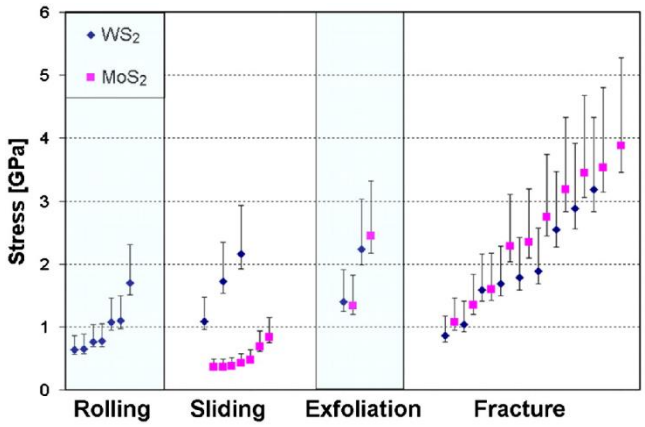

Figure 1.11. The stress values in ascending order, for the three main mechanisms and the fracture stress of IF-WS_2 and IF-MoS_2. 'IF' refers to inorganic fullerene-like nanoparticles of tungsten disulfide (WS_2) and molybdenum disulfide (MoS_2). Reprinted with permission from Ref.[72] Copyright 2011, National Academy of Sciences.

The origin of these excellent nanoparticle tribological properties has been extensively studied over the years and hypothesized to consist of three possible mechanisms including rolling, sliding, and exfoliation. These mechanisms have since been observed by *in situ* transmission electron microscopy and scanning electron microscopy imaging[72, 73] coupled with a nanoindentor/nanomanipulator and were shown to depend on the normal and shear stress as summarized in Figure 1.11. It was found that rolling of the nanoparticles occurs at low shear rates and pressures, which depends on the spherical shape of the particle and their mechanical stability. The sliding of nanoparticles is also dependent on the mechanical strength as well as the amount of interfacial adhesion. In the case of exfoliation, which is typically the dominate mechanism, the outer layers of the nanoparticle delaminate under higher shear stress and pressures. The generated nanosheets are transferred to the contact region and align in

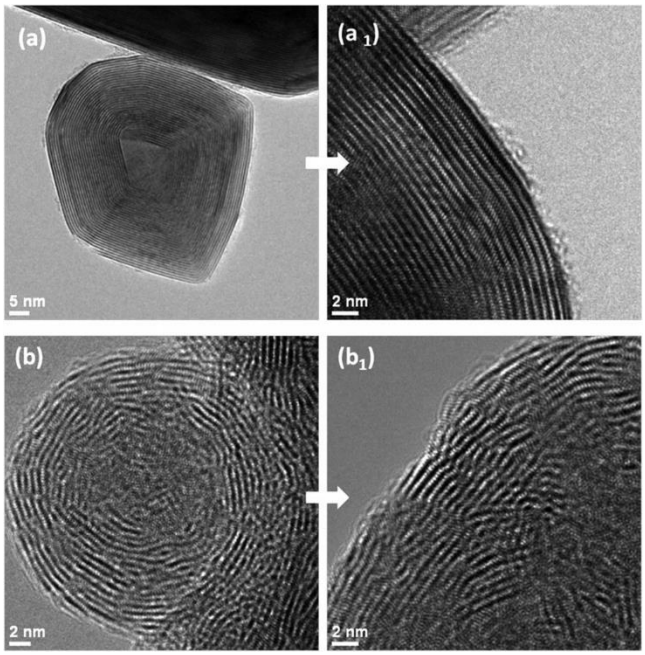

Figure 1.12. High-resolution transmission electron microscope images of (a and a1): perfectly crystallized IF-MoS_2 nanoparticle (namely IF-MoS_2-C) and (b and b1): poorly crystallized IF-MoS_2 nanoparticle (namely IF-MoS_2-A). Reprinted with permission from Ref.[73] Copyright 2013, John Wiley & Sons, Ltd.

the direction of sliding thereby reducing friction through formation of a tribofilm. The efficiency of the exfoliation was studied by comparing MoS_2 nanoparticles with high and low degree of crystallinity (Figure 1.12). When there are more defects present in the nanoparticles, as in the case of low crystalline structures, the exfoliation is immediately observed in the high resolution transmission electron microscopy images (Figure 1.13), allowing for better friction reduction.

These *in situ* nanoscale studies help to visualize and correlate the friction mechanisms of nanoparticle additives to large scale friction studies. Macroscale ball-on-

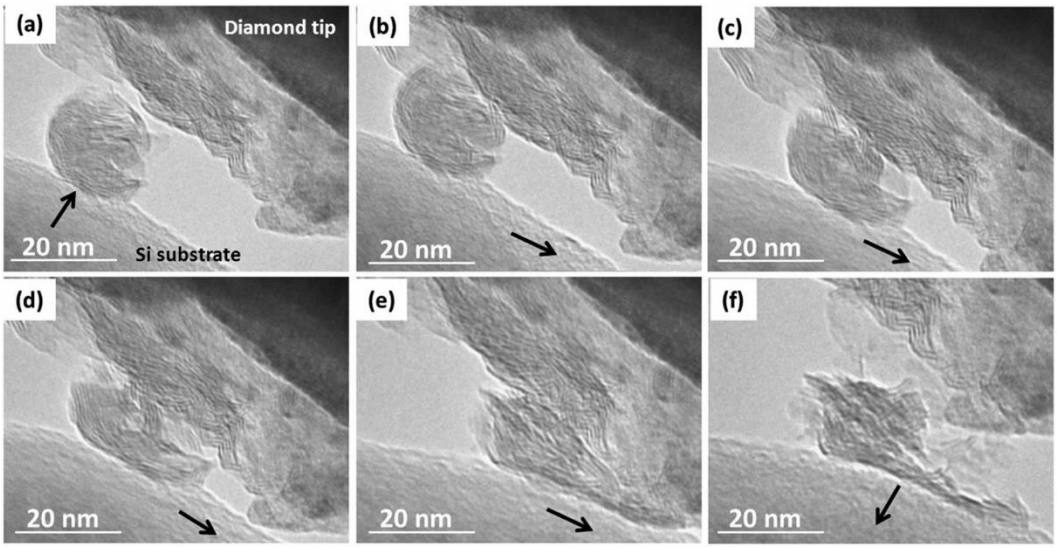

Figure 1.13. Image captures obtained from a video recorded during a sliding experiment carried out with a single poorly crystallized IF-MoS_2 nanoparticle (IF-MoS_2-A) demonstrating exfoliation. The black arrow on the Si substrate indicated the direction of the movement of the Si substrate. Reprinted with permission from Ref.[73] Copyright 2013, John Wiley & Sons, Ltd.

disc studies of 1 wt. % MoS_2 and WS_2 nanoparticles in polyalphaolefin (PAO) on steel have shown that the additives are able to reduce the friction coefficient and wear due to formation of tribofilms.[74, 75] Analysis of the tribofilms revealed exfoliated lamellar sheets and embedded nanoparticles indicating the deformation and exfoliation of the nanoparticles was important for the friction reduction. The effect of crystallinity on the MoS_2 nanoparticles was also investigated and the results were consistent with the TEM experiments with the poorly crystallized particles having a slightly better performance and the lowest friction coefficient as seen in Figure 1.14. The well crystallized particles were observed to have a continuous decrease in the coefficient of friction as well as an inhomogeneous tribofilm while the poorly crystallized particles generated a more

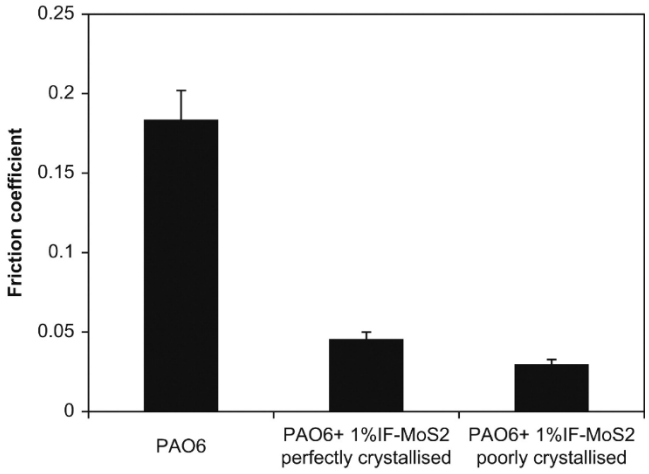

Figure 1.14. Friction coefficient of PAO6, PAO6 + 1 wt% of perfectly crystallized IF-MoS_2 and PAO6 + 1 wt% of poorly crystallized IF-MoS_2. Reprinted with permission from Ref.[74] Copyright 2012, Elsevier.

homogeneous tribofilm and a faster reduction in the coefficient of friction, as expected, due to having more defects and easier exfoliation.

1.3.4 Nanoparticle Additives

Nanoparticle additives are promising but not without limitations, especially since they are known to have issues with dispersibility and agglomeration that must be considered. However, these nanomaterials also offer a degree of tune-ability to overcome these drawbacks. For example, the morphology of the nanoparticles can take a variety of forms including spherical particles, hollow nano-vesicles, nano-platelets, and nanotubes. In one comparison between MoS_2 vesicles and platelets it was found that the vesicles performed better, both lowering the friction and improving wear resistance due to exfoliation which occurs at lower pressures (~31x less than inorganic fullerene like nanoparticles). The poor performance of the nano-platelets was attributed to their higher

tendency to precipitate as compared to the vesicles, which inhibits their ability to enter the contact and reduce friction.[76] In another case, the composition of the MoS_2 particles was studied by doping the inorganic fullerene-like nanoparticles with rhenium. The particles were observed to be more stable and less likely than the 2H-MoS_2 to precipitate, even at higher temperatures. This increased stability was likely due to reduced agglomeration and directly attributed to the effectiveness of the nanoparticles at lowering friction as compared to the base PAO oil.[77]

Although it is clear that nanoparticles are an effective means of reducing friction and wear while offering some flexibility for tailoring the properties for optimal performance under various conditions, it is useful to have a direct comparison of

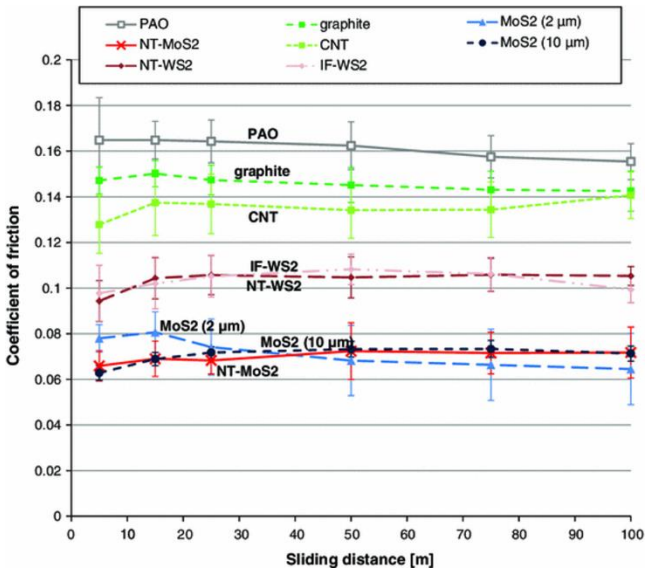

Figure 1.15. Coefficient of friction as a function of sliding distance for the base oil ('PAO') and the base oil with the addition of 5 wt% of various solid lubricant particles. Reprinted with permission from Ref.[78] Copyright 2014, Springer.

particles with different sizes, morphologies and material composition. A recent study, using a ball-on-disc tribotester, has provided such a direct comparison between seven different particles including MoS_2 nanotubes and platelets, WS_2 nanotubes and inorganic fullerene like nanoparticles, graphite platelets and multi-walled carbon nanotubes in PAO on steel. The evolution of the friction coefficients during sliding for the various materials can be seen in Figure 1.15. The coefficients of friction are closely related to the types of material with the MoS_2 particles showing the best performance. Further wear loss experiments indicated the MoS_2 and WS_2 particles had the best wear reduction followed by the carbon nanotubes while the graphite platelets offered the least wear resistance. In this case, there was no dependence of the friction coefficients on size or morphology found, but it is noted that smaller particles have an intrinsic advantage in the ability to be more easily dispersed in the oil lubricant.[78]

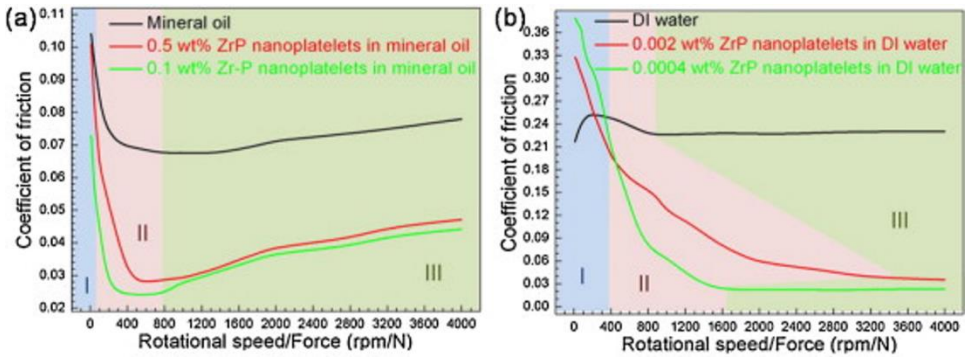

Figure 1.16. Stribeck curves of varying concentration of α-zirconium phosphate (ZrP) nano-platelets in mineral oil (a) and water (b). Adapted with permission from Ref.[79] Copyright 2014, Elsevier.

Akin to those studies carried out on graphene, MoS_2 and h-BN, a host of other layered materials are being explored as friction modifiers. These include materials such as phosphates and layered oxides. Recently, Liang and co-workers have explored the use of Zr phosphate nano-platelets and yttrium oxide nanosheets (Y_2O_3) as additives for lubricants as well as abrasive additives for processes such as chemomechanical planarization.[79, 80] As with many of the above describe platelet systems, the Zr phosphate nano-platelets (on the order of 30 nm in thickness and 600 nm– 1000 nm in length) can be incorporated into oil or water based lubricants as an additive with loadings ranging from 0.0004 wt. % - 0.5 wt. %, which showed decreases in friction from anywhere from 65% to 91% (Figure 1.16). These results are especially interesting as the use of materials such as Zr phosphate provides a green alternative to the production of lubricant additives as compared to materials such as MoS_2, as these materials are basically clays. The resulting dramatic reduction of the coefficient of friction is attributed to two primary factors: the layering of the lubricant molecules along the platelet materials and the orientation of the platelets in the compressed sliding contact.

1.4 Outlook

The design of new friction modification and lubrication additives through the use of nanomaterials represents some unique and challenging opportunities across a range of systems. Clearly we see on the nanoscale the need to design interfaces that can achieve non-commensurate sliding conditions to minimize stick-slip. Computational studies can effectively guide the design of nanomaterials through chemical modification and

combination, striving to minimize sliding strain and facilitate escape from the commensurate to incommensurate state. From the standpoint of additives, we can already see how the combination of nanomaterials in oils can offer new approaches to enhancing the friction reduction capabilities of typical liquid lubricants. Here advances in solubility, dispersability and particle degradation can play a major role in their efficacy. Similar solutions may be on the horizon for biological systems using materials such as graphene oxide, whose functionalization can make these materials water soluble allowing GO platelets to be incorporated with aqueous based lubricants for joint structures.

CHAPTER II

THE INFLUENCE OF NANOSCALE ROUGHNESS AND SUBSTRATE CHEMISTRY ON THE FRICTIONAL PROPERTIES OF SINGLE AND FEW LAYER GRAPHENE*

2.1 Introduction

Since its discovery in 2004,[6] graphene has revolutionized a new field of study in two-dimensional nanomaterials. Although the structure of graphene is a simple honeycomb carbon lattice, it has unique electronic and mechanical properties including ballistic electron transport,[7] high thermal conductivity,[8] large in-plane elastic modulus[12] and a low coefficient of friction.[13-15] These diverse properties expand the field of applications for graphene to include composite materials,[16] energy transfer[17] and storage,[18] electronic[19] and mechanical devices,[20] and solid-state lubrication.[13-15, 33]

Utilizing graphene in real devices however can be limited by the variability of its electronic and mechanical properties, which strongly depend on the interfacial interaction with the underlying substrate.[24, 25] Due to its high out-of-plane flexibility, the morphology of graphene is largely dictated by the geometry of the substrate on which it is deposited, which influences the measured properties through changes in electronic structure, topological defects, and chemical doping effects.[26, 28-31, 81] For example, graphene grown by chemical vapor deposition (CVD) on a copper

* Reprinted from Spear, J. C.; Custer, J. P.; Batteas, J. D. *Nanoscale* **2015,** 7, (22), 10021-10029 with permission from the Royal Society of Chemistry.

catalyst demonstrated improved quality (decreased defects) when a smooth, polished surface was used as compared to a rough one.[82] Subsequently, the electronic properties of graphene were greatly enhanced on the smoother surface with higher measured hole mobility being attributed to the reduction of carrier scattering.

The frictional properties of graphene have also been reported to have a dependence on the substrate morphology and interfacial adhesion. On thermally grown silicon oxide, exfoliated graphene exhibited a "puckering effect" and a significantly increased measured friction for single-layers as compared to multi-layers and bulk graphite. However, when exfoliated onto atomically flat mica, the "puckering effect" was suppressed due to increased adhesion at the graphene-mica interface.[33] Cho and co-workers further studied the effect of surface morphology on the friction and adhesion of graphene and found that when graphene was folded from the silica substrate, the surface corrugations were preserved.[32] This resulted in an enhanced friction on the graphene even when folded onto a flat substrate due to the decreased contact with the surface and lowered interfacial adhesion. These findings imply that strong adhesion to the substrate as well as good conformity are required for optimal frictional properties on graphene and that even small atomic scale roughness can decrease the interfacial binding.

In real devices, the nanoscopic morphology of surfaces can further amplify the effects of substrate interactions and warrant significant study. To address the challenges of graphene's substrate mediated properties, a complete fundamental understanding of the various interfacial interactions is needed in order to control the morphology and thus the properties of graphene. Studying surfaces with nanoscale roughness would aid in

achieving this goal and is of particular interest for using graphene as a protective coating for microelectromechanical system devices, which exhibit nanoscale surface roughness on the order of 10 nm.[83] The interaction between graphene and structured surfaces has been studied predominately theoretically and found to be quite complex, involving an energy balance between the surface geometry, chemistry, bending energy and lattice strain.[84-90] These factors are critical in determining the morphology of graphene on such surfaces and can lead to a range of configurations from fully conformed to lying flat over the surface,[91] which would also affect the frictional behavior. The work in this paper centers around investigating the morphology and tribological properties of graphene exfoliated onto hydrophilic and hydrophobic nanoparticle films with controlled nanoscale roughness, to examine the interfacial interactions and resulting frictional and mechanical properties of graphene on such roughened surfaces.

2.2 Materials and Methods

2.2.1 Sample Preparation

Substrates with controlled nanoscopic roughness were prepared from a modified procedure found in the literature[92, 93] by spin-coating 20 nm diameter silica nanoparticles (Ludox) onto clean Si(100) score cut wafers (Virginia Semiconductor). A nanoparticle concentration of 6 wt% in high purity H_2O (18.2 MΩ·cm, Barnstead), and spin-coating parameters (400 µL, 2000 rpm, 2 min) were used to yield a film thickness ~ 90 nm. The nanoparticle films were then annealed in a kiln at 500º C for 5 hrs and unfunctionalized surfaces were then treated with UV/ozone before graphene transfer onto the particulate

film to yield hydrophilic surfaces. This optimized film thickness provided exceptional optical contrast for observing the locations of the deposited graphene sheets.

To create hydrophobic surfaces, the particle films were silane functionalized with octadecyltrichlorosilane (OTS). The samples were first cleaned and hydroxylated with a 4:1:1 (v/v/v) solution of high purity H_2O (18.2 MΩ·cm, Barnstead), concentrated NH_4OH, and H_2O_2 (30%) for ~15 min at 85ºC (Caution: Piranha solution is highly corrosive and reacts violently with organic matter). The samples were rinsed with nanopure water, ethanol and dried with streaming nitrogen. Substrates were functionalized by sonicating (90 min) in ~1 mM OTS (Gelest)/hexanes solution and stored overnight (12 – 24 hrs). They were then sonicated in tetrahydrofuran, dried with nitrogen and characterized with FTIR Spectroscopy before graphene transfer.

As transfer of graphene by the Scotch tape method[6] was found to be of limited utility on these rough surfaces, we utilized a modified transfer approach as described here. Water soluble tape (3M) was used to exfoliate HOPG (K-Tek Nanotechnology) and transfer the flakes to the sample substrates. The tape was then dissolved in warm high purity water (85º C) and rinsed with high purity water. The samples were then dried with streaming nitrogen and stored in a desiccator overnight. To create graphene, the water soluble tape was again used to cleave part of the graphite from the surface leaving behind small areas of single and multi-layer graphene.

2.2.2 Fourier Transform Infrared (FTIR) Spectroscopy

Sample spectra were recorded with a Thermo Nicolet 6700 FTIR equipped with a liquid nitrogen-cooled MCT (HgCdTe) detector and a Harrick Scientific horizontal

reflection Ge-attenuated total reflection accessory (VariGATR, incidence angle 65º). A semispherical Ge crystal was used as the optical element. Spectra were collected with 128 scans at a resolution of 1 cm^{-1} for the backgrounds and OTS functionalized samples.

2.2.3 Raman Microspectroscopy

A commercially available confocal Raman microscope (WITec Alpha 300R, Germany) was used for locating and characterizing single and multi-layer graphene regions under ambient conditions (20-25 ºC). The microscope was equipped with an Acton triple grating spectrometer interfaced with an Andor Peltier cooled (-65 ºC) CCD detector and a 488 nm Ar ion laser with a laser spot size of *ca.* 300 nm focused with a Nikon high numerical aperture objective (100x, 0.9 NA). The spectral resolution used was ~ 3 cm^{-1}. The laser power for all measurements was maintained below 1.5 mW.

2.2.4 Atomic Force Microscopy (AFM)

Samples were imaged by AFM (Agilent 5500) with silicon tips (Mikromasch CSC37 for contact mode and Aspire CT170R for tapping-mode) under ambient conditions (45% RH - 55% RH and 20 ºC - 25 ºC). The contact mode tips had force constants ranging from 0.1 N/m – 0.8 N/m, depending on lever, and the spring constants were independently determined for each with the Sader method.[94] Tapping-mode tips had resonance frequencies in the range of 150 kHz – 210 kHz. Tip radii were determined experimentally from the blind tip reconstruction feature using Scanning Probe Image Processing (SPIP) Software (Image Metrology, Denmark). All images and roughness calculations were also processed with SPIP. Friction and roughness measurements were taken with a normal load of 5 nN on individual graphene layers.

Raw friction data was analyzed by averaging the total lateral signal for each layer using the same tip and measuring all layers *in situ* on each sample for comparison.

2.3 Results and Discussion

As we have previously reported,[95] silica nanoparticles may be fused to silicon wafers to create surfaces with controlled nanoscale roughness, tunable by particle size, which allows for the formation of surfaces that mimic the nanoscale surface asperities often found in real devices[83] but with uniform roughness. Here we have prepared films consisting of 20 nm in diameter silica particles. The deposition of graphene on these rough surfaces was found to be difficult through normal mechanical exfoliation methods due to the stiffness of the graphite flakes and decreased contact area to the substrate.

To increase the transfer yield, water soluble tape was used to first deposit large (millimeter size) graphite flakes which were then partially re-cleaved from the surface,

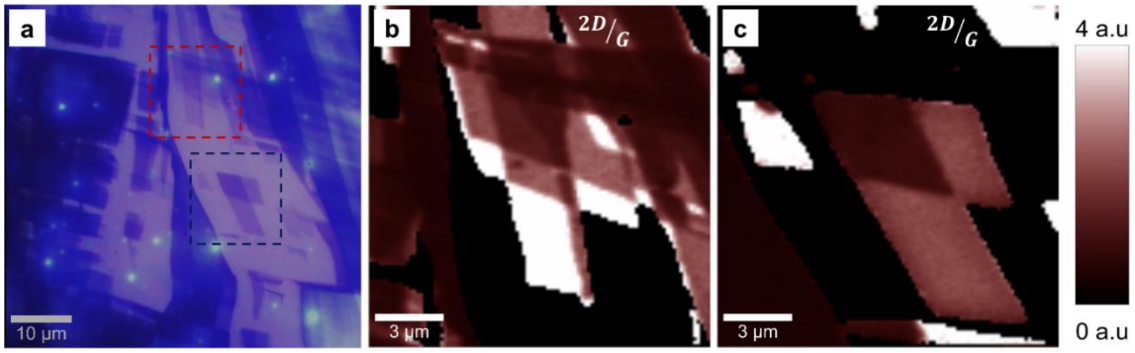

Figure 2.1. (a) Optical micrograph of a sample region on a ~90 nm nanoparticle film with single and multi-layer flakes remaining after cleaving graphite from the surface. The red and blue box indicates the sample regions in (b) and (c), respectively, where Raman maps of the 2D/G peak intensity were taken with graphene having the highest intensity shown as white and graphite as maroon.

leaving thinner flakes with regions of single and few-layer graphene on the surface. Regions of the sample containing graphene layers were located optically and then characterized by Raman microspectroscopy. Figure 2.1a shows a typical optical micrograph where a region of graphite was cleaved leaving single and multi-layer flakes on the surface. The bright "speckles" were found to be large nanoparticle aggregates that formed occasionally during the spin coating of the particle films. Figure 2.1b and 2.1c are Raman maps showing the ratio of the 2D/G bands of the sample regions selected (the red region in Figure 2.1b and the blue in Figure 2.1c) showing graphene as white with the highest intensity ratio, which decreases with increasing thickness up to bulk graphite seen as maroon. These maps were then used to identify specific regions

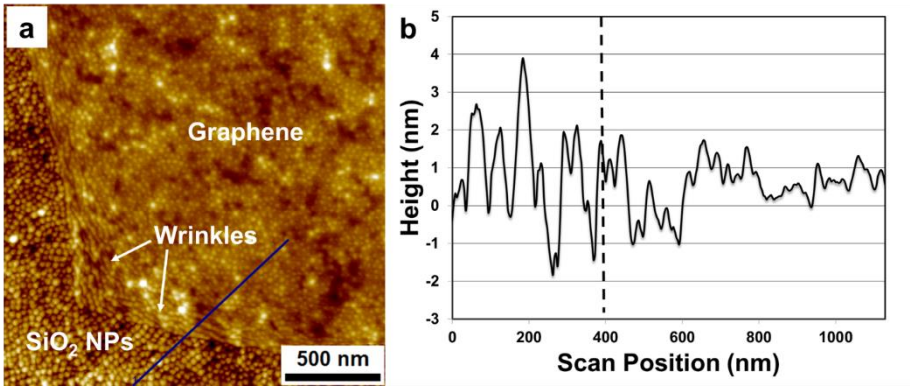

Figure 2.2. (a) Tapping mode AFM topography image of a graphene flake on a rough silica nanoparticle substrate. (b) Line profile from the blue line in (a) showing the partial conformity of the graphene flake to the rough surface due to weak interfacial adhesion. The dashed line indicates the transition from the substrate to the graphene in the line profile.

where the samples could be further characterized and studied using Atomic Force Microscopy (AFM).

2.3.1 Surface Structure of the Graphene Films

The general morphology of the deposited graphene films were investigated first using AFM in both tapping and contact mode. The tapping mode topographic image in Figure 2.2a shows graphene lying over the crests of the rough surface with the underlying surface structure still visible due to the flexible nature of the graphene and its partial conformity to the substrate. The degree of conformity can be seen in the line profile in Figure 2.2b which reveals that for these surfaces the film is partially suspended over the surface asperities, as evident by the decreased height of the amplitude (down to *ca.* 1 nm) along the line profile. This behavior is very different from flat surfaces where graphene has been observed to fully conform to even atomic scale roughness.[96, 97] Some small wrinkles seen along the graphene edges were found to originate from intermittent contact with the AFM tip during scanning, likely due to the relatively weak adhesion and decreased contact with the substrate. Here the tip was able to lift up and partially drag the edges of the graphene flake. Under optimized imaging parameters, this wrinkling effect could be minimized, moreover it was rarely observed to occur during contact mode imaging, implying that a brief contact and lifting motion is required to slide the graphene over the rough surface. Although graphene exhibits high out-of-plane flexibility for conforming to surfaces of different geometries, the van der Waals adhesion forces in this case are clearly not large enough to overcome the inherent

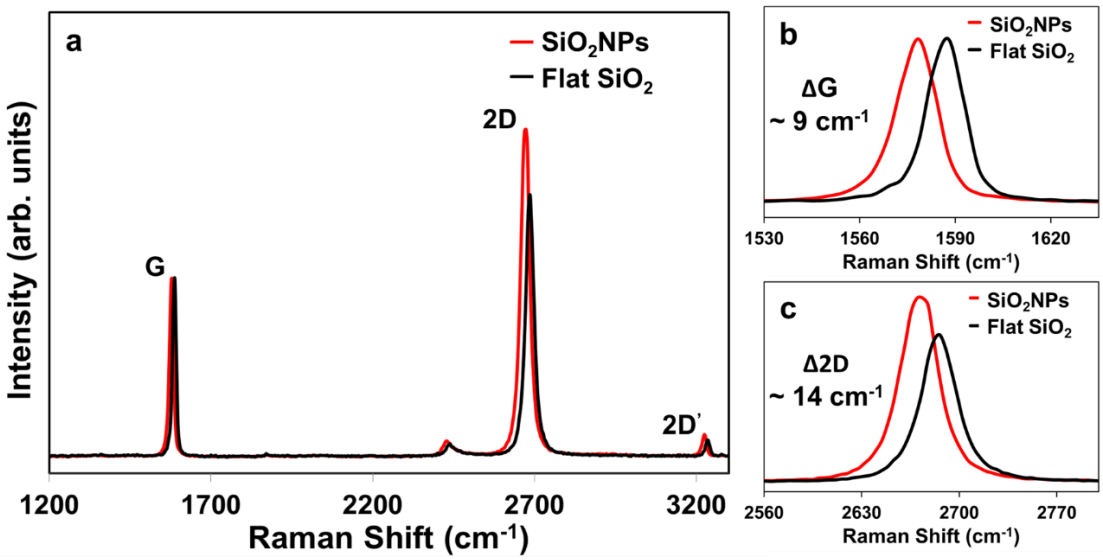

Figure 2.3. (a) Raman spectra of graphene on a rough silica substrate compared to a flat silica surface showing the shift to lower wavenumber on a rough surface due to strain in the graphene lattice. (b) and (c) are larger views of the G and 2D peak shifts. The Raman spectra were normalized to the intensity of the G peak.

in-plane lattice strain imposed by the random distribution of nanoparticle crests on the surface to allow for a fully conformed state to be stabilized.

2.3.2 Raman Spectral Mapping of Graphene Strain

Raman microspectroscopy was used to confirm the presence of lattice strain as a critical factor in the resulting morphology of graphene on these rough surfaces. Raman is known to be sensitive for measuring the strain due to the changes in the crystal lattice, which alters the phonon frequencies.[98] To analyze the strain in the graphene induced by the rough substrate, graphene flakes were also exfoliated onto thermally grown SiO_2 on a Si(100) wafer using the same water soluble tape method as a reference sample. A comparison between the Raman spectra from both flat and rough unfunctionalized samples can be seen in Figure 2.3a. On the rough surface the characteristic G and 2D

peaks show a clear shift to lower frequencies. The relative peak positions and widths were obtained by using a Lorentz fitting: on the flat surface the 2D and G bands appeared at ~ 2685 cm^{-1} (FWHM 30 cm^{-1}) and ~ 1587 cm^{-1} (FWHM 13 cm^{-1}) respectively, while on the rough surface the 2D band was observed at~ 2671 cm^{-1} (FWHM 31 cm^{-1}) and G at ~ 1578 cm^{-1} (FWHM 14 cm^{-1}). This yields approximately a 9 cm^{-1} G peak shift (Figure 2.3b) and a 14 cm^{-1} 2D peak shift (Figure 2.3c) between the two. A slight decrease in the 2D/G ratio was also observed indicating the graphene on the flat SiO_2 surface may be slightly more chemically doped, likely due to the increased contact with the substrate.[98] The larger shift in the 2D peak position however, indicates that the shift is dominated by strain instead of chemical doping and is very consistent with prior studies on biaxial strain in graphene.[98-102]

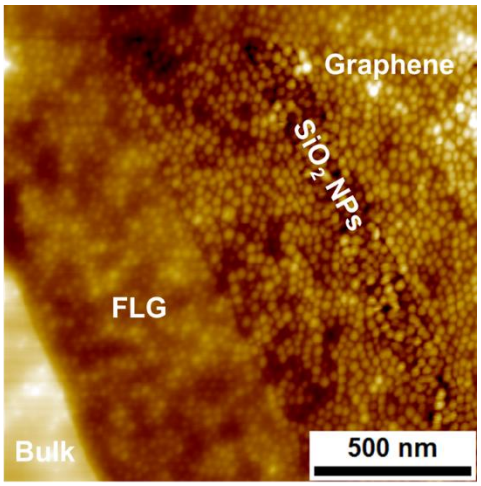

Figure 2.4. Contact mode AFM topography image of the rough silica substrate and graphene layers with different thicknesses and bulk graphite. As the number of layers increased the underlying nanoparticle surface features become less visible due to the increasing stiffness in the layers.

2.3.3 Effect of Thickness and Applied Load on Graphene-Substrate Conformity

Upon examining multi-layered graphene regions, the conformity to the substrate was found to decrease with increasing number of layers or thickness. This can be seen in Figure 2.4 as an obvious reduction in the roughness in the topographic image corresponding to a reduction in the visibility of the nanoparticle film structures. Once the thickness becomes large enough, the morphology appears to be identical to bulk graphite lying flat (rms roughness < 1 nm) over the rough substrate. It should also be noted that the decreasing conformity with increasing number of layers appears to proceed in gradual steps rather than a sharp "snap-through" transition which has been observed on larger corrugated structures.[103] However, the gradual transition can be

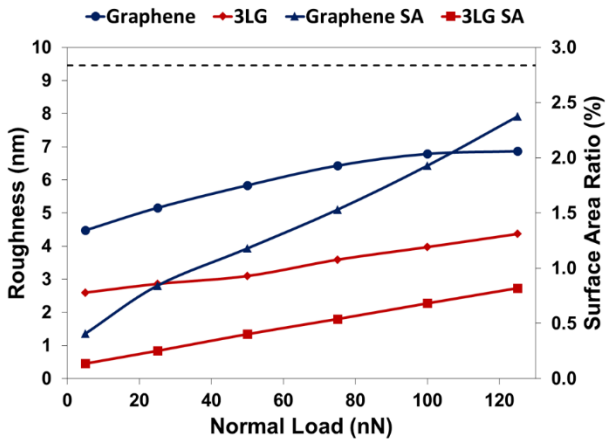

Figure 2.5. RMS Roughness and surface area (SA) ratio as a function of normal load averaged over 1μm^2 scans for graphene and 3-layer graphene (3LG). The dashed line indicates the values for a bare silica nanoparticle surface independent of tip load. Error bars associated with these measurements are smaller than the symbols in the figure.

similarly understood to be due to the increased bending stiffness of the structures with more layers.

The measured roughness and surface morphology of the graphene layers were expected to greatly depend on the imaging load,[104] which increased both the out-of-plane bending and in-plane stretching of the graphene lattice. Using AFM probes with tip radii of ~ 20 nm, the graphene showed increased conformity to the underlying substrate with increased load (Figure 2.5). This change was measured by comparing the calculated roughness and surface area ratio (ratio of the measured interfacial surface area to the area of the projected x-y plane) as a function of normal load. Plotted in this way, the expected range of values start at zero for a flat surface and would maximize at the value measured for a typical rough surface (dashed line), which should be load independent, assuming no wear of the AFM tip. Two cases are shown for comparison: graphene and 3-layer graphene). It can be seen that, for the single-layer case, the roughness increased up to ~ 100 nN of normal tip load and then plateaued around 6.5 nm roughness where the graphene appeared to reach its maximum conformity for this tip size. Beyond 100 nN, the graphene lattice was further stretched and strained as indicated by the continued increase of the surface area ratio. In the case of 3-layers, there was initially some small roughness, which steadily increased with load, but was expectedly lower than the single-layer case due to the added thickness and increased bending stiffness.

Figure 2.6a and 2.6b show topographic images of single-layer graphene at 5 nN and 125 nN imaging load, while Figure 2.6d and 2.6e shows the topographic images of 3-layer graphene at the same loads. As can be readily seen by eye, the images at higher

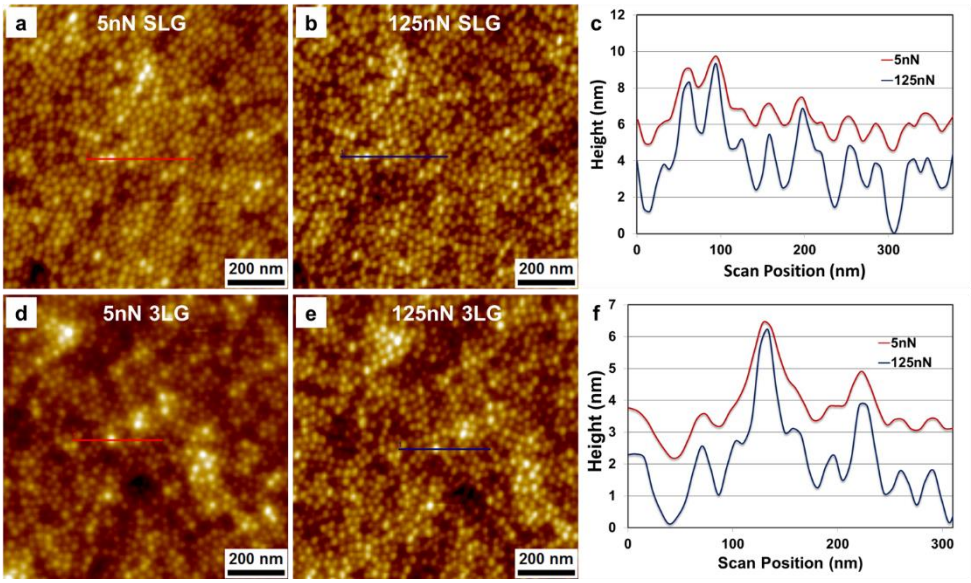

Figure 2.6. Contact mode AFM topography images of graphene at 5 nN (a) and 125 nN (b) and the line profiles (c) from the red and blue lines in (a) and (b). Contact mode AFM topography images of 3-layer graphene (3LG) at 5 nN (d) and 125 nN (e) and the line profiles (f) from the red and blue lines in (d) and (e). The line profiles have been corrected for drift and are offset for easier comparison of the conformity and stretching behavior of the graphene layers under different tip loads.

load appear sharper as the graphene films are compressed onto the substrate. Comparison of the line profiles in Figure 2.6c and 2.6f reveal that the graphene and 3-layer graphene regions are stretched by *ca.* 2 nm – 3 nm and 1 nm – 2 nm, respectively. Even at 125 nN the graphene was unable to fully conform to the surface in comparison to the typical values of ~ 9.5 nm roughness and 2.8% surface area ratio for the unmodified rough silica surface. This implies that even with increased energy from the mechanical tip loading, a fully conformed state was unable to be achieved due to the sharpness of the nanoparticle crests and the elastic restoring energy of graphene to reversibly deform, maintaining minimal strain energy at equilibrium. Using a relatively

simplistic Hertz model[105-107] for the out-of-plane modulus comparing the displacement of the graphene in between the particles at low (5 nN) and high (125 nN) loads, one can estimate the out-of-plane modulus as a simple indentation. Using this model we estimate a modulus of *ca.* ~1 GPa. This estimate however is of course severely compromised by the fact that as the imaging load is increased, the contact is systematically changing from a tip on graphene which limited contact to the substrate to one where the tip-graphene-substrate contact area increases with increasing load. As such a uniaxial load on the center of the graphene by the AFM tip cannot be fully assumed.

2.3.4 The Frictional Properties

Again as real MEMS devices typically exhibit nanoscale roughness of *ca.* 10 nm, the ability of materials to modify the friction of rough surfaces must also be investigated. As such, friction force microscopy was used to evaluate the tribological properties of graphene on these same surfaces. The topography comparing single and bi-layer graphene and the corresponding friction map is shown in Figure 2.7a and 2.7b, respectively. A small variation in roughness can be seen in the topography while no decrease in friction was observed with increasing number of layers. To compare the friction on different regions of the surface, the relative friction signal was averaged from individual friction maps and normalized to the value for bulk graphite, as determined *in situ* from measurements on graphitic flakes (> 5 layers) on the surface. The variation in friction with the number of layers however, was noticeably dependent upon the dimensions of the AFM tip. Figure 2.7c shows the normalized friction values comparing single-layer graphene, bi-layer graphene and graphite collected with both a sharp and

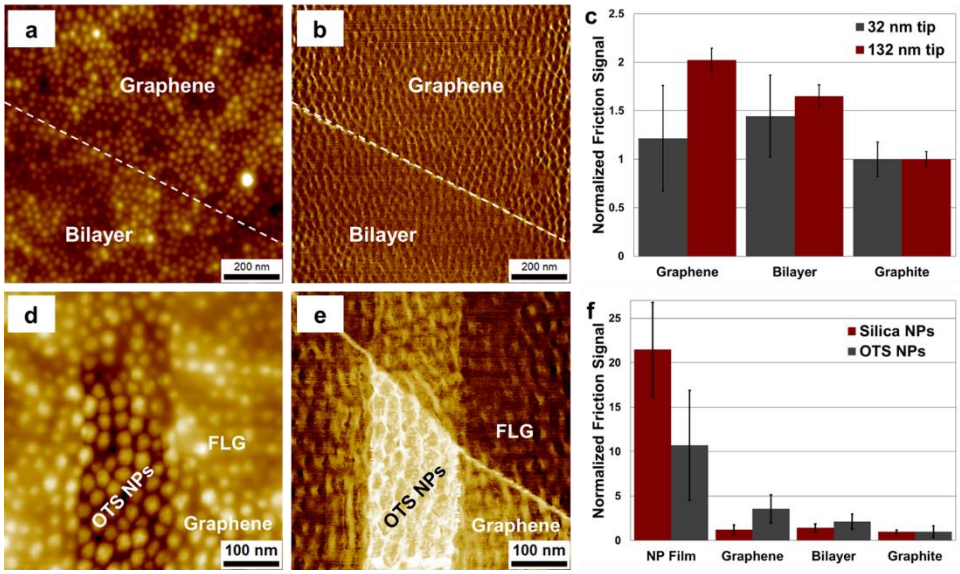

Figure 2.7. Contact mode AFM topography images obtained with a sharp probe (a,d) and friction maps (b,e) of a sample region containing graphene layers on silica and OTS modified nanoparticles, respectively, for comparison of local roughness and friction. (c) Friction values of graphene layers using an AFM probe with a radius of 32 ± 2 nm and friction values of graphene layers using a blunter probe with a radius of 132 ± 17 nm. The friction and roughness values are normalized to that of bulk graphite to show the recovery of the friction trend with a larger AFM probe. (f) Normalized friction values of silica and OTS nanoparticles and graphene layers using an AFM probe with a radius of 32 ± 2 nm. The OTS coated nanoparticles show the typical "puckering effect" with reduced friction combined with graphene, but the overall friction is higher than the graphene on the unfunctionalized surface where the puckering effect is suppressed.

blunt AFM tip. It was seen that with a sharp probe (radius of curvature of 32 nm ± 2 nm) there was not a significant change in friction between single graphene layers up to bulk-like graphite. Although the bi-layer appears to have slightly higher friction than graphene, this is within the error bars which are larger on rough surfaces due to the increased lateral bending of the cantilever (more so with a sharp probe) and generally larger noise associated with the friction measurements on rough surfaces. Further evaluation of the local roughness of the random sample regions taken for average

measurements showed the bilayer had a slightly higher roughness at the low load of 5 nN thus increasing the friction. The result in Figure 2.7c was unexpected since the graphene is weakly adhered and has decreased contact to the surface but seemingly does not exhibit the characteristic "puckering effect" as observed on similarly fabricated flat substrate samples (see Supporting Information Figures A.1-A.2). While high resolution stick-slip images would normally be used to also examine if puckering was occurring, these could not be obtained on these rough graphene surfaces. Adhesion force mapping measurements were also conducted and showed little to no variance in measured adhesion as a function of the number of layers (Figure A.3) indicative that puckering, which on a rough surface we would expect to express itself as layer dependent adhesion, was not occurring.

In contrast to the sharp probe, when a blunted silica probe (132 nm ± 17 nm) with a radius of curvature much greater than that of the surface asperities (~10 nm) of the underlying substrate was used, the friction of single-layer graphene was found to be 50% higher than the bulk and 20% higher than bi-layer, consistent with previous reported values on flat surfaces.[32, 33]

Not surprisingly, these findings indicate that the frictional properties of graphene on such rough surfaces depend strongly on the combined, effective contact area of the sliding interface. When the AFM tip radius is smaller, the total asperity-asperity contact is also smaller and changes smoothly as the tip moves laterally over the nanoparticle asperities. This prevents the graphene from being able to slide over the surface as easily as on flat surfaces, thus suppressing puckering in front of the tip. The larger, blunter

probe simply has a larger contact area thus affording greater adhesion to the probe than to the substrate. The resulting increased shear stress can then induce sliding of the graphene, despite the roughness, and increase the measured friction. This suggests that for rough surfaces, a critical contact area dependence exists which balances the surface forces needed to mitigate this effect and afford good friction modification. One could imagine a blunt enough probe that would allow for multiple asperities to be contacted simultaneously which would balance out the tip-graphene contact area again resulting in the loss of any observed layer dependence, but this would depend on the relative distance between surface asperities as well, and will be the subject of future studies.

2.3.5 Influence of Hydrophobic Surface Interactions

As control of the graphene substrate contact significantly influences the observed friction, in addition to studying graphene on hydrophilic substrates, hydrophobic substrates were also explored to investigate the influence of surface chemistry on the morphology and tribological properties of the deposited graphene. Here the silica nanoparticle films were functionalized with octadecyltrichlorosilane (OTS) and characterized with infrared spectroscopy (Figure A.4). OTS coatings have been previously shown to reduce chemical doping of graphene from the substrate in field effect transistors and it can also provide additional pathways interfacial lubrication.[108, 109] Contact AFM imaging showed that the various graphene layers conform similarly to the OTS coated substrates as they did to the unfunctionalized supports (Figure A.5a), with a similarly observed decrease in roughness with increasing layer thickness (Figure A.5b). As with the unmodified substrates, only partial conformity was observed also due to

strain from the rough substrate which was greater than the added interfacial adhesion. As the surface geometries are nominally the same (with an increase in surface asperities size of at most 10 % due to the added monolayer) the magnitude of the strain was expected to be nearly the same in both hydrophilic and hydrophobic samples. This was confirmed by the observation of similar G (6 cm^{-1}) and 2D (15 cm^{-1}) band peak shifts in the Raman spectra (Figure A.6). The peak positions for graphene exfoliated onto the thermally grown oxide of a flat Si(100) wafer modified with OTS (2D ~ 2689 cm^{-1}, G ~ 1582 cm^{-1}) were also consistent with values for unstrained, undoped graphene (2D ~ 2692 cm^{-1}, G ~ 1582 cm^{-1}) indicating there was very little chemical doping effect from the substrate.[98] In comparison, a slight decrease in the 2D/G intensity was noted for graphene on the OTS modified nanoparticle surface, likely due to the increased disorder in the monolayer on these rough surfaces[110, 111] which results in more collapsed films, yielding slightly decreased buffering from substrate doping.

The largest effect of the functionalized surface was observed in the frictional properties. A significant contrast between the OTS modified nanoparticles, graphene and few-layer graphene can be easily seen in the AFM contact mode topographic image in Figure 2.7d and friction map in Figure 2.7e. The averaged friction signal showed that graphene had lower friction than OTS, but higher friction than bi-layer and bulk graphite on the substrate (Figure 2.7f). These results are also consistent with comparative flat OTS substrate studies, which also showed a very distinct "puckering effect" (Figure A.7 and Figure A.8). In this case, the friction was not found to depend on the contact area since the puckering effect was observed even with a sharp probe resulting in overall

increased friction as compared to graphene layers on the unfunctionalized rough surface. This can be attributed to the slightly larger size of the nanoparticles and increased interfacial lubrication by the OTS film, which reduces the graphene-substrate friction allowing for easier sliding over the surface since the graphene is not strongly bound to the substrate.

2.4 Conclusion

AFM analysis of graphene on surfaces with nanoscale roughness showed that a tightly conformed state was not possible due to the large strain that would be required, leaving graphene weakly adhered at the peaks of the substrate asperities and only partially conformed to the underlying substrate morphology. Conformity to the substrate was also found to decrease with increasing number of graphene layers, but it could be increased under higher applied mechanical loads during imaging, elastically returning to a less conformed state with decreased imaging load. The frictional properties were found to depend on the relative adhesion between the AFM probe tip and the substrate, with suppression of the "puckering effect" under asperity-asperity contact due to the large surface roughness and low adhesion to the tip. With a larger AFM tip which is able to contact multiple asperities at any given time, increased friction on graphene from the increased contact area and shear was observed. Substrate chemistry was also found to modulate the interactions and measured friction, as graphene on hydrophobic OTS functionalized substrates showed a strong affinity for the substrate, but with higher friction for single-layer graphene as compared to multiple layers, and higher friction as compared to graphene on the hydrophilic silica substrate. This increased friction may in

part be due to increased shear strain brought about by the more compliant OTS layer under the graphene as compared to the bare silica support. These findings contribute to the understanding of graphene-substrate interactions by examining the balance between substrate geometry, surface chemistry, graphene bending energy, and lattice strain. They point to an optimal configuration for controlling friction by tailoring of self-assembled monolayers as a buffer layer that can provide additional pathways for energy dissipation in contacts, control over the surface energy and increased binding to rough surfaces. Additionally, utilizing silica surfaces with controlled roughness may provide a platform for using strain as a way to further modulate the electronic properties of graphene and as a means to control the extent of substrate chemical doping effects.

CHAPTER III

THE INFLUENCE OF SUBSTRATE ROUGHNESS ON THE DYNAMIC/ADHESIVE BEHAVIOR OF GRAPHENE

3.1 Introduction

Graphene is an atomically thin nanomaterial composed of a honey comb carbon lattice[6] which has been extensively studied over the past decade and exhibits many unique properties such as high carrier mobility[7] and thermal conductivity,[8] large in-plane elastic modulus,[12] low coefficient of friction[14] and high optical transparency.[112] These properties have drawn significant interest in graphene across a broad range of scientific fields of study and technological applications, including flexible electronics,[113] chemical sensors,[114] energy storage,[18] and nanoelectromechanical systems devices,[115-117] and for modifying surface friction, either as coatings or as lubricant additives.[63-65]

Due to its atomically thin and flexible nature, when deposited on a substrate with relatively small roughness, graphene can closely follow underlying surface structure down to the atomic scale, causing its properties to be strongly affected by its interactions with the substrate. By understanding these fundamental interactions, precise control of graphene's properties and can be achieved. In particular, controlling substrate adhesion, is critical for applications to micro- and nano- electromechanical systems devices,[118] where control of both interfacial friction and electrical and thermal conductivity are important considerations.[119, 120] Studies on the adhesion of graphene to various substrates have been previously investigated through a host of techniques, including

intercalation of nanoparticles,[121] Atomic Force Microscopy (AFM),[122] peel tests[123] and pressurized blister tests[124] with the work of adhesion at the graphene-silica interface being reported to be up to 0.45 J/m^2,[124] although the values vary significantly across the literature.

It is suspected that one of the key factors that influences the variation in reported adhesion values in the literature originates from differences in surface roughness, which varies depending on the type of substrate and sample fabrication methods. In general adhesion is known to vary with roughness but little experimental work has been done to understand this effect on 2D materials such as graphene. Adhesion measurements made by AFM have shown that small changes in the sample roughness[125] (even sub-nanometer roughness) and microsphere tip roughness[126] greatly impact the measured adhesion on graphene and must be taken into account. Another critical factor that must be considered is that because graphene sheets are covalently bonded networks, spatial variations associated with differences in local substrate interactions, make the graphene-substrate interaction dynamic, and this dynamic behavior has yet to be fully explored or accounted for when examining for example, the frictional properties of graphene, which must be dynamically changing during sliding contact. Recent studies by Berman *et al*.[127] have shown that small graphene sheets can bond and de-bond from substrates to create nanoscrolls, but direct images of the dynamic nature of graphene on substrates and in sliding contacts have yet to be fully explored.

Computational studies on graphene on corrugated surfaces have shown that the interfacial adhesion is directly related to the surface structure of the substrate which

affects the roughness of graphene.[84, 85, 128] Previously we have shown that nanoscale roughness can increase the roughness of graphene which can affect the frictional properties.[129] Here we have used thin films composed of different nanoparticle sizes ranging from 6 nm to 85 nm to study the effect of varying nanoscale roughness and surface structure on the adhesion of graphene using AFM.

3.2 Experimental Section

3.2.1 Sample Preparation

Substrates with nanoscale roughness were prepared by spin-coating 85 nm, 50 nm, 20 nm, 12 nm, and 6 nm diameter silica nanoparticles (NexSil aqueous colloidal silica) onto clean Si(100) score cut wafers (Virginia Semiconductor). Nanoparticle stock solutions were diluted with high purity H_2O (18.2 MΩ·cm, Barnstead) to concentrations of 5-6 wt%. Before spin-coating, the solutions were sonicated in water bath for 30-45 min to break up any aggregated nanoparticles to help produce more uniform thin films. To obtain a desired film thickness ~ 90-100 nm, 400 µL of nanoparticle solution was deposited by spin-coating at 2000 rpm for 2 min. By controlling the thickness of the nanoparticle films the optical contrast can also be controlled for locating the exfoliated graphene sheets with the best contrast observed on the films made from smaller particles. The nanoparticle films were annealed in a kiln at 500º C for 5 hrs to dry and sinter the nanoparticles together. The silica substrates were then cleaned with UV/ozone (for ~10 min) before graphene transfer.

Graphene is typically exfoliated by the Scotch tape method[6] but it was found to less effective on these rough surfaces so we modified the method to use water soluble

tape (3M) to exfoliate and transfer graphite (K-Tek Nanotechnology) to the substrates before a second exfoliation to produce graphene. After the first transfer the tape was dissolved in a water bath (85º C) for ~45 sec and rinsed with water from a wash bottle to slowly remove the softened tape residue and only some of the graphite. The samples were then dried with nitrogen and exfoliated again with tape to remove the top layers of graphite leaving some areas of freshly cleaved single and multi-layer graphene. Samples were stored in a desiccator between Raman and AFM measurements.

3.2.2 Raman Microspectroscopy

A confocal Raman microscope (WITec Alpha 300R, Germany) was used for visualizing regions with graphene flakes utilizing the optical contrast provided by the controlled thickness of the top silica layer of the substrate. The samples were characterized with Raman spectroscopy under ambient conditions (20-25 ºC). The microscope was equipped with an Acton triple grating spectrometer interfaced with an Andor Peltier cooled (-65 ºC) CCD detector and a 488 nm Ar ion laser with a laser spot size of *ca.* 300 nm focused with a Nikon high numerical aperture objective (100x, 0.9 NA). The spectral resolution used was ~ 3 cm^{-1}. The laser power for all measurements was maintained below 1.5 mW.

3.2.3 Atomic Force Microscopy (AFM)

Samples were imaged by AFM (Agilent 5500) with silicon tips (Mikromasch CSC37 for contact mode and Aspire CT170R for tapping-mode) and diamond-like-carbon tips (BudgetSensors ContDLC) under both ambient (45% RH - 55% RH and 20 ºC - 25 ºC) and dry nitrogen (<1% RH) conditions. The contact mode tips had force constants

ranging from 0.1 N/m – 0.8 N/m, depending on lever, and the spring constants were independently determined for each cantilever with the Sader method.[94] Tapping-mode tips had resonance frequencies in the range of 150 kHz – 210 kHz. Tip radii were measured by scanning standards with controlled geometry and then calculated using the blind tip reconstruction feature of Scanning Probe Image Processing (SPIP) Software (Image Metrology, Denmark). All images, roughness, and adhesion calculations were also processed with SPIP.

3.3 Results and Discussion

3.3.1 Surface Morphology of Graphene on Substrates with Nanoscale Roughness

To understand the influence of substrate roughness on adhesion of graphene, substrates with controlled nanoscale roughness were fabricated. As we have shown previously,[95] surface roughness can be controlled by spin-coating nanoparticles to create uniform thin films whereby changing the size of the nanoparticles used, the overall roughness can be tuned. Smaller nanoparticles create films with lower roughness and increased numbers of asperity-graphene contact points, while larger particles increase the roughness of the packed films and increase the nearest neighbor peak-to-peak contact distance. The nanoparticle sizes used in this study include 6 nm, 12 nm, 20 nm, 50 nm, and 85 nm, all of which were employed to make thin films composed of the various sizes by spin-coating onto an oxidized Si(100) wafer and then annealing. For comparison to

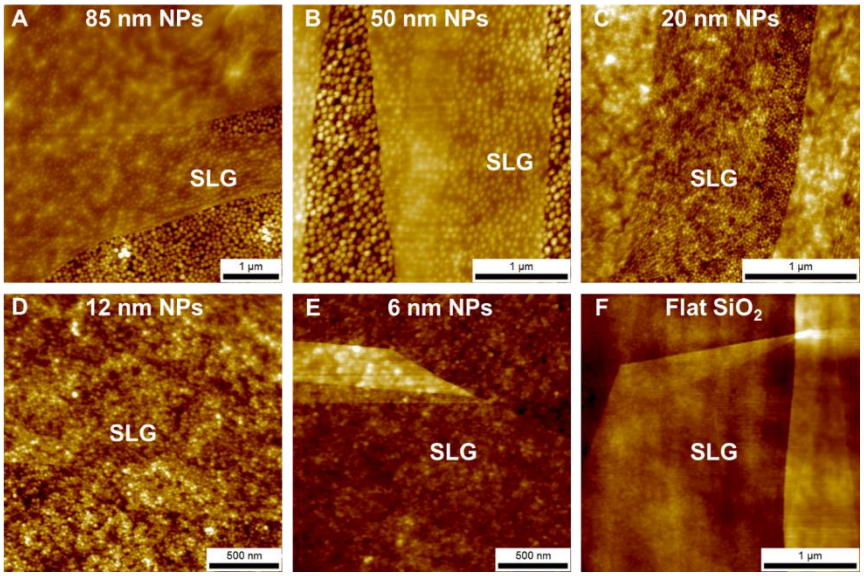

Figure 3.1. Contact mode AFM topography images of monolayer graphene on thin silica films composed of (A) 85 nm nanoparticles (B) 50 nm nanoparticles (C) 20 nm nanoparticles (D) 12 nm nanoparticles (E) 6 nm nanoparticles (F) graphene on 90 nm thermally grown silicon oxide.

the rough substrates, a Si(100) wafer with a thermally grown oxide layer was also used as an atomically flat reference substrate. For simplicity, we will refer to the sizes of the nanoparticles to distinguish between the different samples in this study. After the substrates were prepared and cleaned, graphene samples were fabricated using a water soluble tape method we have previously reported.[129]

Figure 3.1 shows topographic images of single and few layer graphene deposited on surfaces with varying roughness measured by contact mode AFM. Since graphene exhibits a high out-of-plane flexibility, it can be seen to adopt a topographic structure similar to the substrate, such that by changing the roughness of the substrate, the roughness of graphene can also be readily controlled. This has many useful applications

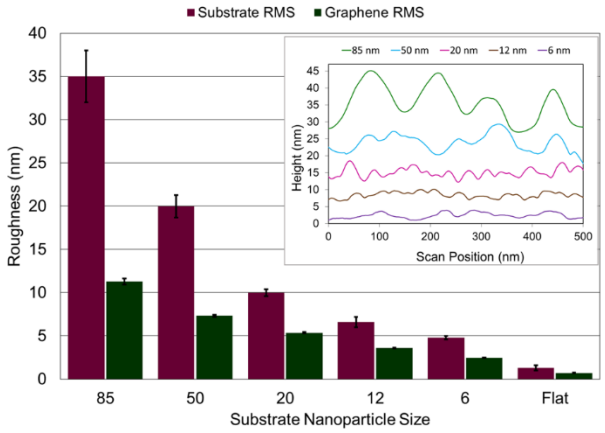

Figure 3.2. RMS roughness calculated from 500 nm^2 regions on the different silica substrates and the corresponding monolayer graphene regions. The inset shows example line profiles extracted from the graphene regions showing the controlled decrease in roughness with changing nanoparticle size from the different samples.

in terms of utilized deformation of the graphene on the support to alter its electronic properties, as has been explored by others.[130] As can be seen in the topographic images for substrates with larger roughness (Figure 3.1A and Figure 3.1B) the graphene adheres to and follows the top-most nanoparticle asperities with regions of suspended graphene in between the peaks. For the substrates with lower roughness the graphene was seen to readily follow the surface structure more closely due to the smaller heights of the nanoparticle asperities and their more closely spaced proximities. The measured changes in roughness for 500 nm^2 regions on the substrate and graphene are shown in Figure 3.2. It is clear that by decreasing the size of nanoparticles used to create the films, the roughness decreases in a consistent and tunable fashion, from ~ 35 nm RMS for the films composed of the 85 nm diameter particles to ~ 1 nm RMS on the bare oxidized Si(100) substrate. A similar trend is also observed for the single layer graphene

flakes but with a smaller magnitude decreasing from ~ 11 nm RMS to ~ 0.7 nm RMS. The decreasing graphene roughness can be visualized in the inset of Figure 3.2 which shows example topographic line profiles taken from single layer graphene regions from where the roughness measurements were taken. In general, graphene conformity to the surface increases as the roughness decreases, although in all samples the graphene roughness was always lower as compared to the substrate due to smoothening by the membrane. The 85 nm sample which has the largest roughness also had the least conformity with a ~70% reduction in roughness on the graphene due to the suspended graphene regions between the valleys of the nanoparticle asperities.

These changes in conformity of the graphene samples are related to a balance between the out-of-plane flexibility, the local interfacial work of adhesion and elastic strain energy. The interfacial adhesion between graphene and the silica nanoparticles is dominated by van der Waals interactions and calculations on flat silica surfaces have shown the adhesion energy to be directly related to conformity and contact between graphene and the surface.[128] In the case of rough silica surfaces it is expected that the interfacial adhesion with graphene would be lowest on the roughest surfaces due to decreased contact area with the substrate. Substrates with lower roughness clearly exhibit increased conformity and thus increased total interfacial adhesion due to the attractive van der Waals forces and high out-of-plane flexibility, but at the cost of increased strain energy. For the films composed of 20 nm nanoparticles (~ 10 nm RMS roughness) this falls in the middle with a distinct partial conformity observed due to the increases in asperity height, but with closer spacing between neighboring asperities,

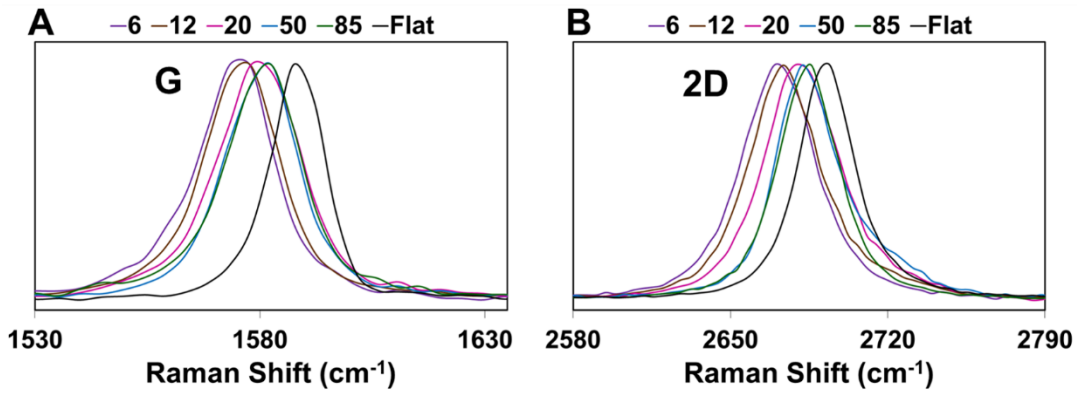

Figure 3.3. Normalized Raman spectra from monolayer graphene with varying sample nanoparticle size. The characteristic G (A) and 2D (B) Raman modes both show increasing shifts to lower wavenumber due to increased strain from graphene conformity to the rough substrates.

making the strain requirement for full conformity larger than the strength of the intrinsic substrate adhesion.

3.3.2 Raman Spectroscopy and Graphene Strain as a Function of Surface Roughness

Changes in the graphene structure due to surface conformity are also expected to lead to changes in the degree of lattice strain. Raman spectroscopy can be used to measure changes in strain[98] as well as chemical doping effects from the substarte.[131] Average single spectra were taken for each sample with the same laser power and are compared in Figure 3.3. As our spot size is *ca.* 300 nm in diameter, spectra are of course convolutions of all areas within that sampling area, but are all of single layer graphene structures. The Raman spectra were normalized to show the trends for the characteristic G (Figure 3.3A) and 2D (Figure 3.3B) graphene peaks and shifts in their position

Sample	2D (cm^{-1})	G (cm^{-1})	Δ2D	ΔG	Γ_{2D}	Γ_G	I_{2D}/I_G
Flat	2693	1588	+1	+6	29	13	1.75
85	2685	1581	-7	-1	31	19	3.3
50	2684	1581	-8	-1	34	19	2.2
20	2682	1580	-10	-2	40	21	2.4
12	2674	1576	-18	-6	38	19	2.2
6	2671	1575	-21	-7	39	19	2.7
Unstrained/ Undoped*	2692	1582	-	-	-	-	-

Table 3.1. Values calculated from the Raman spectra of graphene on different rough substrates and fit with a Lorentzian. The 2D and G peak positions and their shifts from the unstrained/undoped literature reference value.[98] The full width at half max values for the 2D (Γ_{2D}) and G (Γ_G) and the peak intensity ratio (I_{2D}/I_G).

relative to that of single layer graphene on the atomically smooth oxidized Si(100) substrate. It can be seen that the Raman peaks shift to lower wavenumber with decreasing roughness. The peaks were fit with a Lorentzian to obtain approximate peak positions and widths with the results shown in Table 3.1. For rough graphene samples the 2D peak shift is much larger than the G peak shift characteristic of strain dominated spectral shifts.[100, 132, 133] The G peak width is relatively constant while a slight broadening is seen for the 2D peak width with decreasing roughness. It has been previously shown that the intensity ratio of the 2D/G peaks can provide an indication of the degree of chemical doping.[134] The intensity ratios are also shown in Table 3.1 for rough and flat graphene with the highest calculated for the 85 nm sample and the lowest for the flat graphene sample. Due to the shift of the flat graphene spectrum to higher

wavenumber and the lower 2D/G intensity ratio, the spectral shift in that case is dominated by chemical doping effects most likely due to the increased conformity and interaction with the substrate and water trapped at the surface between the silica and graphene.[135]

The peak shifts with decreasing roughness can be understood by considering the changing morphology of graphene and the amount of interaction it has with the different rough substrates and their concerted impact on the extent of strain in the graphene lattice. Graphene deposited on the 85 and 50 nm samples contain many suspended regions which means that the graphene has decreased overall contact area with the substrate due to the longer distances between the peaks of the asperities, resulting in minimal chemical doping and an overall reduced total lattice strain. As the substrate roughness decreases and the conformity of the graphene increases, the graphene has increased strain from out-of-plane deformation and stretching of the graphene due to locally induced radial strain from the particles.[136]

3.3.3 Influence of Roughness on Graphene Adhesion

To investigate the influence of roughness on the adhesion of graphene, force-distance (FD) spectroscopy was used to measure the pull-off force for graphene on the different rough substrates. The samples were measured using a diamond-like-carbon (DLC) AFM tip to prevent tip wear, under ambient environments (~ 40% humidity and 20 ^{o}C), with equivalent sampling parameters (*i.e.* approach and retract rates, peak applied load and data points to acquire). The average pull-off forces as determined from the FD curves for the varying substrates are shown in Figure 3.4. The measured

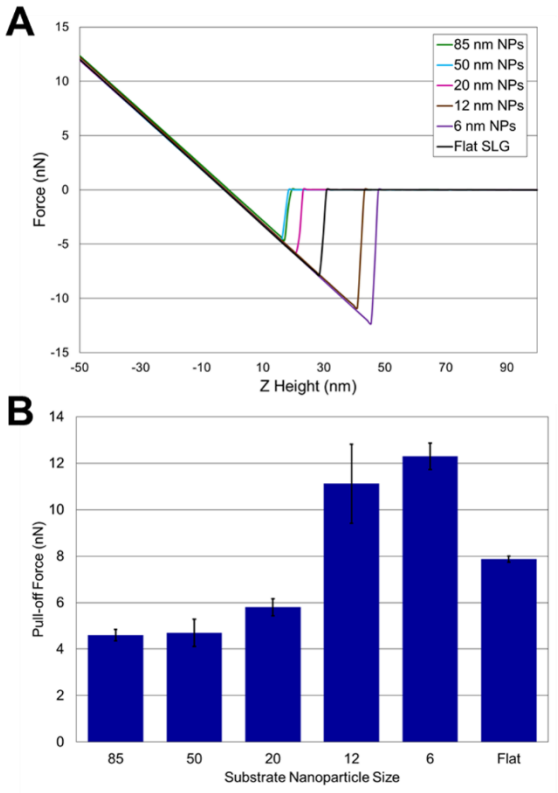

Figure 3.4. (A) Average of 10 force-distance retract curves and (B) plotted average pull-off force measurements from graphene on different rough substrates showing adhesion variation with changing roughness.

adhesion was found to generally decrease with increasing roughness with the lowest measured adhesion on the 85 nm and 50 nm samples, which have similar values, and the highest adhesion on the 6 nm sample. The variations in adhesion depend on a combination of varying surface roughness, environment such as humidity, and the surface chemistry of the tip and sample. Although graphene is intrinsically hydrophobic it has been shown to exhibit increased hydrophilic nature under ambient conditions due to surface adsorbents[137] allowing for the formation of a capillary at the tip-graphene interface. The capillary force depends on contact area which is also affected by the local

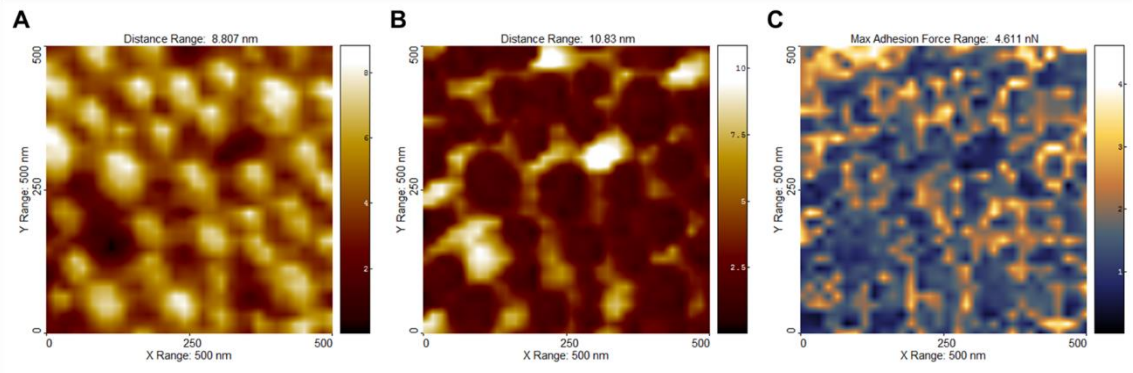

Figure 3.5. Deflection height images at ~20 nN (A) and -3 nN (B) extracted from a 32x32 grid array of force-distance curves on the 85 nm nanoparticle graphene sample. Adhesion map (C) calculated from the pull-off forces showing adhesion variation across the rough surface.

roughness of the surface.[138, 139] On the 85 nm and 50 nm samples the radius of curvature of the particles is larger, or nearly equivalent to that of the AFM tip (measured to be ~ 29 nm) creating a reduced contact radius which can decrease the measured pull-off force. As roughness decreases the particles also have reduced radii smaller than the radius of the tip and closer spacing together allowing for the tip to contact multiple asperities, affording nucleation of multiple capillaries which would nominally increase the adhesion force.

Although it is clear that the adhesion varies with changing roughness, the cause of the variations remains the same as a result of, in this case, humidity and the relative changes in contact area between the tip and the graphene covered particles. As noted above, since the graphene is not fully conformed when deposited on larger 85 nm and 50 nm nanoparticle samples, this provided a unique platform to spatially resolve changes in local adhesion through force-volume mapping. Here, small regions of 500 nm^2 or less

were imaged and then corresponding adhesion maps were calculated from the pull-off forces from a 32 x 32 grid array of force-distance curves. Figure 3.5 shows example deflection height images at imaging loads of ~20 nN and ~ -3 nN for the 85 nm sample and the corresponding adhesion map extracted from the force-volume data.

Due to the size of the nanoparticles and small regions measured, single particle features are readily resolved and local changes in adhesion as it varies across the suspended graphene film could be mapped out and correlated to the local topography. The higher load deflection height image in Figure 3.5A shows the graphene is compressed and conformal to the nanoparticles while the low load deflection height image in Figure 3.5B shows that graphene regions are suspended between the nanoparticles. The graphene is also observed to adhere to the tip as it pulls away from the surface and can be extended up to 8 nm above the surrounding particles.

In the adhesion map (Figure 3.5C) it is clear that there are variations in adhesion across the surface, including spikes in adhesion around the particles which can be seen as ring-like structures. The increase in adhesion at these locations corresponds to increased contact between the particle-graphene-tip interfaces, since along the edges of these asperities, more of the tip is contacted in these locations. Similar ring-like artifacts can be observed in the friction maps obtained when imaging in contact mode (see Supporting Information in Appendix B) due to bending of the cantilever as the tip encounters the sides of the nanoparticles during scanning and coupling of the normal and lateral signals in the photodectector. There are also small variations in the data when comparing suspended graphene regions between the nanoparticles and

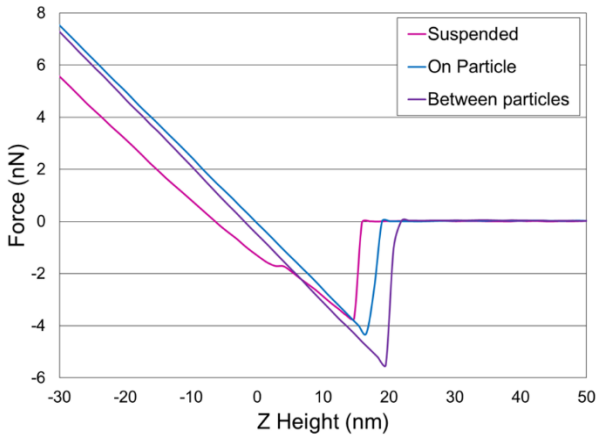

Figure 3.6. Example force-distance curves showing graphene adhesion variations depending on tip location on top of a single nanoparticle, on suspended regions of graphene, and between two adjacent nanoparticles.

graphene regions directly supported by the nanoparticles, which is not obvious from the adhesion map. These differences can be more easily observed by viewing individual local force-distance retract curves (Figure 3.6) taken by placing the AFM tip at different known locations on the graphene.

The suspended graphene retract curve shows a smaller deflection slope in the repulsive region and reduced adhesion in the pull-off region. This is in agreement with previous literature work on adhesion of suspended graphene.[140] In addition to these similarities, a small change in the slope is also observed in the retract curves of suspended graphene right before pull-off. This change of slope can be described as a point of instability where, as the tip decreases load, the tension created in the graphene is reduced and the tip transitions to lifting the graphene. Average adhesion for each location was found to be the lowest for the suspended graphene (3.7 ± 1.1 nN), highest when the tip was placed between two adjoining particles (5.5 ± 0.7 nN) and in between

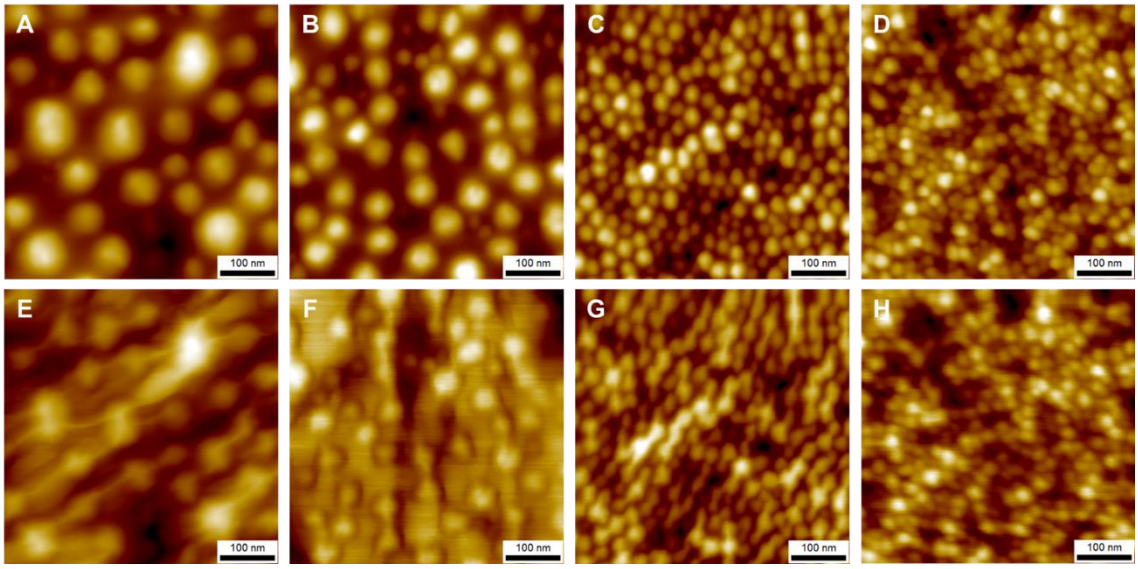

Figure 3.7. AFM contact mode topography images of graphene on (A, E) 85 nm nanoparticles (B, F) 50 nm nanoparticles (C, G) 20 nm nanoparticles (D, H) 12 nm nanoparticles under different tip loads. Images A-D were obtained with a tip load of 20 nN and images E-H were obtained with a tip load of -3 nN.

(4.3 ± 0.7 nN) when the tip was placed on top of a large nanoparticle. These adhesion variations can be attributed to changes in the contact between the tip and the graphene on the rough substrate. The tip has higher adhesion contacting the side of a nanoparticle while in a valley or contacting multiple nanoparticles simultaneously than when it is on top of a single nanoparticle. These variations in adhesion are expected to occur on the smaller nanoparticle films as well since large deviations are also observed on those samples as the tip contact changes across the sample. However, when the nanoparticles are smaller than the tip, the resolution of the force-distance grid cannot correlate the adhesion changes to topographical changes due to the low resolution.

From the force-volume data it was seen that graphene adhesion is a balance between the adhesion of the graphene to the substrate and to the tip since the graphene could only be lifted up on regions suspended above the substrate. Using contact mode imaging under similar tip loads of 20 nN and -3 nN, this effect is also observed as the tip is able to shear the graphene when a negative load is used, causing wrinkle formation on the 85 nm, 50 nm, and 20 nm samples (Figure 3.7). However, when the same negative imaging load was used to image the 12 nm, 6 nm, and flat graphene no wrinkles were observed due to the increased graphene conformity with the substrate and the associated increased adhesion to those substrates.

The wrinkles that are formed are small and depend on the presence of an attractive capillary force to hold the tip to the surface while imaging and are reversible since by imaging under an increased tip load the graphene is compressed and the wrinkles smoothed out. Thus, the behavior of the graphene is highly dynamic as function of applied load, and as such, the graphene can readily adhere and de-adhere from the substrate, when there is a rough surface.

With regards to the dynamic formation of wrinkles in the graphene, it was also found that by rinsing the dry samples with high purity water for even a few seconds and using nitrogen to dry excess water from the surface a more dramatic wrinkle effect could be created. After exposing the rough graphene samples to solvent, excess water can remain trapped under the graphene and decrease the interfacial adhesion between graphene and the substrate. Combined with the shearing motion of the tip, when the damp samples were imaged in contact mode the graphene was easily able to adhere to

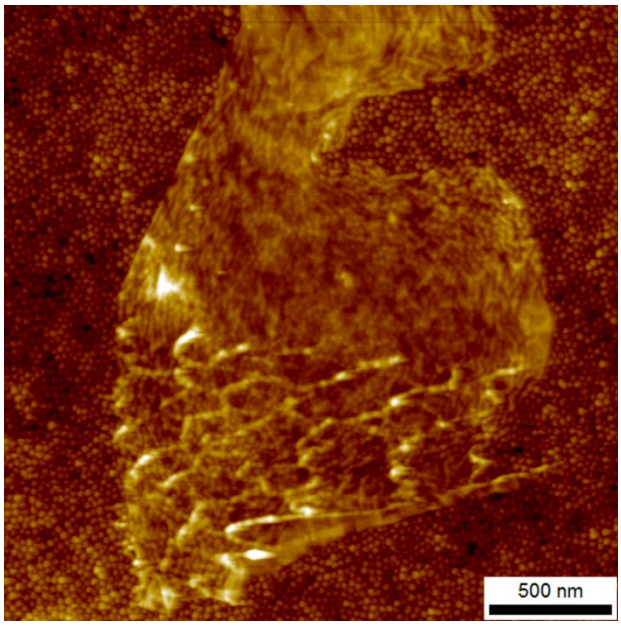

Figure 3.8. Tapping mode image of monolayer graphene on 20 nm nanoparticles imaged after the sample had been rinsed with high purity water and dried with nitrogen and first scanned in contact mode which caused large wrinkle formation in the graphene.

the tip and large wrinkles were created. As contact mode scanning was used to create the wrinkles they were only able to be visualized in tapping mode. An example of these contact mode induced wrinkles on a small graphene flake on 20 nm nanoparticles is shown in Figure 3.8. The wrinkle heights in this case are found to be up to 10 nm in height. These types of wrinkles on damp and rough graphene samples are easily reproduced but were not desirable as they altered the pristine structure of freshly exfoliated graphene. They are, however, a good example of the importance of environmental influence and sample preparation on the adhesion of rough graphene.

The dynamic behavior illustrated here is in good agreement with ability of graphene sheet under shear to be able to form nanoscrolls in the presence of diamond

nanoparticles in shearing contacts,[127] whereby the continuous adhering and de-adhering of the graphene from the substrate (which is a direct result of having both bound and suspended regions) affords a dynamic restructuring of the graphene sheets under sheer, which provides a mechanism for nanoscroll formation to occur.

3.4 Conclusion

Thin nanoparticle films with controlled thickness and roughness were successfully fabricated by tuning the nanoparticle size from 6 nm to 85 nm and used as substrates for investigating the influence of roughness on the adhesive properties of graphene. It was shown with AFM that the morphology of mechanically exfoliated graphene depends on the roughness of the substrate with changes between conformed states on substrates with low roughness to partially conformed states on substrates with large roughness. These changes in morphology were attributed to a balance between the flexible nature of graphene combined with the attractive interfacial van der Waals adhesion and elastic strain of the graphene lattice. The interfacial adhesion between graphene and the substrate increased with decreased roughness but at the cost of increased strain as measured by shifts in the 2D and G Raman peaks. Analysis of force-distance curves between a diamond-like-carbon AFM tip and graphene showed that adhesion decreased with increased roughness and depended on the contact area and capillary force, which increased on substrates with lower roughness due to multiple asperity contacts. Nanoparticle films composed of 50 nm and 85 nm nanoparticles provided a unique platform for force-volume mapping where adhesion variations on graphene were directly correlated to topographic features. By controlling the tip force

between negative and applied loads and the amount of water at the interface, the dynamic nature of graphene was also explored revealing a controllable adhering and de-adhering from the substrate.

CHAPTER IV

MODULATING THE TRIBOLOGICAL PROPERTIES OF GRAPHENE BY TUNING SUBSTRATE-GRAPHENE INTERACTIONS USING SELF-ASSEMBLED MONOLAYERS

4.1 Introduction

Graphene is a two-dimensional carbon nanomaterial and one of the thinnest solid materials first experimentally fabricated over a decade ago in 2004.[6] It is well-known for its unique properties such as high out-of-plane flexibility, large in-plane elastic modulus (measured up to 1TPa),[12] intrinsic hydrophobicity, chemical inertness and a low coefficient of friction.[52] These properties make graphene an ideal candidate for many technological applications including micro-/nano-electromechanical systems (MEMS/NEMS) devices where control over friction and adhesion is critical for device performance and operational lifetime. Utilization of graphene in real devices however is still largely limited, due to graphene's high surface-to-volume ratio making it susceptible to surface forces which dictate the interface interactions, and the need of approaches for delivery of graphene to surfaces on the large scale.

The interfacial interactions noted above can have undesirable effects on the properties of graphene and are impacted by a number of sources including the substrate material, morphology, surface chemistry, environment, and fabrication method. For example, exposure to ambient conditions has been shown to increase surface adsorbents

and contaminants which can decrease the hydrophobicity of graphene.[137] The substrate has also been found to have a large influence on graphene's properties with variations in measured friction reported from studies on suspended graphene[140] and graphene mechanically exfoliated on silica and mica.[33] These variations in friction originate from differences in atomic-scale roughness which decreases the adhesion between graphene and the substrate. On surfaces with nanoscale roughness, this effect is enhanced where graphene conformity and adhesion decreased with increased roughness, limiting the points of contact to the substrate.

Although the effect of surface roughness may add a physical limitation to the optimal adhesion and friction performance of graphene, the properties may be improved and more controllable by changing the surface chemistry. Self-assembled monolayers (SAMs) are ideally suited for controlling surface chemistry by chemical functionalization of silica substrates and tuning the functional groups of the attached monolayers. Although the surface chemistry and tribological properties of a wide variety of SAMs have been studied for decades,[141] there are only few studies on the tribological properties of SAM/graphene composites.[109, 129] Here, in order to improve the fundamental understanding of the tribological properties of graphene/SAM composites, mixed SAM surfaces were prepared on thermally oxidized silicon wafers to study the *in situ* changes of surface interactions between the SAMs and graphene. In particular we have compared the interactions of graphene with octadecyltrichlorosilane (OTS) and perfluorophenylazide-silane (PFPA-silane) monolayers which offer contrasting interactions, as OTS is methyl-terminated molecule yielding only

hydrophobic van der Waals interactions with graphene, while PFPA-silane, upon heating, can react with graphene to yield a covalent linkage to the graphene. Theses SAMs have been prepared with varying structure, and as mixed monolayers on oxidized Si(100) wafers to explore the individual and concerted effects of these molecules on the resulting tribological properties of the graphene-SAM composites.

4.2 Experimental Methods

4.2.1 Sample Preparation

To create mixed SAM surfaces, thermally oxidized Si(100) wafers (prepared by heating the Si wafer in a kiln at 1050 ºC for 80-90 min and then cleaned as described below) were partially functionalized with octadecyltrichlorosilane (OTS) to create island structures and backfilled with a perfluorophenylazide-silane (PFPA-silane) molecule (N-(3-Trimethoxysilylpropyl)-4-azido-2,3,5,6-tetrafluorobenzamide from Toronto Research Chemicals Inc). The oxidized silicon wafers were first cleaned and hydroxylated with a 4:1:1 (v/v/v) solution of high purity H_2O (18.2 MΩ·cm, Barnstead), concentrated NH_4OH, and H_2O_2 (30%) for ~15 min at 85ºC (*Caution: Piranha solution is highly corrosive and reacts violently with organic matter*). The samples were rinsed with nanopure water, ethanol and dried with streaming nitrogen. Island structures were created by preparing a ~1 mM OTS (Gelest)/hexanes solution under nitrogen environment and the solution was aged 5-10 min before the clean wafers were dipped in the solution for 1-10 sec. The wafers were then immediately rinsed with hexanes, toluene and dried with nitrogen. For mixed SAM surfaces the OTS island samples were soaked in a ~1mM PFPA-silane/toluene solution for ~20 hrs while stored away from

light. The samples were again rinsed with toluene and dried with nitrogen before characterization with FTIR Spectroscopy.

To create graphene/SAM composites water soluble tape (3M) was first used to exfoliate HOPG (K-Tek Nanotechnology) and transfer the flakes to the sample substrates. The tape was then dissolved in a water bath (85º C) and rinsed with water from a wash bottle to slowly remove the bulk of the tape residue and some graphite. Tape was used a second time to cleave part of the graphite from the dried surface resulting in new exposed regions of graphene flakes. The samples were stored in a desiccator until further characterization.

4.2.2 Fourier Transform Infrared (FTIR) Spectroscopy

Infrared spectra of chemically functionalized substrates were measured with a Thermo Nicolet 6700 FTIR equipped with a liquid nitrogen-cooled MCT (HgCdTe) detector and a Harrick Scientific horizontal reflection Ge-attenuated total reflection accessory (VariGATR, incidence angle 65º). A semispherical Ge crystal was used as the optical element. Spectra were collected at a resolution of 1 cm^{-1} for the backgrounds (64 scans) and functionalized samples (512 scans).

4.2.3 Raman Microspectroscopy

A confocal Raman microscope (WITec Alpha 300R, Germany) was used for visualizing regions with graphene flakes utilizing the optical contrast provided by the controlled thickness of the top silica layer of the substrate. The samples were characterized with Raman spectroscopy under ambient conditions (20-25 ºC). The microscope was equipped with an Acton triple grating spectrometer interfaced with an

Andor Peltier cooled (-65 ºC) CCD detector and a 488 nm Ar ion laser with a laser spot size of *ca.* 300 nm focused with a Nikon high numerical aperture objective (100x, 0.9 NA). The spectral resolution used was ~ 3 cm^{-1}. The laser power for all measurements was maintained below 1.5 mW.

4.2.4 Atomic Force Microscopy (AFM)

Samples were imaged by AFM (Agilent 5500) with silicon tips (Mikromasch CSC37 for contact mode) under ambient conditions (40% RH - 50% RH and 20 ºC -25 ºC). The contact mode tips had force constants ranging from 0.1 N/m – 0.8 N/m, depending on lever, and the spring constants were independently determined for each with the Sader method.[94] Tip radii were measured by scanning standard substrates with known geometry and calculating the radii from the blind tip reconstruction feature using Scanning Probe Image Processing (SPIP) Software (Image Metrology, Denmark). All topography images, friction maps, height profiles, and adhesion calculations were also processed with SPIP.

4.3 Results and Discussion

4.3.1 OTS Islands on Oxidized Si(100)

In a previous study we have shown that silica nanoparticles and thermally oxidized silicon wafers may be chemically functionalized with OTS and interfaced with graphene through mechanical exfoliation.[129] It was found that the hydrophobicity of OTS coated surfaces increases the affinity of graphene towards the substrate and can minimize chemical doping from charge groups on the underlying silica. However, this improved adhesion was not enough to alter the surface morphology or frictional

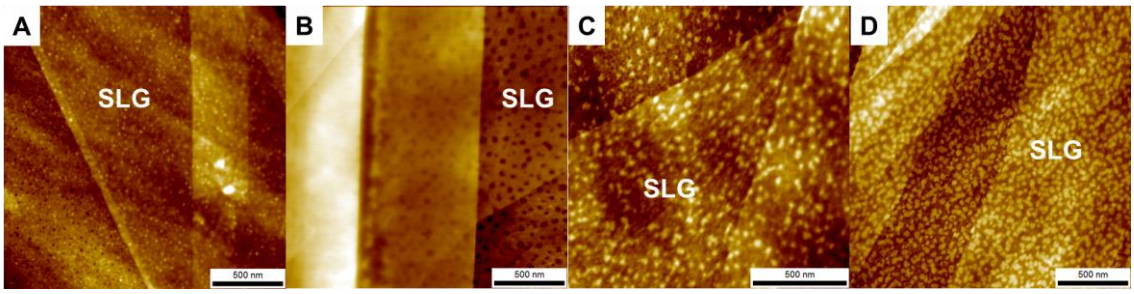

Figure 4.1. AFM topography images of monolayer and mult-layer graphene flakes on OTS films with different structures including small pits (A), large pits (B), and nano-islands (C) & (D).

properties of graphene but rather appeared to increase the friction in some cases. Although the OTS had an overall neutral effect on the graphene, it was also observed that different surface structures of the SAM may be fabricated with some examples of graphene on OTS films with pores and islands shown in Figure 4.1. The ability to pattern OTS surface structures by simply controlling the reaction conditions makes it an ideal molecule for studying *in-situ* changes in friction and adhesion on mixed monolayer SAMs.

The reaction of OTS on silicon surfaces[142] has been well-studied and is known to depend on various factors that affect film formation including concentration, reaction times, solvent, water content, temperature and roughness.[143-146] Due to the extreme sensitivity of OTS deposition, exact sample-to-sample reproducibility is often difficult and it was necessary to test similar conditions found in the literature in order to achieve the desired island structures for creating mixed SAM surfaces. AFM was used to characterize the OTS films deposited under various conditions and topography images of typical island structures fabricated are shown in Figure 4.2.

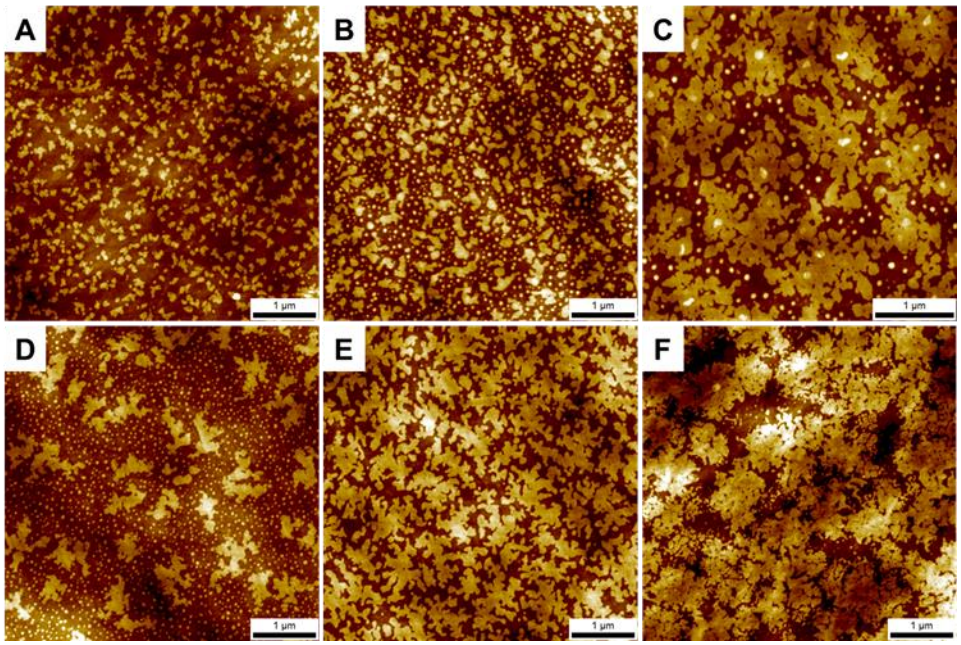

Figure 4.2. AFM topography image of controlled formation of OTS islands under different reaction conditions. (A) Solution age 10 min, 10 sec deposition (B) Solution age 10 min, 5sec deposition (C) Solution age 60 min, 1 sec deposition (D) Solution age 5 min, 1 sec deposition (E) Solution age 5 min, 5 sec deposition (F) Solution age 10 min, 1 sec deposition. (D-F) were deposited with increased humidity (RH ~ 55%).

These island structures were formed by using ~ 1 mM OTS in hexanes solution. Higher concentrations were found to react more quickly preventing capture of the intermediate island phase during film formation. Using toluene as the solvent only showed small micelle aggregates on the surface and no island structures. The effect of sonication was found to slow down the reaction and break up aggregates in solution with small, closely spaced nanometer sized islands (< 50 nm) observed in Figure 4.1C and Figure 4.1D. However, sonication was found to be important for full film formation as it aids in removing micelle aggregates from the surface. This explains why small circular pits were formed as seen in Figure 4.1A and Figure 4.1B where the OTS film formed around

the small micelles, which were later removed with sonication during cleaning. For the purpose of this study, larger islands with less density were desired for measurements of the mixed SAM surface so instead of sonication, which breaks up island aggregates, the OTS solution was aged without agitation to allow for larger island aggregates to form. The effect of aging combined with short deposition times up to 10 secs consistently produced island structures with larger diameters shown in Figure 4.2A and Figure 4.2B. Aging the solution longer (up to an hour) allowed for continued island growth (>500 nm), however the reproducibility of these islands was limited by the control of water content in solution and relative humidity, which can cause polymerization of OTS.[147] Samples with OTS deposited under more humid conditions therefore required shorter deposition and solution aging times to in order to form islands as shown in Figure 4.2D-F.

To create mixed SAM surfaces, samples with deposited OTS islands shown in Figure 4.2A and Figure 4.2B were backfilled by soaking in a solution with perfluorophenylazide (PFPA)-silane molecules overnight. PFPA was chosen for this study and is of interest due to its versatility as a coupling agent to covalently functionalize materials such as polymers and bind to a variety of substrates including silicon wafers, gold films, and metal oxides by simply changing the linker between silanes, thiols, and phosphates.[148] It is of particular interest in graphene research for its efficient covalent functionalization which enables tuning of graphene's properties such as carrier mobility enhancement, solubility improvement and immobilization of

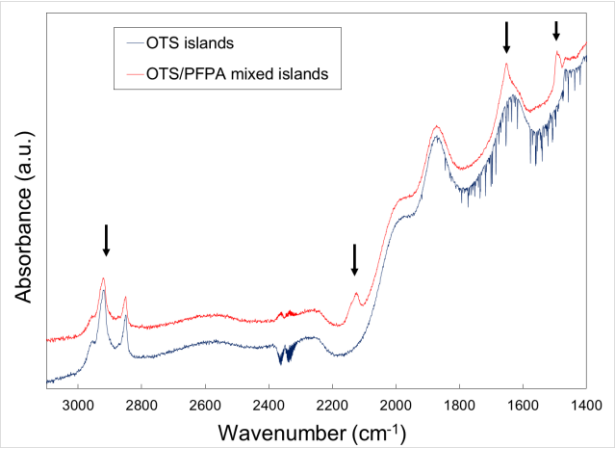

Figure 4.3. ATR-FTIR absorbance spectra of OTS islands on thermally oxidized silicon before and after addition of PFPA-silane.

graphene on solid substrates.[149] The immobilization of graphene on silicon wafers has been shown to be quite robust, even under sonication, making it an ideal candidate for binding graphene to rough surfaces where weak adhesion is a critical issue for utilization of graphene as a solid lubricant and protective coating.

Figure 4.3 shows ATR-FTIR absorption spectra of the OTS islands before and after deposition of the PFPA-silane. The characteristic methylene stretching vibrations for OTS are observed at 2919 cm^{-1} for the asymmetric CH_2 and 2849 cm^{-1} for the symmetric CH_2 peaks. After deposition of PFPA-silane additional peaks[150] are seen at 2124 cm^{-1} (asymmetric stretching of the azide), 1651 cm^{-1} (amide stretching), and 1492 cm^{-1} (C=C stretching from the phenyl ring). It was also observed that exposing the functionalized silicon wafers to ambient conditions resulted in increased adsorption of water on the surface which could be seen in the FTIR absorption spectra due to the hydrophilic nature of the SiO_2 and PFPA sample regions. Using AFM to measure the

average OTS island heights before and after addition of PFPA showed a decrease from 2.1 ± 0.3 nm to 1.6 ± 0.4 nm also indicative of mixed SAM functionalization.

4.3.2 Fabrication and Characterization of Graphene/SAM Composites

Graphene/SAM composites were prepared through mechanical exfoliation using water-soluble tape, which we previously found increases the yield of graphene flakes on silica surfaces over the typical scotch-tape method.[6] Regions containing graphene flakes were located optically for further characterization by Raman microspectroscopy and AFM. Figure 4.4A shows an example optical micrograph of graphene and multi-layer graphene flakes on a thermally oxidized silicon wafer previously functionalized with OTS and PFPA-silane. The AFM topography image in Figure 4.4B corresponds to the region marked with a red box in the optical micrograph showing single and multi-layer graphene flakes are easily able to adopt to the underlying OTS island structures. Similar to previous observations on rough graphene surfaces, the conformity decreases with increased thickness of the graphene layers with less of the island features visible on the thicker flakes.

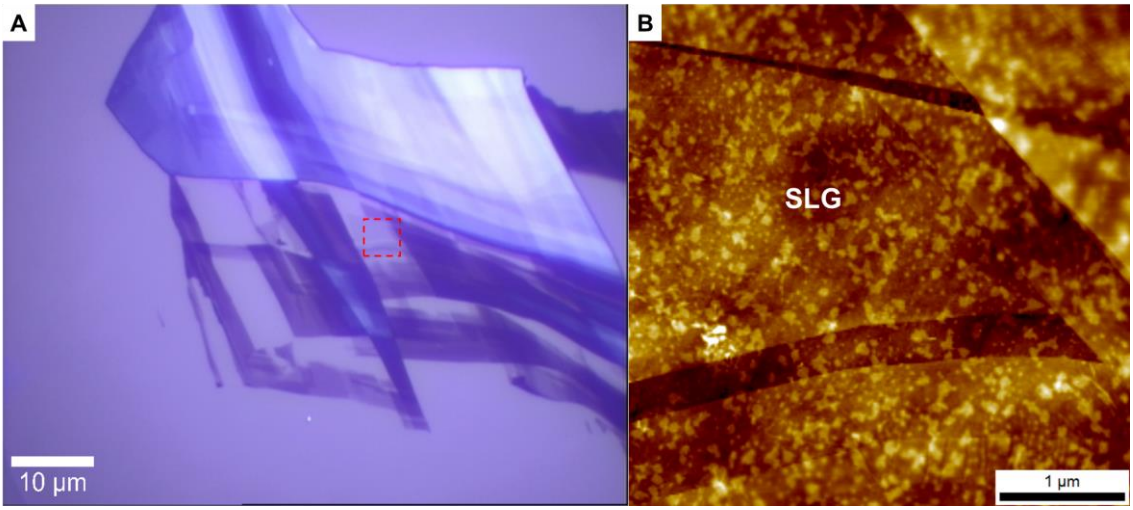

Figure 4.4. Optical micrograph (A) of exfoliated graphene flakes on a thermally oxidized silicon wafer functionalized with mixed SAMs of OTS islands and PFPA. The corresponding AFM topography image (B) of monolayer and multi-layer graphene taken from the region labeled with the red box in A.

To achieve covalent functionalization of graphene with the PFPA molecule, the sample was heated to 140 ^{o}C for 40 min.[151] Upon thermal activation, the azido group is converted to a highly reactive singlet phenylnitrene which can then react with graphene through C=C addition.[151] Single point Raman spectra (Figure 4.5) were acquired before and after heat treatment showing the characteristic G and 2D Raman modes of pristine, single-layer graphene. The spectra were fit with a Lorentzian to obtain peak positions and widths. The G mode was located at 1587 cm^{-1} with a FWHM of 15 cm^{-1} before heating and 1588 cm^{-1} with a FWHM of 16 cm^{-1} after heating. The 2D mode was located at 2696 cm^{-1} with a FWHM of 27 cm^{-1} before heating and shifted slightly to 2697 cm^{-1} with a FWHM of 29 cm^{-1} after heating. The largest change in the spectra was

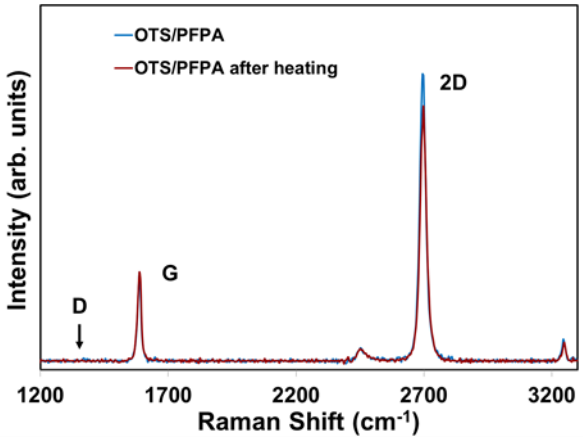

Figure 4.5. Raman spectra of monolayer graphene before and after heat treatment of the sample showing the characteristic G and 2D peaks. *Notably, the D peak is missing after heating, indicating little disruption of the graphene sp2 network.*

a decrease in the intensity ratio between the 2D and G peaks decreasing from 3.4 to 2.7 after heating. It is interesting to note that upon covalent binding of the graphene with PFPA there was no introduction of measurable defects in the graphene as evidenced by the lack of a D peak at 1350 cm^{-1}. This lack of a D peak is consistent with previous literature work[151] although it is unclear why there is little change in the Raman spectra after the graphene is functionalized with PFPA. This could either be indicative of little reaction between the PFPA and graphene, or little disruption of the sp^2 covalent network.

AFM was also used to characterize the graphene/SAM composites before and after heating, where much more noticeable changes in the samples were observed. From the topographic images in Figure 4.6A and Figure 4.6C the graphene was seen to become rougher after functionalization and was more compressed to the substrate. The friction map in Figure 4.6B shows that the PFPA functionalized silica has the highest friction with lower friction on the OTS islands and graphene flakes (darker regions).

The graphene region of the friction map shows divided regions of high and low friction most likely due to the presence of trapped water between the graphene and the mixed SAMs. Since graphene is impermeable, it well-known to be able to trap gases and liquids[152] and the water in this sample likely originated from water adsorption on the surface as the sample was prepared under ambient conditions or from water intercalation during removal of the water-soluble tape.

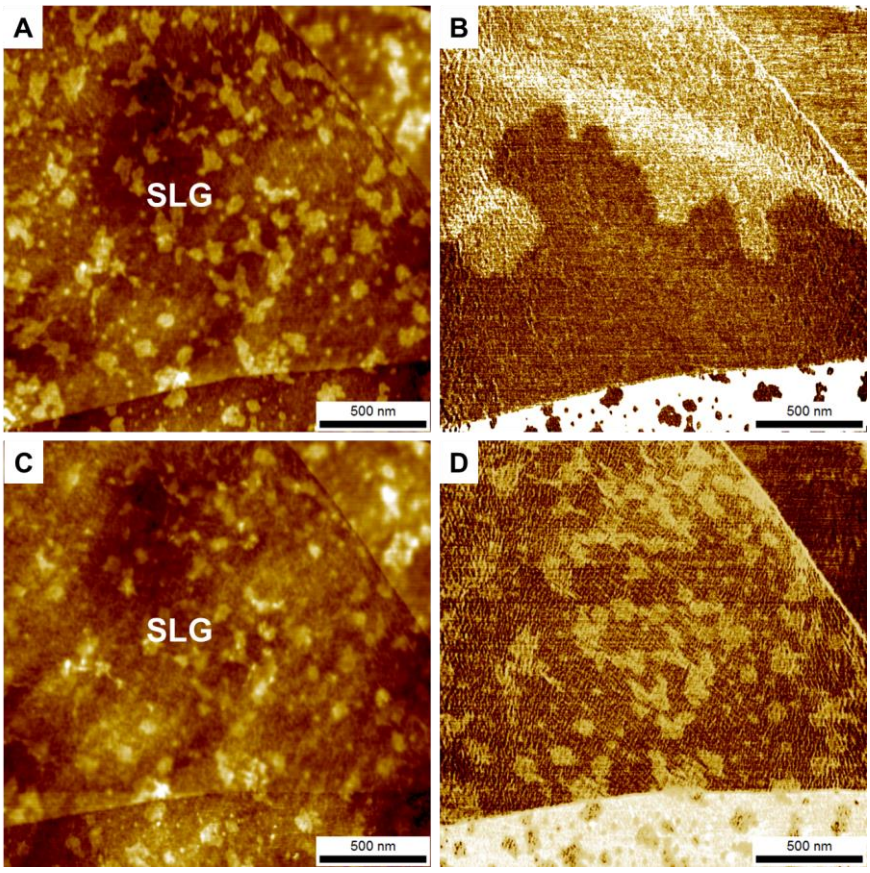

Figure 4.6. Contact mode AFM topographic and friction images of graphene/mixed SAM composites before (A and B) and after (C and D) heating.

After heating the sample, the friction map in Figure 4.6D showed that most of the water was removed and distinct changes in friction can be found on the graphene where the PFPA functionalized graphene has lower friction than the graphene/OTS islands. This indicates that the coupling of PFPA and graphene improves the friction likely due to increased stiffness and decreased puckering of the graphene from the covalent immobilization. Compared to the substrate and multi-layer regions the graphene has lower friction than the substrate but the lowest friction was still seen on the multi-layer graphene. When a graphene/OTS island sample without PFPA was heated under similar conditions there were no significant changes in the topography and friction as was observed on the mixed SAM sample, although the presence of trapped water was observed and similarly reduced after heating (Supporting Information in Appendix C).

Force-distance spectroscopy was used to measure the changes in pull-off force on different sample regions before and after thermal activation of the PFPA with the results shown in Table 4.1. Before heating the sample there was little difference in adhesion on the SAM or graphene which is likely due to any adsorbed contaminates and trapped water at the surface. After heating, the highest adhesion was measured on the PFPA functionalized substrate and the lowest on the OTS islands. Since the adhesion measurements were taken under ambient conditions with an oxidized silicon AFM tip, it is expected that higher adhesion would be found on the more hydrophilic PFPA molecules than the hydrophobic OTS islands. These adhesion results however require further review as the nature of the tip-graphene-substrate contact can be widely altered through changes in molecular organization of the SAM upon heating, which can modify

the tip-sample contact area having a marked impact on the resulting adhesion. Further studies to examine these changes in detail are underway.

Sample Region	Before Heating Pull-off (nN)	After Heating Pull-off (nN)
Graphene/OTS	2.8 ± 0.05	4.7 ± 0.5
Graphene/PFPA	3.0 ± 0.2	4.1 ± 0.4
OTS	3.0 ± 0.2	2.5 ± 0.05
PFPA	3.0 ± 0.2	5.3 ± 0.4

Table 4.1. Pull-off force adhesion results from force-distance spectroscopy measurements on different substrate and graphene regions. Each value was obtained from an average of 10 measurements on each sample region.

4.4 Conclusion

In this study, the tribological properties of graphene/SAM composites were explored by Atomic Force Microscopy and Raman microspectroscopy. Thermally oxidized silicon wafers were functionalized and patterned with islands of octadecyltrichlorosilane by controlling the deposition conditions. Further functionalization was achieved by addition of a perfluorophenylazide-silane molecule yielding substrates with mixed self-assembled monolayers. Graphene/SAM composites were fabricated by mechanical exfoliation and the topography, friction and adhesion of these composites was characterized before and after thermal activation of the PFPA. It was shown that the PFPA can covalently functionalize graphene with lower friction

observed on the bonded graphene as compared to the friction on the OTS/graphene regions. The presence of trapped water between the graphene and substrate as well as between multi-layer graphene flakes was observed and shown to be reduced after heat treatment of the sample. This trapped water was also observed to influence the tribological measurements and should be accounted for in future experiments. These preliminary results suggest that PFPA-silane is an ideal candidate for future studies to covalently bind graphene on substrates with nanoscale roughness where weak substrate adhesion is a critical factor for friction modification.

CHAPTER V

SUMMARY AND OUTLOOK

5.1 Summary

The influence of surface roughness on the tribological properties of graphene was experimentally investigated using Atomic Force Microscopy. For the purpose of understanding the interactions of pristine graphene with rough surfaces, a protocol was first developed and used throughout this research to mechanically exfoliate graphene from highly oriented pyrolytic graphite (HOPG) onto rough surfaces through the use of water-soluble tape. This method provided the advantage of increasing the yield of graphene flakes as well as transferring large millimeter sized graphite to the substrate, which was used as a reference for optically locating graphene and for comparative tribological measurements.

In the first study, silica substrates with ~ 10 nm RMS roughness were used to mimic the roughness often found in real microelectromechanical systems (/MEMS) devices, as well as many real machined interfaces, to understand the general morphology and substrate dependent properties of deposited graphene. From AFM topography images it was found that, unlike the atomically flat surfaces that have been typically researched to this point, graphene can only partially conform to the rough structure resulting in decreased interaction with the substrate and a weakly bound state. This partial conformity was seen to further decrease on thicker graphene layers due to increased bending stiffness. The unique morphology of graphene on substrates with

nanoscale roughness resulted from competing factors of interfacial van der Waals forces, bending stiffness of the graphene layers, and lattice strain imposed by the sharp asperity peaks.

The mechanical properties of graphene were studied by controlling the applied tip load during imaging, and graphene was observed to readily deform under loads up 125 nN but reversibly relaxed when the load was decreased (back to *ca.* 5 nN) due to the elastic nature of graphene. The frictional properties were found to have an unexpected dependence on the contact area of the AFM tip where there was little difference in friction between graphene and thicker layers when a sharp tip was used but an increase in friction was measured on graphene when a tip much larger than the size of the substrate asperities was used due to increased adhesion and contact with the graphene. The influence of substrate chemistry on these properties was studied by functionalizing the silica substrates with octadecyltrichlorosilane (OTS) resulting in increased affinity of graphene to the substrate. The graphene/OTS composites showed similar morphology and lattice strain as compared to graphene on unfunctionalized substrates. Additionally, the OTS was seen to also act as a buffer layer between the graphene and silica surface to reduce chemical doping effects.

From this research, an improved fundamental understanding of the substrate dependent tribological properties of graphene was achieved. The morphology of graphene was found to be dictated by the substrate roughness and the resulting weakly bound state suggests graphene would easily delaminate from the surface under strong shearing forces, which is largely undesirable as a protective coating and a key limitation

of using graphene as a solid lubricant coating. The effect of lattice strain could potentially lead to nucleation of defects at points of high pressure contacts and weakening of the structure over time although the onset of wear may be slowed by the ability of graphene to elastically deform under mechanical loading.

By changing the size of the nanoparticles used to control substrate roughness, films with controlled nanoscale roughness were fabricated for investigating the influence of roughness on the adhesion of graphene to such substrates. It was found that the conformity of graphene increased on substrates with small roughness while it decreased on surfaces with large roughness composed of 50 nm and 85 nm nanoparticles. This change in conformity corresponded to changes in interfacial adhesion where substrates with less contact with graphene exhibited large suspended regions, had the lowest adhesion. Similar trends were also observed in peak shifts in the Raman spectra indicating that substrates with low roughness and increased graphene conformity also had the most induced strain due to increased out-of-plane deformation of the lattice, as the graphene tried to accommodate the spatial changes in substrate morphology and maximize adhesion to the substrate. Force-distance spectroscopy was used to measure the adhesion variations between the tip and graphene with different rough substrates and showed adhesion increased with increased number of asperity contacts as observed on smaller nanoparticle substrates. Force-volume mapping of small regions on the 50 nm and 85 nm samples allowed for adhesion variations between the tip and graphene to be spatially correlated with topographic features. Adhesion increased when the tip was placed between nanoparticles while it decreased on top of the nanoparticles and on

suspended regions of graphene. Topographic images of graphene under negative and applied loads revealed that graphene can change morphology and continuously adhere and de-adhere between the tip and particles. The effect of substrate bound water was also shown to decrease the adhesion between graphene and the substrate resulting in large wrinkle structures which could be readily introduced during the shearing motion of the tip across the sample.

Through controlled substrate roughness, it was shown that through the interplay of morphology, graphene lattice strain, and local adhesive interactions of graphene to the substrate, that the tribological properties of graphene could be tuned and largely regulated but was still limited by the substrate geometry. An alternative method for controlling the friction and adhesion properties of graphene was demonstrated by functionalizing the surface with a perfluorophenylazide-silane (PFPA-silane) molecule, which could be used as a coupling agent to covalently bond to and immobilize graphene. The changes in friction and adhesion were measured on a thermally oxidized silicon wafers patterned with OTS islands and backfilled with PFPA-silane. It was observed that the PFPA was able to bind the graphene to the surface without introducing a significant density of atomic scale defects into the graphene (i.e. limited loss of sp^2 character) and the friction of graphene was lower on the PFPA than the OTS islands. These preliminary results suggest that covalent immobilization of graphene with PFPA would be ideally suited for substrates with nanoscale roughness where weak substrate adhesion is a critical factor. In addition to these observations, it was also found that the presence of water trapped under the graphene and between graphene layers can obscure

the measurements of friction and adhesion as observed on graphene/OTS composites and should be considered in future experiments.

5.2 Outlook

The results of this research has provided a foundation for understanding and controlling the tribological properties of graphene on rough silica substrates. Future work may expand these tribological studies to include experiments designed to further understand nanoscale wear of graphene as well as the energy dissipation pathways on graphene/SAM composites. The silica nanoparticles used in this research could also be replaced with metal nanoparticles for understanding the tribological properties of graphene under metal contacts. Since it is known that strain alters the electronic properties of graphene, the use of a conductive substrate would also aid in studying the effect of tuning the strain by roughness and controlling wrinkle formation by tuning the substrate adhesion on these properties. These results also point to factors which can be readily controlled that can directly influence the inherent electronic properties of graphene, as well as ways in which local bond strain can be exploited to control local chemical functionalization of graphene. In addition, the research here may also be expanded to include studies on other two-dimensional nanomaterials such as molybdenum disulfide and hexagonal boron nitride which are similar in structure to graphene but have very different electronic properties.

REFERENCES

1. Spalvins, T. *Thin Solid Films* **1982,** 96, (1), 17-24.

2. Dienwiebel, M.; Verhoeven, G. S.; Pradeep, N.; Frenken, J. W. M.; Heimberg, J. A., *et al. Physical Review Letters* **2004,** 92, (12), 126101.

3. Bull, S. J. *Diamond and Related Materials* **1995,** 4, (5–6), 827-836.

4. Spanu, L.; Sorella, S.; Galli, G. *Physical Review Letters* **2009,** 103, (19), 196401.

5. Busch, C., Solid Lubrication. In *Lubricants and Lubrication*, Wiley-VCH Verlag GmbH & Co. KGaA: 2007; pp 694-714.

6. Novoselov, K. S.; Geim, A. K.; Morozov, S. V.; Jiang, D.; Zhang, Y., *et al. Science* **2004,** 306, (5696), 666-669.

7. Du, X.; Skachko, I.; Barker, A.; Andrei, E. Y. *Nature Nanotechnology* **2008,** 3, (8), 491-495.

8. Balandin, A. A.; Ghosh, S.; Bao, W.; Calizo, I.; Teweldebrhan, D., *et al. Nano Letters* **2008,** 8, (3), 902-907.

9. Balandin, A. A. *Nature Materials* **2011,** 10, (8), 569-581.

10. Renteria, J.; Nika, D.; Balandin, A. *Applied Sciences* **2014,** 4, (4), 525-547.

11. Yan, Z.; Nika, D. L.; Balandin, A. A. *IET Circuits, Devices & Systems* **2015,** 9, (1), 4-12.

12. Lee, C.; Wei, X.; Kysar, J. W.; Hone, J. *Science* **2008,** 321, (5887), 385-388.

13. Kim, K.-S.; Lee, H.-J.; Lee, C.; Lee, S.-K.; Jang, H., *et al. ACS Nano* **2011,** 5, (6), 5107-5114.

14. Wählisch, F.; Hoth, J.; Held, C.; Seyller, T.; Bennewitz, R. *Wear* **2013,** 300, (1–2), 78-81.

15. Kitt, A. L.; Qi, Z.; Rémi, S.; Park, H. S.; Swan, A. K., *et al. Nano Letters* **2013,** 13, (6), 2605-2610.

16. Stankovich, S.; Dikin, D. A.; Dommett, G. H. B.; Kohlhaas, K. M.; Zimney, E. J., *et al. Nature* **2006,** 442, (7100), 282-286.

17. Chen, Z.; Berciaud, S.; Nuckolls, C.; Heinz, T. F.; Brus, L. E. *ACS Nano* **2010,** 4, (5), 2964-2968.

18. Stoller, M. D.; Park, S.; Zhu, Y.; An, J.; Ruoff, R. S. *Nano Letters* **2008,** 8, (10), 3498-3502.

19. Xia, F.; Farmer, D. B.; Lin, Y.-m.; Avouris, P. *Nano Letters* **2010,** 10, (2), 715-718.

20. Bunch, J. S.; van der Zande, A. M.; Verbridge, S. S.; Frank, I. W.; Tanenbaum, D. M., *et al. Science* **2007,** 315, (5811), 490-493.

21. Li, Q.; Lee, C.; Carpick, R. W.; Hone, J. *physica status solidi (b)* **2010,** 247, (11-12), 2909-2914.

22. Filleter, T.; McChesney, J. L.; Bostwick, A.; Rotenberg, E.; Emtsev, K. V., *et al. Physical Review Letters* **2009,** 102, (8), 086102.

23. Ma, T.-B.; Wang, L.-F.; Hu, Y.-Z.; Li, X.; Wang, H. *Scientific Reports* **2014,** 4, 3662.

24. Seol, J. H.; Jo, I.; Moore, A. L.; Lindsay, L.; Aitken, Z. H., *et al. Science* **2010,** 328, (5975), 213-216.

25. Cai, W.; Moore, A. L.; Zhu, Y.; Li, X.; Chen, S., *et al. Nano Letters* **2010,** 10, (5), 1645-1651.

26. Lee, J.-K.; Yamazaki, S.; Yun, H.; Park, J.; Kennedy, G. P., *et al. Nano Letters* **2013,** 13, (8), 3494-3500.

27. Kase, T.; Ogino, T. *Journal of Physical Chemistry C* **2013,** 117, (31), 15991-15995.

28. Wu, Q.; Wu, Y.; Hao, Y.; Geng, J.; Charlton, M., *et al. Chemical Communications* **2013,** 49, (7), 677-679.

29. Zhu, W.; Low, T.; Perebeinos, V.; Bol, A. A.; Zhu, Y., *et al. Nano Letters* **2012,** 12, (7), 3431-3436.

30. Goncher, S. J.; Zhao, L.; Pasupathy, A. N.; Flynn, G. W. *Nano Letters* **2013,** 13, (4), 1386-1392.

31. Berciaud, S. p.; Ryu, S.; Brus, L. E.; Heinz, T. F. *Nano Letters* **2008,** 9, (1), 346-352.

32. Cho, D.-H.; Wang, L.; Kim, J.-S.; Lee, G.-H.; Kim, E. S., *et al. Nanoscale* **2013,** 5, (7), 3063-3069.

33. Lee, C.; Li, Q.; Kalb, W.; Liu, X.-Z.; Berger, H., *et al. Science* **2010,** 328, (5974), 76-80.

34. Yalin, D. *Journal of Physics D: Applied Physics* **2014,** 47, (5), 055305.

35. Ye, Z.; Tang, C.; Dong, Y.; Martini, A. *Journal of Applied Physics* **2012,** 112, (11), 116102-3.

36. Ye, Z.; Otero-de-la-Roza, A.; Johnson, E. R.; Martini, A. *Applied Physics Letters* **2013,** 103, (8), 081601.

37. Wang, L.-F.; Ma, T.-B.; Hu, Y.-Z.; Wang, H.; Shao, T.-M. *Journal of Physical Chemistry C* **2013,** 117, (24), 12520-12525.

38. Leven, I.; Azuri, I.; Kronik, L.; Hod, O. *Journal of Chemical Physics* **2014,** 140, (10), 104106.

39. Reguzzoni, M.; Fasolino, A.; Molinari, E.; Righi, M. C. *Physical Review B: Condensed Matter* **2012,** 86, (24), 245434.

40. Liang, T.; Sawyer, W. G.; Perry, S. S.; Sinnott, S. B.; Phillpot, S. R. *Physical Review B: Condensed Matter* **2008,** 77, (10), 104105.

41. Levita, G.; Cavaleiro, A.; Molinari, E.; Polcar, T.; Righi, M. C. *Journal of Physical Chemistry C* **2014,** 118, (25), 13809-13816.

42. Xiaoyang, Z.; Linyang, L.; Mingwen, Z. *Journal of Physics: Condensed Matter* **2014,** 26, (9), 095002.

43. Smith, G.; Modine, N.; Waghmare, U.; Kaxiras, E. *Journal of Computer-Aided Materials Design* **1998,** 5, (1), 61-71.

44. Liang, T.; Sawyer, W. G.; Perry, S. S.; Sinnott, S. B.; Phillpot, S. R. *Physical Review B* **2008,** 77, (10), 104105.

45. Kwon, S.; Ko, J.-H.; Jeon, K.-J.; Kim, Y.-H.; Park, J. Y. *Nano Letters* **2012,** 12, (12), 6043-6048.

46. Yalin, D.; Wu, X.; Ashlie, M. *Nanotechnology* **2013,** 24, (37), 375701.

47. Hod, O. *ChemPhysChem* **2013,** 14, (11), 2376-2391.

48. Hod, O. *Physical Review B: Condensed Matter* **2012,** 86, (7), 075444.

49. Feng, X.; Kwon, S.; Park, J. Y.; Salmeron, M. *ACS Nano* **2013,** 7, (2), 1718-1724.

50. Washizu, H.; Kajita, S.; Tohyama, M.; Ohmori, T.; Nishino, N., *et al. Faraday Discussions* **2012,** 156, (0), 279-291.

51. Kikuchi, K.; Yoshida, M.; Maekawa, T.; Watanabe, H. *Chemical Physics Letters* **1991,** 185, (3–4), 335-338.

52. Berman, D.; Erdemir, A.; Sumant, A. V. *Materials Today* **2014,** 17, (1), 31-42.

53. Penkov, O.; Kim, H.-J.; Kim, H.-J.; Kim, D.-E. *International Journal of Precision Engineering and Manufacturing* **2014,** 15, (3), 577-585.

54. Guo, W.; Yin, J.; Qiu, H.; Guo, Y.; Wu, H., *et al. Friction* **2014,** 2, (3), 209-225.

55. Spear, J. C.; Custer, J. P.; Batteas, J. D. *Nanoscale* **2015,** (in revision).

56. Yitian, P.; Zhuoqiong, W.; Cong, L. *Nanotechnology* **2014,** 25, (30), 305701.

57. Paolicelli, G.; Tripathi, M.; Corradini, V.; Candini, A.; Valeri, S. *Nanotechnology* **2015,** 26, (5), 055703.

58. Robinson, B. J.; Kay, N. D.; Kolosov, O. V. *Langmuir* **2013,** 29, (25), 7735-7742.

59. Muñoz, R.; Gómez-Aleixandre, C. *Chemical Vapor Deposition* **2013,** 19, (10-11-12), 297-322.

60. Zhang, Y.; Zhang, L.; Zhou, C. *Accounts of Chemical Research* **2013,** 46, (10), 2329-2339.

61. Egberts, P.; Han, G. H.; Liu, X. Z.; Johnson, A. T. C.; Carpick, R. W. *ACS Nano* **2014,** 8, (5), 5010-5021.

62. Yan, J.; Yang, L.; Bing, L.; Xiaofei, Y.; Tongwei, H., *et al. Nanotechnology* **2012,** 23, (49), 495703.

63. Berman, D.; Erdemir, A.; Sumant, A. V. *Carbon* **2013,** 59, (0), 167-175.

64. Berman, D.; Deshmukh, S. A.; Sankaranarayanan, S. K. R. S.; Erdemir, A.; Sumant, A. V. *Advanced Functional Materials* **2014,** 24, (42), 6640-6646.

65. Kinoshita, H.; Nishina, Y.; Alias, A. A.; Fujii, M. *Carbon* **2014,** 66, (0), 720-723.

66. Wang, Y.; Pu, J.; Xia, L.; Ding, J.; Yuan, N., *et al. Tribology Letters* **2014,** 53, (1), 207-214.

67. Pu, J.; Mo, Y.; Wan, S.; Wang, L. *Chemical Communications* **2014,** 50, (4), 469-471.

68. Huang, T.; Xin, Y.; Li, T.; Nutt, S.; Su, C., *et al. ACS Applied Materials and Interfaces* **2013,** 5, (11), 4878-4891.

69. Xuemei, L.; Jun, Y.; Jianxin, Z.; Wanlin, G. *Nanotechnology* **2014,** 25, (10), 105701.

70. Chen, S.; Brown, L.; Levendorf, M.; Cai, W.; Ju, S.-Y., *et al. ACS Nano* **2011,** 5, (2), 1321-1327.

71. Li, L. H.; Cervenka, J.; Watanabe, K.; Taniguchi, T.; Chen, Y. *ACS Nano* **2014,** 8, (2), 1457-1462.

72. Tevet, O.; Von-Huth, P.; Popovitz-Biro, R.; Rosentsveig, R.; Wagner, H. D., *et al. Proceedings of the National Academy of Sciences of the United States of America* **2011,** 108, (50), 19901-19906.

73. Lahouij, I.; Vacher, B.; Dassenoy, F. *Lubrication Science* **2014,** 26, (3), 163-173.

74. Lahouij, I.; Vacher, B.; Martin, J.-M.; Dassenoy, F. *Wear* **2012,** 296, (1–2), 558-567.

75. Ratoi, M.; Niste, V.; Walker, J.; Zekonyte, J. *Tribology Letters* **2013,** 52, (1), 81-91.

76. Xu, Z.; Hu, K.; Han, C.; Hu, X.; Xu, Y. *Tribology Letters* **2013,** 49, (3), 513-524.

77. Yadgarov, L.; Petrone, V.; Rosentsveig, R.; Feldman, Y.; Tenne, R., *et al. Wear* **2013,** 297, (1–2), 1103-1110.

78. Kogovšek, J.; Kalin, M. *Tribology Letters* **2014,** 53, (3), 585-597.

79. He, X.; Xiao, H.; Choi, H.; Díaz, A.; Mosby, B., *et al. Colloids and Surfaces A: Physicochemical and Engineering Aspects* **2014,** 452, (0), 32-38.

80. He, X.; Chen, Y.; Zhao, H.; Sun, H.; Lu, X., *et al. Friction* **2013,** 1, (4), 327-332.

81. Kase, T.; Ogino, T. *The Journal of Physical Chemistry C* **2013,** 117, (31), 15991-15995.

82. Luo, Z.; Lu, Y.; Singer, D. W.; Berck, M. E.; Somers, L. A., *et al. Chemistry of Materials* **2011,** 23, (6), 1441-1447.

83. Maboudian, R.; Carraro, C. *Annual Review of Physical Chemistry* **2004,** 55, (1), 35-54.

84. Hao, C.; Yin, Y.; Shaohua, C. *Journal of Physics D: Applied Physics* **2013,** 46, (20), 205303.

85. Wei, G.; Rui, H. *Journal of Physics D: Applied Physics* **2011,** 44, (45), 452001.

86. Aitken, Z. H.; Huang, R. *Journal of Applied Physics* **2010,** 107, (12), 123531-10.

87. Scharfenberg, S.; Mansukhani, N.; Chialvo, C.; Weaver, R. L.; Mason, N. *Applied Physics Letters* **2012,** 100, (2), 021910-3.

88. Zhang, J.; Wang, Y.; Wang, X. *Nanoscale* **2013,** 5, (23), 11598-11603.

89. Wagner, T. J. W.; Vella, D. *Applied Physics Letters* **2012,** 100, (23), 233111-4.

90. Li, T.; Zhang, Z. *Nanoscale Research Letters* **2009,** 5, (1), 169-173.

91. Reserbat-Plantey, A.; Kalita, D.; Han, Z.; Ferlazzo, L.; Autier-Laurent, S., *et al. Nano Letters* **2014,** 14, (9), 5044-5051.

92. Prosser, J. H.; Brugarolas, T.; Lee, S.; Nolte, A. J.; Lee, D. *Nano Letters* **2012,** 12, (10), 5287-5291.

93. Cook, K. T.; Tettey, K. E.; Bunch, R. M.; Lee, D.; Nolte, A. J. *ACS Applied Materials & Interfaces* **2012,** 4, (12), 6426-6431.

94. Sader, J. E.; Chon, J. W. M.; Mulvaney, P. *Review of Scientific Instruments* **1999,** 70, (10), 3967-3969.

95. Batteas, J.; Quan, X.; Weldon, M. *Tribology Letters* **1999,** 7, (2-3), 121-128.

96. Ishigami, M.; Chen, J. H.; Cullen, W. G.; Fuhrer, M. S.; Williams, E. D. *Nano Letters* **2007,** 7, (6), 1643-1648.

97. Cullen, W. G.; Yamamoto, M.; Burson, K. M.; Chen, J. H.; Jang, C., *et al. Physical Review Letters* **2010,** 105, (21), 215504.

98. Zabel, J.; Nair, R. R.; Ott, A.; Georgiou, T.; Geim, A. K., *et al. Nano Letters* **2011,** 12, (2), 617-621.

99. Metzger, C.; Rémi, S.; Liu, M.; Kusminskiy, S. V.; Castro Neto, A. H., *et al. Nano Letters* **2009,** 10, (1), 6-10.

100. Ding, F.; Ji, H.; Chen, Y.; Herklotz, A.; Dörr, K., *et al. Nano Letters* **2010,** 10, (9), 3453-3458.

101. Pan, W.; Xiao, J.; Zhu, J.; Yu, C.; Zhang, G., *et al. Scientific Reports* **2012,** 2.

102. Zhao, Y.; Liu, X.; Lei, D. Y.; Chai, Y. *Nanoscale* **2014,** 6, (3), 1311-1317.

103. Scharfenberg, S.; Rocklin, D. Z.; Chialvo, C.; Weaver, R. L.; Goldbart, P. M., *et al. Applied Physics Letters* **2011,** 98, (9), 091908-3.

104. Osvath, Z.; Gergely-Fulop, E.; Nagy, N.; Deak, A.; Nemes-Incze, P., *et al. Nanoscale* **2014,** 6, (11), 6030-6036.

105. Persson, B. N. J. *Surface Science Reports* **2006,** 61, (4), 201-227.

106. Schwarz, U. D. *Journal of Colloid and Interface Science* **2003,** 261, (1), 99-106.

107. Martín, J.; Muñoz, M.; Encinar, M.; Calleja, M.; Martín-González, M. *Langmuir* **2014,** 30, (18), 5217-5223.

108. Lafkioti, M.; Krauss, B.; Lohmann, T.; Zschieschang, U.; Klauk, H., *et al. Nano Letters* **2010,** 10, (4), 1149-1153.

109. Ou, J.; Wang, Y.; Wang, J.; Liu, S.; Li, Z., *et al. The Journal of Physical Chemistry C* **2011,** 115, (20), 10080-10086.

110. Ewers, B. W.; Batteas, J. D. *The Journal of Physical Chemistry C* **2012,** 116, (48), 25165-25177.

111. Jones, R. L.; Pearsall, N. C.; Batteas, J. D. *The Journal of Physical Chemistry C* **2009,** 113, (11), 4507-4514.

112. Nair, R. R.; Blake, P.; Grigorenko, A. N.; Novoselov, K. S.; Booth, T. J., *et al. Science* **2008,** 320, (5881), 1308.

113. Kim, K. S.; Zhao, Y.; Jang, H.; Lee, S. Y.; Kim, J. M., *et al. Nature* **2009,** 457, (7230), 706-710.

114. Schedin, F.; Geim, A. K.; Morozov, S. V.; Hill, E. W.; Blake, P., *et al. Nature Materials* **2007,** 6, (9), 652-655.

115. Feng, P. X. L. *Nature Nanotechnology* **2013,** 8, (12), 897-898.

116. Miao, T.; Yeom, S.; Wang, P.; Standley, B.; Bockrath, M. *Nano Letters* **2014,** 14, (6), 2982-2987.

117. Qian, Z.; Liu, F.; Hui, Y.; Kar, S.; Rinaldi, M. *Nano Letters* **2015,** 15, (7), 4599-4604.

118. Bunch, J. S.; Dunn, M. L. *Solid State Communications* **2012,** 152, (15), 1359-1364.

119. Benjamin, F. T.; Ronald, A. C., Jr.; John, W. M. *Journal of Micromechanics and Microengineering* **2013,** 23, (10), 103001.

120. Williams, J. A.; Le, H. R. *Journal of Physics D: Applied Physics* **2006,** 39, (12), R201.

121. Zong, Z.; Chen, C.-L.; Dokmeci, M. R.; Wan, K.-t. *Journal of Applied Physics* **2010,** 107, (2), 026104-3.

122. Li, P.; You, Z.; Cui, T. *Sensors and Actuators A: Physical* **2014,** 217, (0), 56-61.

123. Yoon, T.; Shin, W. C.; Kim, T. Y.; Mun, J. H.; Kim, T.-S., *et al. Nano Letters* **2012,** 12, (3), 1448-1452.

124. Koenig, S. P.; Boddeti, N. G.; Dunn, M. L.; Bunch, J. S. *Nature Nanotechnology* **2011,** 6, (9), 543-546.

125. Pourzand, H.; Tabib-Azar, M. *Applied Physics Letters* **2014,** 104, (17), 171603.

126. Jiang, T.; Zhu, Y. *Nanoscale* **2015**.

127. Berman, D.; Deshmukh, S. A.; Sankaranarayanan, S. K. R. S.; Erdemir, A.; Sumant, A. V. *Science* **2015,** 348, (6239), 1118-1122.

128. Paek, E.; Hwang, G. S. *Journal of Applied Physics* **2013,** 113, (16), 164901.

129. Spear, J. C.; Custer, J. P.; Batteas, J. D. *Nanoscale* **2015,** 7, (22), 10021-10029.

130. Castro Neto, A. H.; Guinea, F.; Peres, N. M. R.; Novoselov, K. S.; Geim, A. K. *Reviews of Modern Physics* **2009,** 81, (1), 109-162.

131. Das, A.; Pisana, S.; Chakraborty, B.; Piscanec, S.; Saha, S. K., *et al. Nat Nano* **2008,** 3, (4), 210-215.

132. Ferrari, A. C.; Basko, D. M. *Nature Nanotechnology* **2013,** 8, (4), 235-246.

133. Ni, Z. H.; Yu, T.; Lu, Y. H.; Wang, Y. Y.; Feng, Y. P., *et al. ACS Nano* **2008,** 2, (11), 2301-2305.

134. Das, A.; Pisana, S.; Chakraborty, B.; Piscanec, S.; Saha, S. K., *et al. Nature Nanotechnology* **2008,** 3, (4), 210-215.

135. Tsukamoto, T.; Yamazaki, K.; Komurasaki, H.; Ogino, T. *The Journal of Physical Chemistry C* **2012,** 116, (7), 4732-4737.

136. Ryan, B.; Luiz Gustavo, C.; Ado, J.; Vamivakas, A. N.; Lukas, N. *Nanotechnology* **2015,** 26, (17), 175702.

137. Li, Z.; Wang, Y.; Kozbial, A.; Shenoy, G.; Zhou, F., *et al. Nature Materials* **2013,** 12, (10), 925-931.

138. Farshchi-Tabrizia, M.; Kappl, M.; Butt, H.-J. *Journal of Adhesion Science and Technology* **2008,** 22, (2), 181-203.

139. Ata, A.; Rabinovich, Y. l.; Singh, R. K. *Journal of Adhesion Science and Technology* **2002,** 16, (4), 337-346.

140. Deng, Z.; Klimov, N. N.; Solares, S. D.; Li, T.; Xu, H., *et al. Langmuir* **2012,** 29, (1), 235-243.

141. Cheng, H.; Hu, Y. *Advances in Colloid and Interface Science* **2012,** 171–172, 53-65.

142. Onclin, S.; Ravoo, B. J.; Reinhoudt, D. N. *Angewandte Chemie International Edition* **2005,** 44, (39), 6282-6304.

143. Wang, Y.; Lieberman, M. *Langmuir* **2003,** 19, (4), 1159-1167.

144. Poda, A.; Anderson, A.; Ashurst, W. R. *Applied Surface Science* **2010,** 256, (22), 6805-6813.

145. Parikh, A. N.; Allara, D. L.; Azouz, I. B.; Rondelez, F. *The Journal of Physical Chemistry* **1994,** 98, (31), 7577-7590.

146. Manifar, T.; Rezaee, A.; Sheikhzadeh, M.; Mittler, S. *Applied Surface Science* **2008,** 254, (15), 4611-4619.

147. McGovern, M. E.; Kallury, K. M. R.; Thompson, M. *Langmuir* **1994,** 10, (10), 3607-3614.

148. Liu, L.-H.; Yan, M. *Accounts of Chemical Research* **2010,** 43, (11), 1434-1443.

149. Liu, L.-H.; Yan, M. *Journal of Materials Chemistry* **2011,** 21, (10), 3273-3276.

150. Al-Bataineh, S. A.; Luginbuehl, R.; Textor, M.; Yan, M. *Langmuir* **2009,** 25, (13), 7432-7437.

151. Liu, L.-H.; Yan, M. *Nano Letters* **2009,** 9, (9), 3375-3378.

152. Lee, D.; Ahn, G.; Ryu, S. *Journal of the American Chemical Society* **2014,** 136, (18), 6634-6642.

153. Rastei, M. V.; Heinrich, B.; Gallani, J. L. *Physical Review Letters* **2013,** 111, (8), 084301.

APPENDIX A

SUPPLEMENTAL DATA FOR CHAPTER II

Comparative Studies of Graphene Layers on Oxidized SiO_2/Si(100) Substrates

To calibrate the results from studies of graphene on the rough surfaces the same water-soluble tape method was used to fabricate graphene samples on thermally oxidized (~90 nm oxide thickness) SiO_2/Si(100) as a comparison. Figure A.1a shows a Raman map of the 2D/G intensity ratio of an example graphene sample region shown as white and graphite as maroon. Figure A.1b and A.1c show the contact mode Atomic Force Microscopy (AFM) topography image and the corresponding friction map. The graphene region appears to have an overall higher friction than the multilayer regions with some areas displaying various friction domains due to differences in the crystallographic orientation of the lattice.[153] The relative friction signal was averaged from individual friction maps on different layers of graphene and normalized to the value for bulk graphite (determined *in situ* from thick layers on the surface). Figure A.2 shows the normalized friction values comparing single-layer, bilayer and bulk-like graphene (greater than five layers) with friction decreasing with increasing layer thickness. Graphene is seen to have higher friction than multi-layers which is characteristic of the "puckering effect".[33] Figure A.3a shows a contact mode AFM image containing one to three layers of graphene on silica nanoparticles and the corresponding adhesion map (Figure A.3b) generated from a grid array (32 x 32) of force-distance curves where the tip-surface pull-off force was measured.

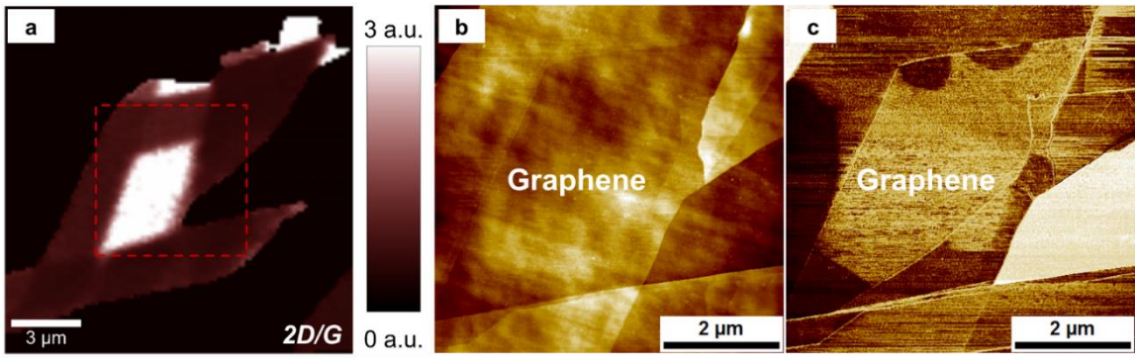

Figure A.1. (a) Raman map of the 2D/G intensity ratio for a single and multi-layer graphene sample region on thermally oxidized (~90 nm oxide thickness) SiO_2/Si(100) with graphene having the highest intensity shown as white and graphite as maroon. (b) Contact AFM topography image of the sample region from the red box in (a) and the corresponding friction map (c).

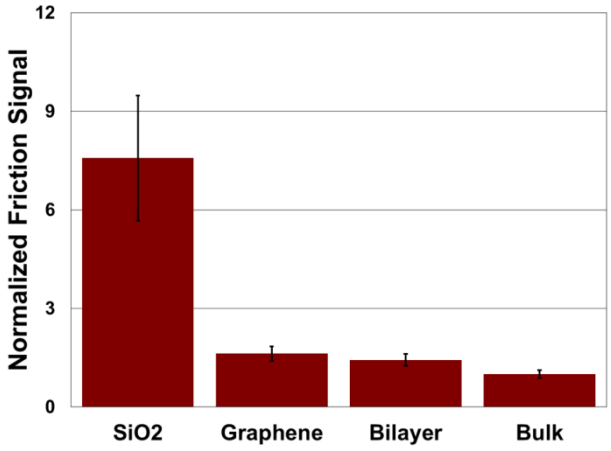

Figure A.2. Friction values of SiO_2/Si(100) and graphene layers measured on an unfunctionalized substrate and normalized to that of bulk graphite. The friction trend shows the "puckering effect" with decreasing friction as the number of layers increase.

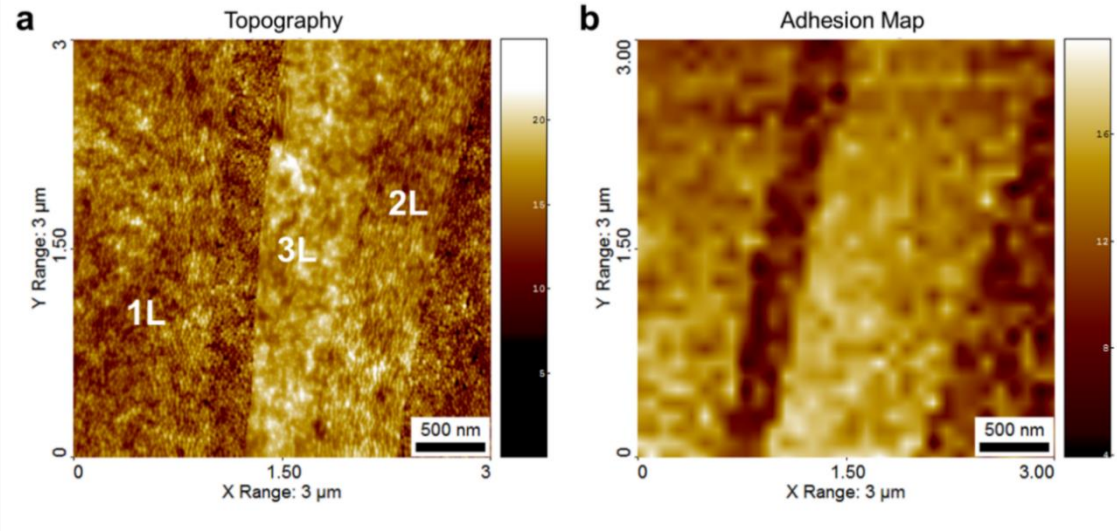

Figure A.3. (a) Contact AFM topography image showing silica nanoparticles and one to three graphene layers. (b) Corresponding adhesion map of the sample region in (a) containing a 32 x 32 grid array of force-distance curves used to measure the pull-off force

Comparative Studies of Graphene Layers on OTS Functionalized SiO_2/Si(100) and Spincoated SiO_2 Nanoparticle/Si(100) Substrates

For reference samples to compare to the rough surfaces functionalized with octadecyltrichlorosilane (OTS), thermally oxidized (~90 nm oxide thickness) SiO_2/Si(100) substrates were also functionalized with OTS and graphene was mechanically exfoliated on the surface using the water soluble tape method. OTS substrates were characterized with infrared spectroscopy before graphene transfer with a typical spectrum shown in Figure A.5. Figure A.6 is a contact mode topography image and line profile showing similar partial conformity and roughness changes on the functionalized rough surface as observed on the unfunctionalized silica nanoparticles.

The partial conformity is due to strain which was measured using Raman microspectroscopy and the characteristic peak shifts to lower wavenumber on the rough substrates are shown in Figure A.7.

Figure A.8a shows a Raman map of the 2D/G intensity ratio of an example graphene sample on a thermally oxidized wafer with graphene shown as white and graphite as maroon. Figure S8b and 85c show the contact mode AFM topography image and the corresponding friction map comparing OTS, single-layer, bi-layer, tri-layer and bulk-like graphene. The relative friction signal was averaged from individual friction maps on the different layers of graphene and normalized to the value for bulk graphite (determined *in situ* from thick layers on the surface). Figure A.9 shows the normalized friction values comparing single-layer, bi-layer and bulk-like graphene (greater than five layers) with friction decreasing with increasing layer thickness. Graphene on OTS is seen to also have higher friction than multi-layers which is characteristic of the "puckering effect".[33]

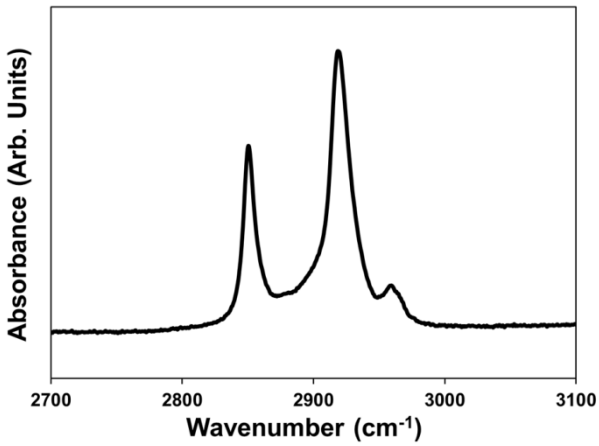

Figure A.4. Example infrared spectrum of an OTS functionalized nanoparticle film showing the characteristic CH_2 asymmetric stretching band at 2918 cm^{-1}.

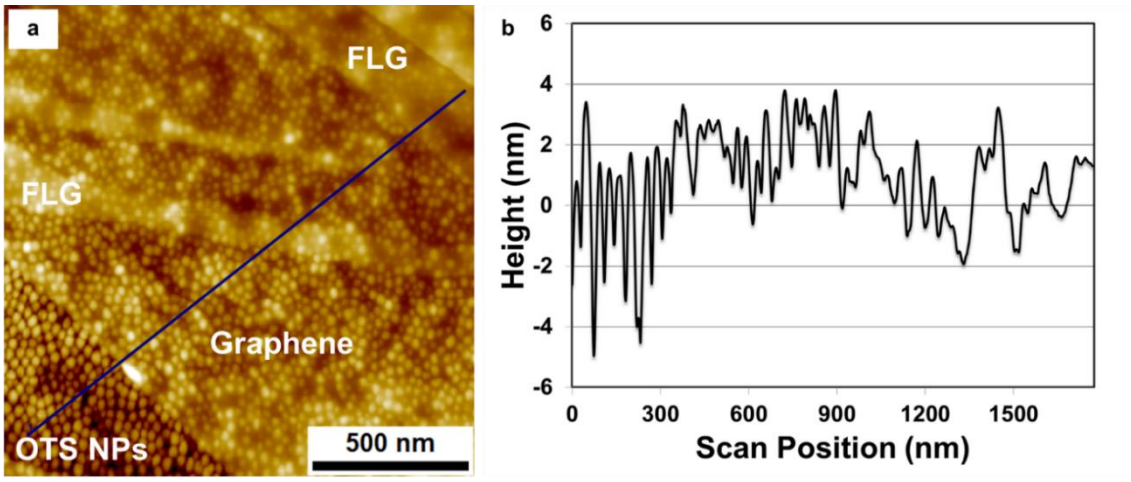

Figure A.5. (a) Contact mode AFM topography image of graphene and multilayer graphene on a rough OTS nanoparticle surface. (b) Line profile from the blue line in (a) showing the decrease in roughness from the OTS nanoparticles to the different layers.

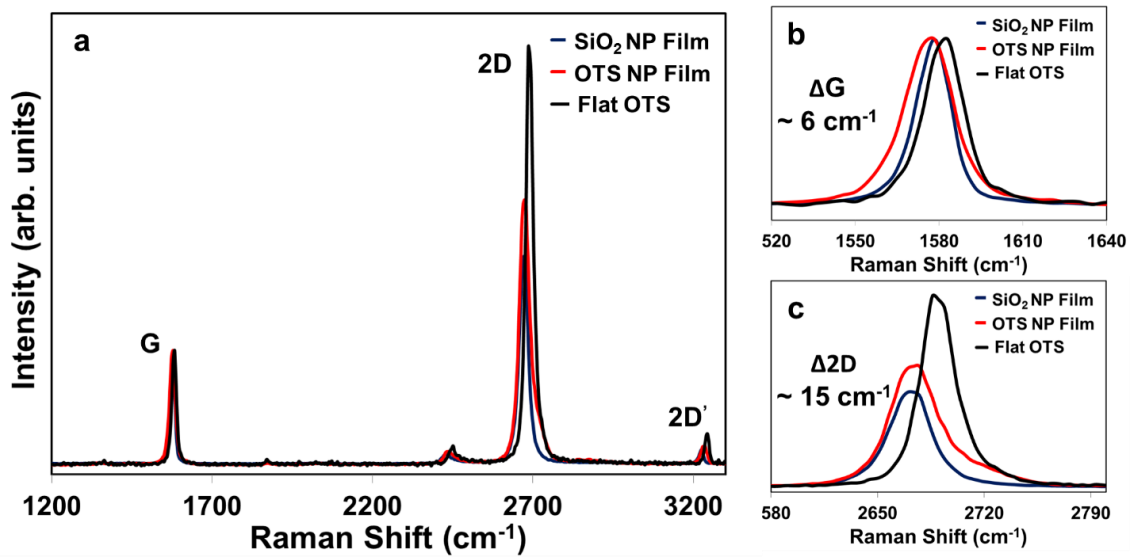

Figure A.6. (a) Raman spectra of graphene on an unfunctionalized and an OTS functionalized nanoparticle surface compared to a flat OTS functionalized surface showing the shift to lower wavenumbers on rough surfaces due to strain in the graphene lattice. (b) and (c) are larger views of the G and 2D peak shifts. The Raman spectra were normalized to the intensity of the G peak.

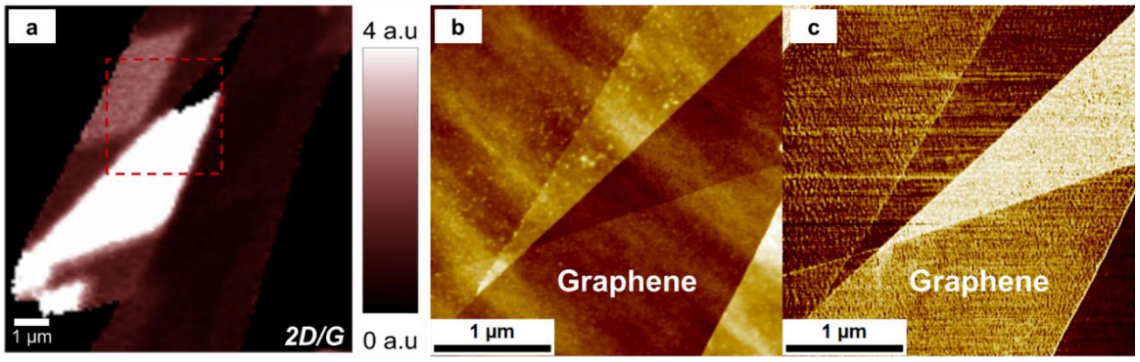

Figure A.7. **(**a) Raman map of the 2D/G intensity ratio for a single and multi-layer graphene sample region on an OTS functionalized SiO2/Si(100) substrate with graphene having the highest intensity shown as white and graphite as maroon. (b) Contact AFM topography image of the sample region from the red box in (a) and the corresponding friction map (c).

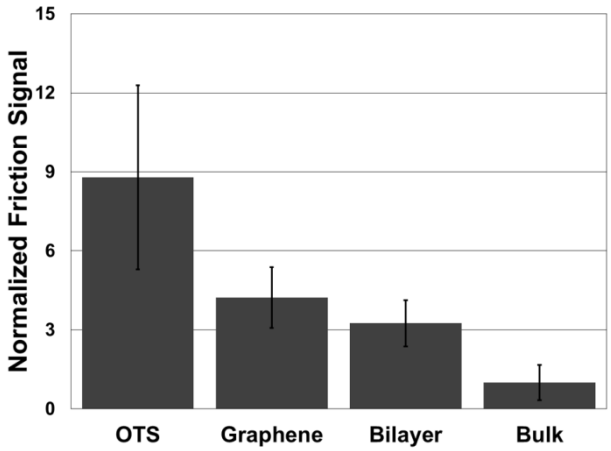

Figure A.8. Friction values of graphene layers on a flat OTS functionalized substrate normalized to that of bulk graphite. The friction trend shows the "puckering effect" with decreasing friction as the number of layers increase.

APPENDIX B

SUPPLEMENTAL DATA FOR CHAPTER III

Adhesion Data for Graphene on the 50 nm Nanoparticle Sample

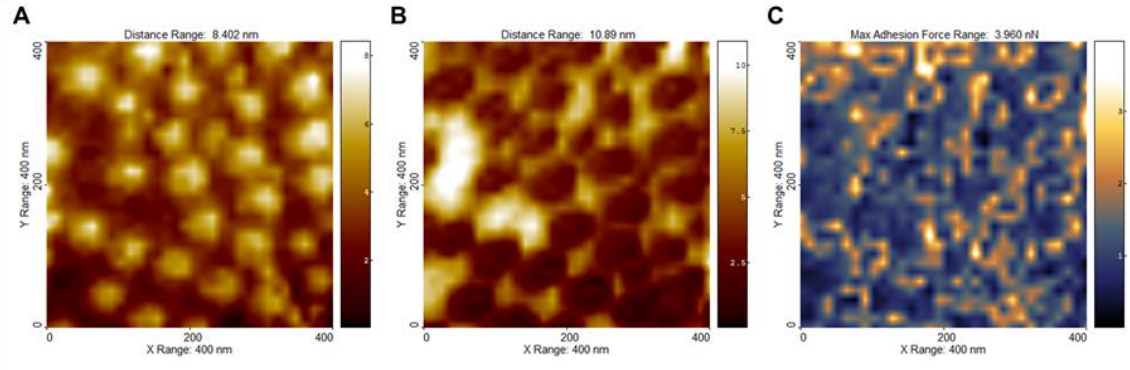

Figure B.1. Deflection height images at ~20 nN (A) and -3 nN (B) extracted from a 32x32 grid array of force-distance curves on the 50 nm nanoparticle graphene sample. Adhesion map (C) calculated from the pull-off forces showing adhesion variation across the rough surface.

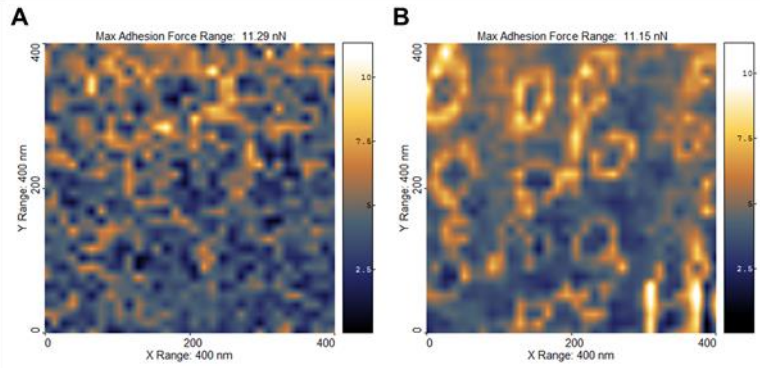

Figure B.2. Adhesion maps from a 32x32 grid array of force-distance curves with a silicon AFM tip on the 50 nm nanoparticle samples under (A) dry nitrogen conditions with humidity <5% and (B) ambient conditions with humidity ~40-45%. The magnitude of the capillary force was reduced under dry nitrogen but some adhesion variations are still observed due to changes in topography and contact to the tip.

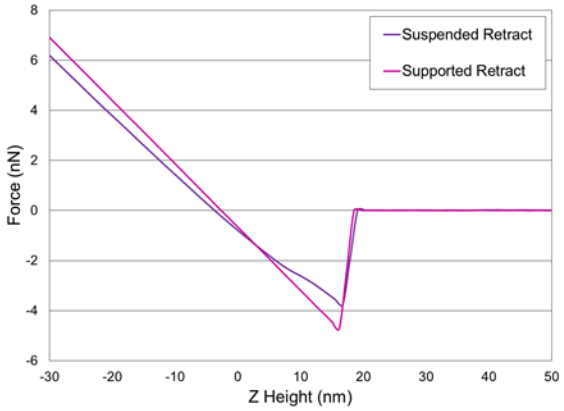

Figure B.3. Example force-distance curves showing graphene adhesion variations depending on tip location on top of a single 50 nm nanoparticle and on suspended regions of graphene.

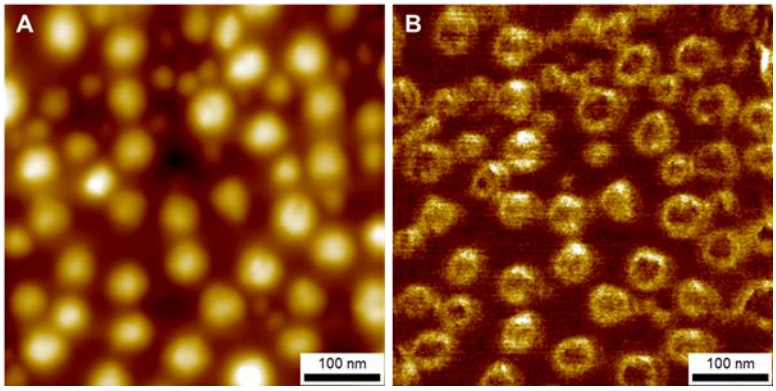

Figure B.4. AFM contact mode topography and friction map of graphene on 50 nm nanoparticles under 20 nN tip load.

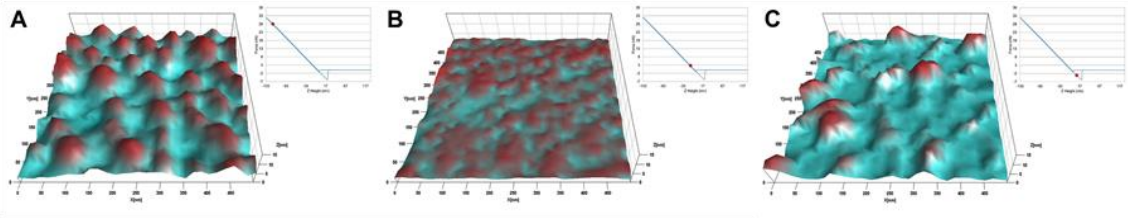

Figure B.5. 3D deflection height images extracted from a 32x32 grid array of force-distance curves on the 50 nm nanoparticle sample showing the dynamic nature of graphene under (A) ~28 nN load (B) ~3 nN load and (C) ~ -3 nN load.

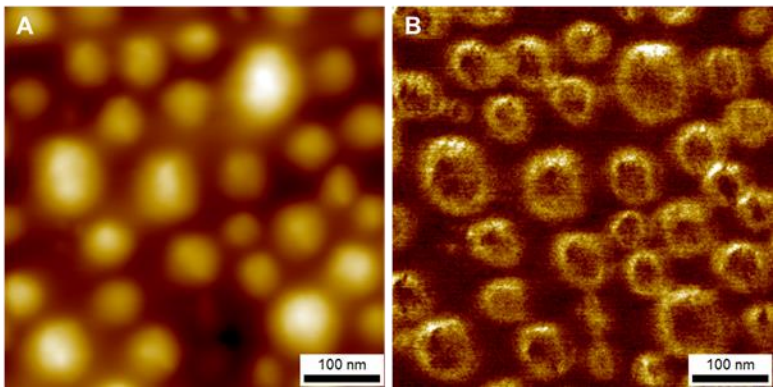

Figure B.6. AFM contact mode topography and friction map of graphene on 85 nm nanoparticles under 20 nN tip load.

APPENDIX C

SUPPLEMENTAL DATA FOR CHAPTER IV

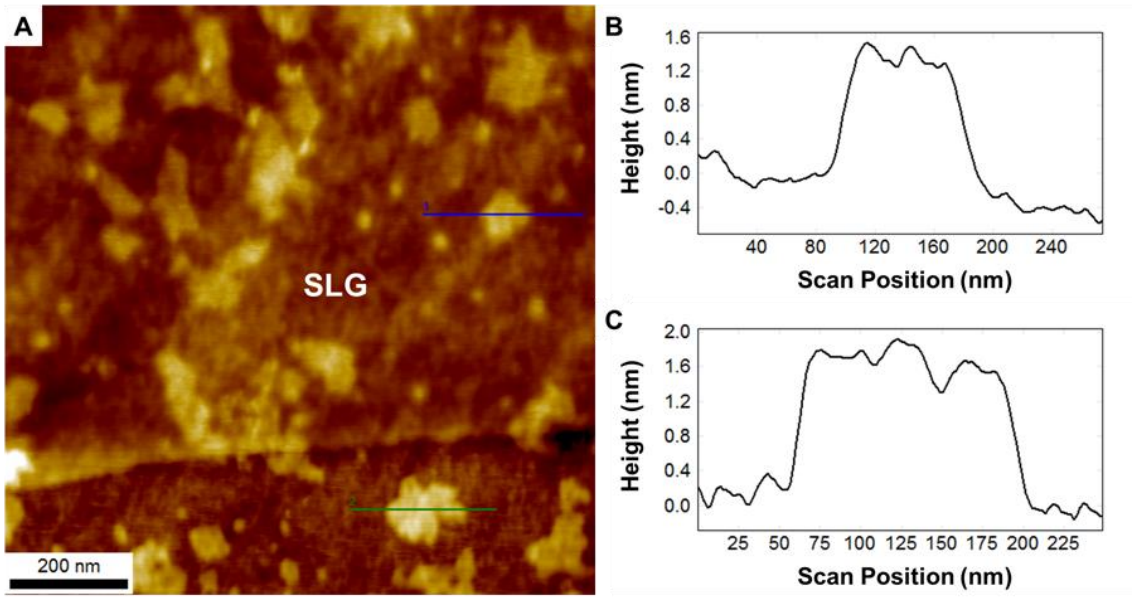

Figure C.1. (A) AFM topography of graphene on an oxidized Si(100) substrate functionalized with OTS islands and PFPA-silane before thermal activation of the PFPA. (B) Line profile corresponding to the blue line in (A) and (C) line profile corresponding to the green line in (A) showing the relative heights of the OTS islands on (B) and off (C) the graphene monolayer.

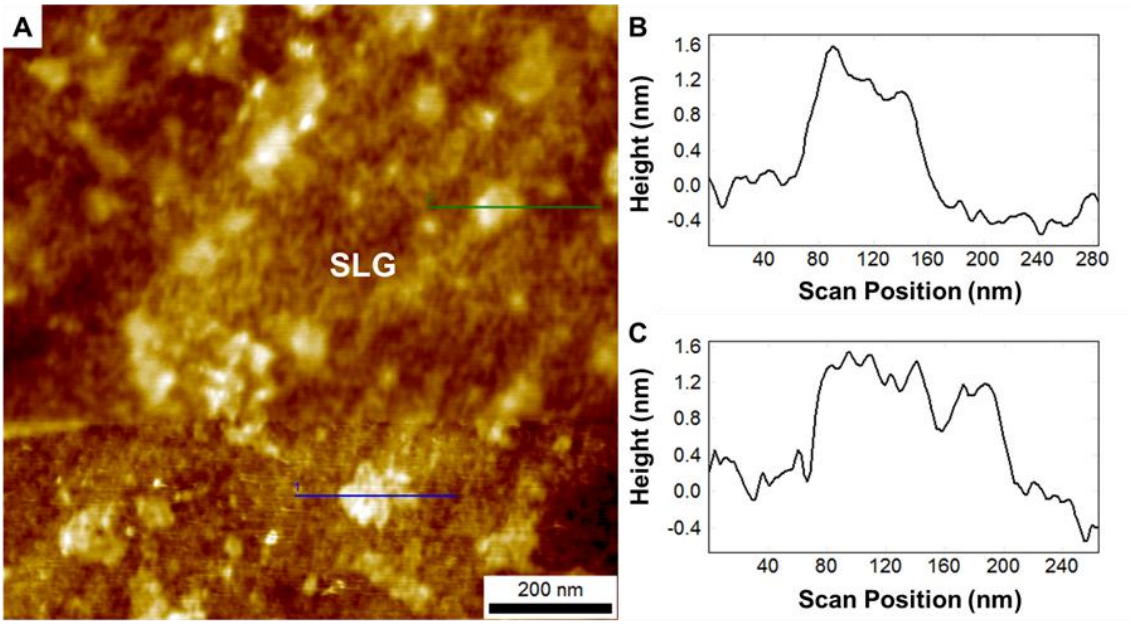

Figure C.2. (A) AFM topography of graphene on an oxidized Si(100) substrate functionalized with OTS islands and PFPA-silane after thermal activation of the PFPA. (B) Line profile corresponding to the green line in (A) and (C) line profile corresponding to the blue line in (A) showing the relative heights of the OTS islands on (B) and off (C) the graphene monolayer.

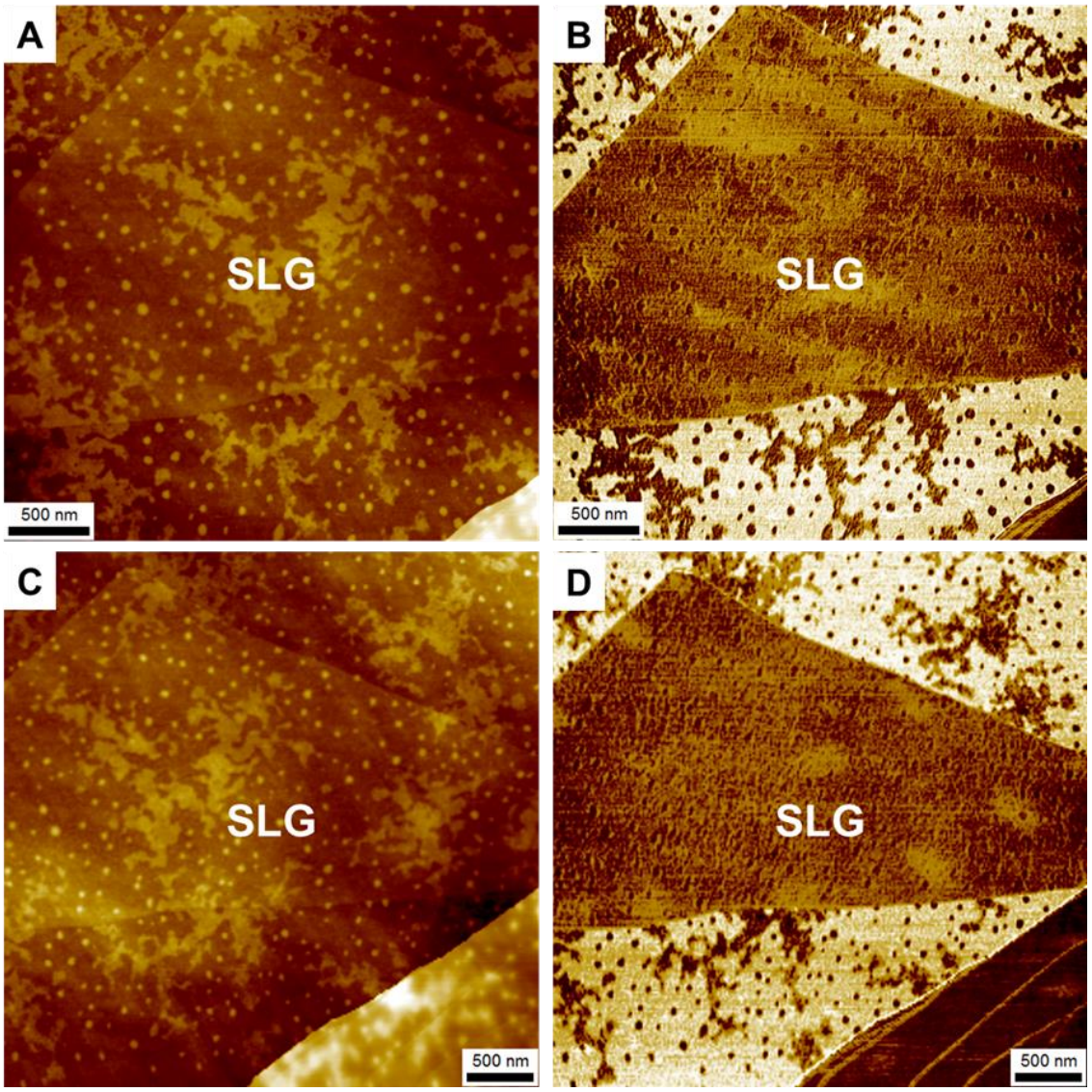

Figure C.3. AFM topographies (A) and (C) and friction maps (B) and (D) of monolayer graphene on an oxidized Si(100) functionalized with OTS islands before (A) and (B) and after (C) and (D) thermal treatment of the sample.

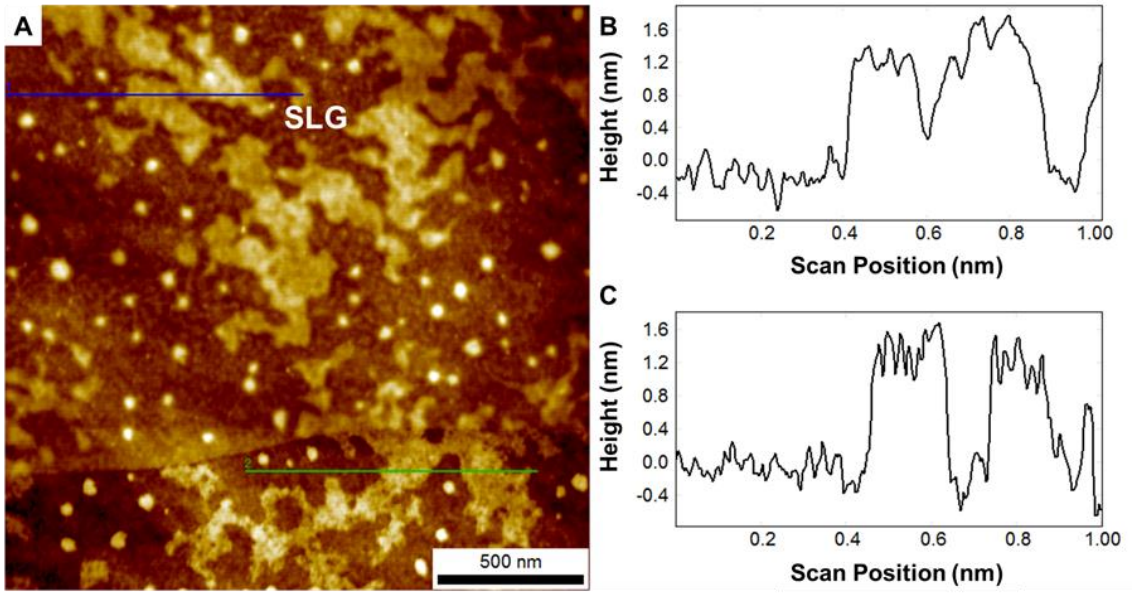

Figure C.4. (A) AFM topography of graphene on an oxidized Si(100) substrate functionalized with OTS islands after thermal treatment of the sample. (B) Line profile corresponding to the blue line in (A) and (C) line profile corresponding to the green line in (A) showing the relative heights of the OTS islands on (B) and off (C) the graphene monolayer.

APPENDIX D

SAMPLE PREPARATION AND EXPERIMENTAL METHODS

Sample Preparation

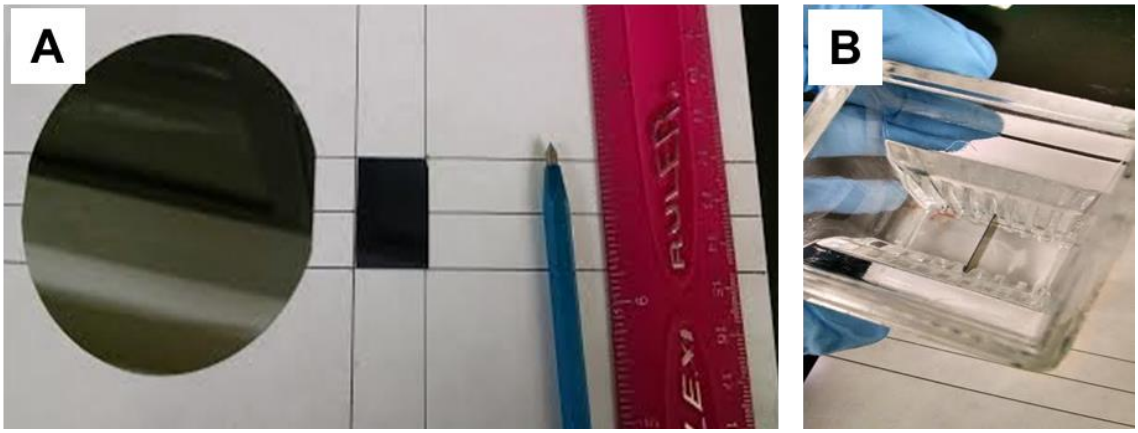

Figure D.1. (A) A silicon wafer and a score cut silicon wafer using a diamond scribe and a ruler. (B) Score cut silicon wafer placed in a staining jar to separate the wafers for cleaning in a base piranha solution.

Substrate Cleaning

Samples were fabricated in this project by first cleaning a Si(100) substrate. Si(100) wafers were score cut to the size needed for the sample (typically 2.5 cm x 2 cm) and then rinsed with high purity water to remove any excess debris (Figure D.1A). The cut wafers were then cleaned in a basic piranha solution composed of high purity H_2O, NH_4OH, and H_2O_2 in a 4:1:1 volumetric ratio and heated in an oven at 85°C up to 20 min (Figure D.1B). The cut wafers were then thoroughly rinsed with high purity water,

ethanol, and dried with streaming nitrogen. This cleaning method allows for removal of organic contaminants and other small particle debris while leaving the Si(100) hydroxylated and hydrophilic. It is noted that this method can also cause etching of the silica surface but it can be slowed by diluting the mixture or lowering the temperature.

Thermal Oxidation

To create substrates with optical contrast for optically locating monolayer graphene samples, the cut and cleaned Si wafers were thermally oxidized. The substrates were placed in a kiln and heated to 1050°C for ~1 hr and 25 min to grow an oxidation layer with ~ 90 nm thickness. After heating the substrates have a pink/purple color which confirms the oxidation layer is near the desired thickness.

Nanoparticle Spincoating

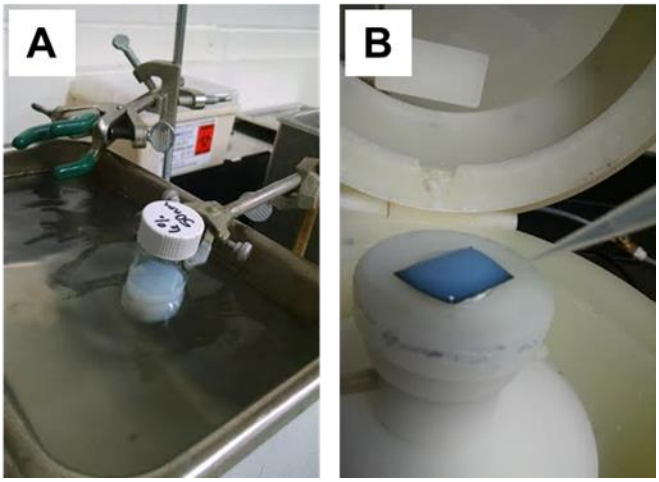

Figure D.2. (A) Silica nanoparticles diluted and placed in a water bath sonicator for breaking up aggregates before spincoating. (B) 400 µl of diluted nanoparticle solution pipetted on a clean silicon wafer placed in the center of the spincoater.

Nanoparticles were diluted from the stock wt% to ~4.7 – 6 wt% (depending on size 6 nm – 85 nm) with high purity water with the total volume kept at least 10 ml in a 20 ml vial for more efficient sonication. The diluted nanoparticles were sonicated (Figure D.2A) using high power for 30 – 60 min until spincoated to break up nanoparticle aggregates for more homogeneous nanoparticle films. The water level around the nanoparticle solution vial was also adjusted for maximum agitation to break up the nanoparticle aggregates more efficiently. Clean silicon substrates were then placed on the spincoater and 400 μl of a nanoparticle solution was pipetted on the wafer (enough that will spread out and cover most of the wafer) as shown in Figure D.2B. The spincoating parameters used were 2000 rpm and 665 rpm/s for up to 2 min or until all excess solution dried. The nanoparticle films were then placed in a kiln and heated to 500 °C for 5 hrs.

Chemical Functionalization

To chemically functionalize substrates with self-assembled monolayers, the substrates were first cleaned with the basic piranha as previously described. A silane/hexanes solution was prepared under nitrogen in a pyrex jar and the sample was then immersed up to 24 hrs for full film formation or shorter for island formation. The concentrations used were typically ~1 mM and the solvents included hexanes or toluene depending on the solubility of silane molecule used. After functionalization the samples were sonicated in tetrahydrofuran for ~ 30 min to remove excess molecules and rinsed with high purity water and ethanol before drying with streaming nitrogen. For functionalization of AFM tips a similar procedure was used including the same solvents

and concentrations except the tips were not sonicated but dipped in solvents for rinsing. The tips were first cleaned in the basic piranha solution except without heating and then functionalized by holding the tip in a silane solution for ~ 1 min. To rinse the functionalized tips they were dipped in hexanes and toluene to remove the excess molecules. Toluene was found to be the best solvent for efficiently rinsing excess residue from the functionalized surfaces which is especially important for functionalized tips as too much residue can affect the ability to precisely focus the laser on the back of the cantilever and reduce the detected signal intensity.

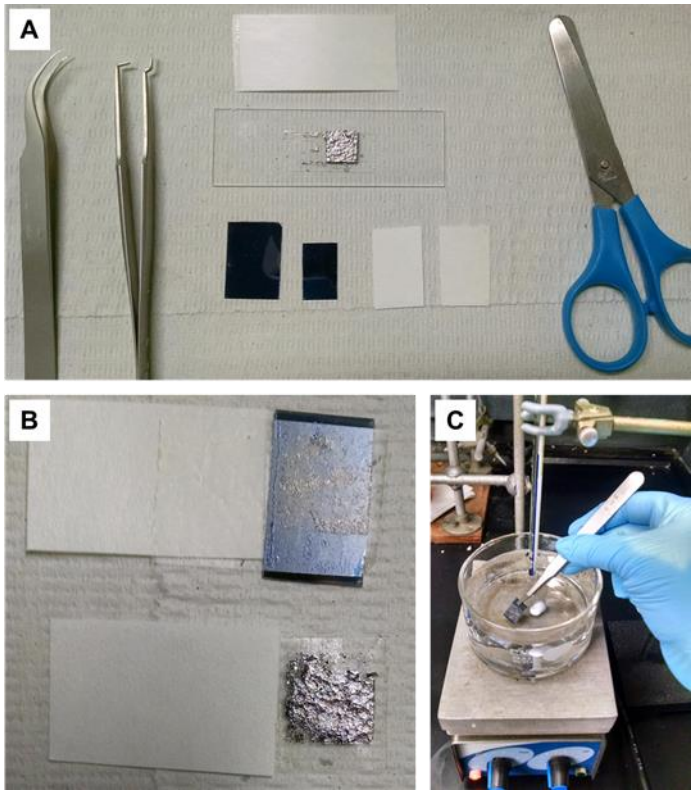

Figure D.3. (A) Setup used for exfoliating graphene on silica substrates including tweezers, silicon substrates, water soluble tape, graphite, and scissors. (B) Graphite exfoliated with water soluble tape and placed on a silicon wafer. (C) Heated water bath setup used for dissolving the water soluble tape to transfer graphite to the substrate.

Graphene Exfoliation

To fabricate graphene flakes on silica substrates graphite was mechanically exfoliated using water soluble tape. Substrates that had been previously thermally oxidized or spincoated with silica nanoparticles were first score cut into half and then cleaned with UV/ozone for 5 min followed by rinsing with high purity water, ethanol and dried with streaming nitrogen. A fresh piece of water soluble tape was cut with scissors into small pieces approximately a few centimeters in length similar to the size of the original substrate (Figure D.3A). A pair of sharp tweezers were used to peel the tape from the white support and re-combined with half the tape hanging from the end. This allowed for easy control and peeling of the tape. To create graphene a piece of tape was firmly pressed to the graphite and slowly peeled to cleave a thin layer of graphite. Since the first peel usually results in a single piece of cleaved graphite another piece of tape was used to re-cleave the graphite once more resulting in multiple pieces of thin graphite flakes. The tape was then carefully pressed onto the substrate starting with one end and firmly smoothed over the substrate to make good contact without leaving large air bubbles (Figure D.3B). The excess tape around the edges was trimmed and the sample was soaked in a hot water bath to dissolve the tape for ~ 1 min (Figure D.3C) and then the excess tape residue was slowly rinsed with a wash bottle containing high purity water. Once the bulk tape residue was rinsed away the sample was dried with streaming

nitrogen and a piece of tape was used to cleave some of the top layers of graphite from the substrate which then exposed single and multi-layer graphene flakes. An optical microscope was subsequently used to identify and locate clean sample regions.

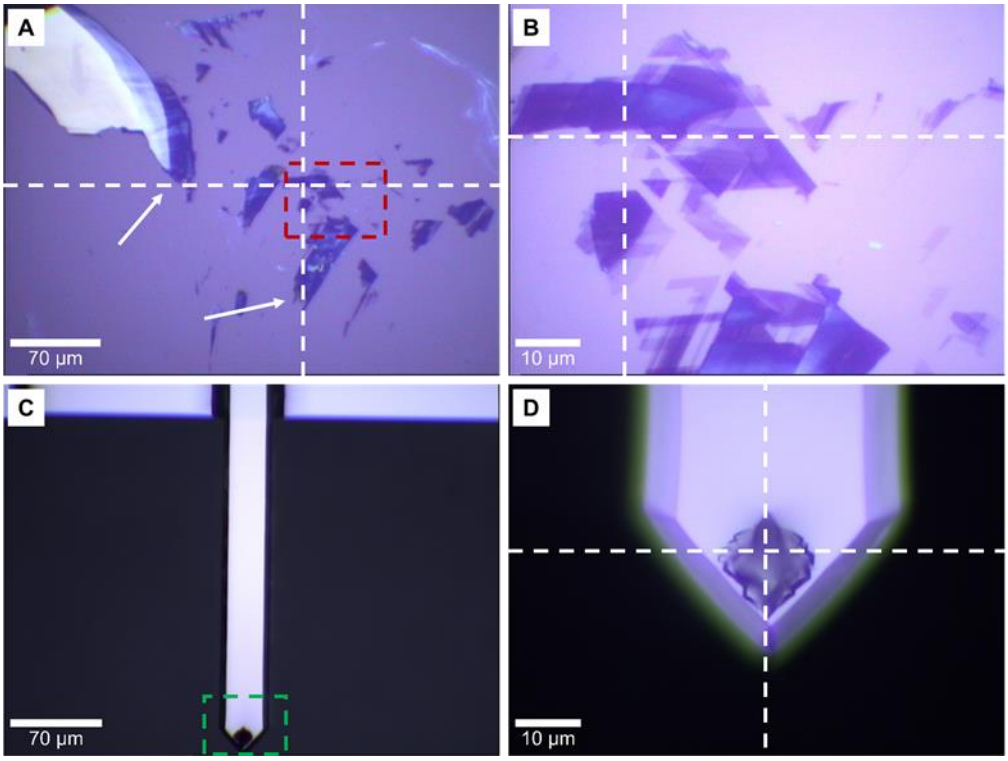

Figure D4. (A) Example 20x optical micrograph of exfoliated single and multi-layer graphene flakes on a thermally oxidized silicon wafer. (B) 100x optical micrograph corresponding to the region marked by the red box in (A). (C) 20x optical micrograph of an example contact mode silicon AFM tip. (D) 100x optical micrograph corresponding to the region marked by the green box in (C). The white dashed lines were used to align the center of the AFM tip on a single layer graphene by using surrounding graphite flakes marked with white arrows.

Confocal Raman Microspectroscopy

A confocal microscope was used to locate regions of the sample containing thin layers of graphene and to identify clean areas as well as take Raman measurements to differentiate single layer graphene from two or more layers. Figure D.4A shows an example 20x optical micrograph of single and multi-layer graphene flakes exfoliated on a thermally oxidized silicon wafer. The 100x optical micrograph in Figure D.4B corresponds to the region marked by the red box in Figure D.4A. The single layer graphene flakes were typically found to be less than 10 μm^2 but were large enough to see optically with the 100x objective lens and collect Raman spectra. For sample regions too small to clearly differentiate between the graphene layers, high resolution Raman maps were used to confirm the location of single layer graphene and the identify the number of graphene layers in the surrounding area. Raman maps were typically 10-15 μm^2 with 100 data points per line for 100 lines. The integration time for each spectra was 0.2 sec, however the laser power being ~ 1 mW was sufficient to collect Raman spectra with a good signal-to-noise ratio while using lower integration times to maintain a reasonable total data acquisition time. It is also noted that before Raman measurements the laser was allowed to warm up and fully equilibrate for at least 30 min to obtain a stable power output.

Atomic Force Microscopy

After the optical micrographs and Raman were collected the images were then used to locate the sample region on the high resolution atomic force microscope and also aided in aligning the tip directly on the graphene flakes. Figure D.4C shows a 20x

optical micrograph of a typical silicon contact mode AFM tip and Figure D.4D shows a 100x optical micrograph of the same tip corresponding to the region marked by the green box in Figure D.4C. From these images the general location of the AFM tip on the cantilever can be observed and used to aid in aligning the tip on the graphene flakes. To align the tip in the high resolution microscope the exact location must be known since the image scan size is limited to 10 μm^2 and repeated imaging to blindly search for the sample would severely damage the AFM tip. The sample region was first located by placing the known quadrant containing the graphene in the center of the sample plate on double sided scotch tape to hold the sample in place. The large graphite flakes observed in the 20x optical micrograph were then located using the camera on the high resolution AFM. The tip was then mounted and the laser beam focused on the back of the cantilever to the photodetector which was also aligned so the laser was in the center of the detector. Using the camera on the microscope the sample stage was moved in the x and y direction to align the tip over the graphene. Since the cantilever is much wider than the actual tip and the graphene under the cantilever is hidden, the tip was aligned to surrounding graphite flake markers that were further from the sample region but in line with the graphene as shown by the dotted white lines in Figure D.4A and Figure D.4B and marked by the white arrows in Figure D.4A. Since exfoliation with water soluble tape typically leaves many large graphite flakes on the substrate this alignment method can be utilized on most samples. After aligning the tip over the graphene flake a 10 μm^2 region was scanned and the 100x optical micrograph was used to precisely determine which flakes were being scanned using the friction images. These images provide high

contrast between the silica and graphene and the unique shape of the exfoliated flakes can be matched in the optical micrographs or Raman maps to confirm the location of the tip on the graphene layers. This alignment method was used for all graphene samples and typically allows for placement of the tip within a 20 μm^2 of the actual sample (after a little practice) so the graphene can be found after a few scans with the tip quality preserved.

After the graphene flakes of interest were located they were first imaged in low load contact mode to determine if the graphene and surrounding silica substrate was clean and contained minimal residue from the exfoliation process. To minimize tip wear during imaging, the load was maintained at 5 nN with slow scan speeds. High quality images were obtained with low loads, slow scan speeds, and resolutions of 512 data points with 512 lines for image sizes smaller than 5 μm^2. The I gain and P gain were optimized during imaging and the z range adjusted depending on the amount of drift observed. After the graphene flake was located the tip-sample setup was allowed to settle for 30 min to an hour to reduce the drift for obtaining stable and consistent measurements and the laser beam alignment on the cantilever and detector were adjusted a final time once stable values were obtained. During imaging the light from the camera was turned off to reduce noise from the cooling fan. Friction measurements were taken from the lateral signal trace and retrace images obtained on small regions of each graphene flake and the silica substrate.

Adhesion measurements were taken after collecting a topography image of the sample region of interest and then placing the tip at known locations and collecting

force-distance curves. The parameters for the data acquisition were first optimized by setting the total distance range to 300 nm (or larger) and adjusting the distance range so that the FD curve was centered. Other parameters were pre-set for consistency including the number of data points (typically 500) and the total time (typically 1 sec) which also influences the rate for each curve collected. Average curves were collected for specific locations as well as multiple locations across each sample for comparison. Once the general force-distance parameters are set (the range was adjusted to center the curves for each new set-up) force-volume images were collected by choosing the number of FD curves to obtain depending on the scan size of topography image being mapped. For example, for rough substrates fabricated by spincoating large nanoparticles (50 nm & 85 nm diameters) scan sizes of 500 nm^2 or less with a 32x32 force-distance grid array was found to be adequate for resolving the topography features with a correlated adhesion map.

For quantitative measurements the spring constant and radius of the AFM tip were calibrated using the sader method and blind tip reconstruction. To calculate the spring constant using the sader method an AFM tip was mounted and an amplitude versus frequency spectrum was collected with the AFM operating in AC mode. From this spectrum the resonance frequency can be obtained as well as estimation of the quality factor. The dimensions of the cantilever were typically used as provided by the manufacturer but can also be measured with an optical microscope from images similar to the ones in Figure D.4C and Figure D.4D. To calibrate the tip radius high resolution

images were obtained on substrates with a known geometry such as strontium titanate or NioProbe standard samples.

Infrared Spectroscopy

Infrared spectroscopy was used to characterize the silane functionalized substrates. An ATR accessory was used for thin film measurements and a MCT detector cooled with liquid nitrogen. Before collecting background and sample spectra parameters were set which typically included aligning the laser beam, making sure the raw interferogram was saved, the output set to absorption, the total number of scans, the wavenumber range, optical velocity, resolution and the aperture size. If the detector or accessory was recently changed the IR was allowed to equilibrate with high flowing dry nitrogen to remove excess humidity from inside the chamber.